Studies at the Solution/Air Interface by Experiment and Molecular Dynamics Simulation

Esther R Rousay

Supervisors: Dr J. G. Frey, Dr J. W. Essex

Advisor: Dr A. E. Russell

A thesis submitted for the qualification of

Doctor of Philosophy at the University of Southampton

School of Chemistry

September 2005

University of Southampton

ABSTRACT

FACULTY OF SCIENCE

SCHOOL OF CHEMISTRY

Doctor of Philosophy

Studies at the Solution/Air Interface using Second Harmonic Generation and Molecular Dynamics Simulations

by Esther Ruth Rousay

The behaviour of benzo-15-crown-5 and 4-nitrobenzo-15-crown-5 at the aqueous solution/air interface has been studied, as a function of bulk concentration, using surface tension measurements, second harmonic generation (SHG) spectroscopy and molecular dynamics (MD) computer simulations.

From the surface tension measurements, the area occupied per molecule at the surface is derived over a bulk concentration range between 0 and 10 mM. This is used to set up a series of MD simulations, which enable investigation of the crown ethers on an atomistic scale. These simulations allow the calculation of parameters that influence the second harmonic response of the system, such as the tilt angle of the molecule to the surface normal and the order parameters $\langle P_1 \rangle$, $\langle P_2 \rangle$ and $\langle P_3 \rangle$. An estimate of the interfacial refractive index, n_{int} of the system may also be obtained. The conformations which may be adopted by the crown ethers at the surface are also examined.

SHG analysis also relies upon several assumptions about the system under investigation, and through the simulations, it is possible to examine the validity of these assumptions.

The combination of these three techniques greatly increases the understanding of the systems investigated, and also allows a critical analysis of the limitations and assumptions used.

Acknowledgements

I would like to say thank you to everyone who helped in any way at all to make this thesis happen! Thank you Jeremy for your supervision, guidance, and enthusiasm, and for finding funding to allow me to continue to work on the project! Thanks Jon, for supervision of my computational work, and for helping keep the end in sight!

Thank you Lefteris: for the motivational talks, the advice and the viva preparation, as well as your help with the practical work and the theory behind SHG. Thanks for being genuinely interested in my work, and being approachable!

To Harry and Alison, my parents, a massive thank you for all your encouragement, support, and listening to everything I babbled on about regarding the phD. Generally, thanks for being fabulous!

Thanks to everyone in both groups for making the journey bearable (even enjoyable at times...): to Jamie and Tleyane for frequent help with the laser setup, to Hanne, Helen and Sarah for lunchtime escapism, to Donna for always having a sympathetic ear!

Finally, my biggest acknowledgement has to be to Adrian, for being there to mentor, tutor and do anything you could to help (and that was a lot!) with my computational work, for proof-reading and listening, and also for being eternally patient, loving and positive about my phD. Don't know how I'd have done it without you!

Contents

Chapter 1

Introduction

1.1 Interfaces

Interfaces are of great importance in many aspects of science. In terms of the living world, interfaces are all around. There is the massive interfacial region between sea and air, between land and sea, land and air, and foliage and air. Microscopically, interfaces are numerous within living organisms.

An interface is the boundary region between two bulk phases, and both its chemical and physical properties differ from each of these phases. The interface has a thickness of perhaps a few molecular diameters, but is of great importance in terms of the chemistry that can occur there.

An interfacial layer has chemistry analogous to that of bulk in some instances; for example, substances may dissolve at an interface until saturation is reached - in many cases with a species which will not dissolve in either bulk phase[1–3]which often results in the formation of a monolayer of substance. Chemical reactions may occur at interfaces at accelerated rates in many cases due to concentration and forced orientation of the molecules involved.

The reason for the altered behaviour of a system at an interface is due to the asymmetric forces acting upon atoms and molecules in the region. This is particularly well illustrated in the geometric arrangement, equilibrium constants, pH,

molecular motion and phase and phase changes of amphiphilic molecules located in the layer.[4]

1.2 Techniques for the Study of Liquid Interfaces

1.2.1 Surface Tension Measurement

The simplest property of a liquid-air interface which may be measured is the surface tension, γ. Molecules in a liquid have cohesive forces between them and in the bulk liquid this force is symmetric in all directions. At the liquid-air interface the molecules experience an imbalance of forces. The molecules spontaneously contract in order to minimise the surface area, and thus maximise the number of molecules in bulk. This leads to the presence of free energy at the surface (the surface free energy). The surface tension, expressed in N m^{-1}, is exactly equivalent to the surface free energy, which has units of J m^{-2}.

Surface active molecules, or surfactants, have both hydrophobic and hydrophilic parts, and so these molecules aggregate at the surface, decreasing the surface free energy (i.e lowering the surface tension). Surface tension alone, however, is insufficient to obtain in-depth information about the interface.

Depending upon the particular system being studied, several techniques may be applied to studies at the water-air interface.

1.2.2 Non-Linear Optical Techniques

The interface is, in terms of volume and area, a very small part of a chemical system. If the molecules being studied are present solely in this region, then ordinary spectroscopic methods form a good basis on which to begin an investigation (e.g absorption/fluorescence spectroscopy).

In a solution/vapour interface, where the compound of interest is soluble, or partially soluble in the liquid, there will be an equilibrium between bulk and inter-

facial presence. In such cases, the techniques mentioned above become redundant for interfacial study, as any signal from the interface will be lost within the much larger bulk signal. Surface specific techniques are required to probe such systems.

Non-linear optical spectroscopy is one such technique,[5,6] whereby an intense electromagnetic beam is focussed onto an interface, evoking a quadratic (or higher) response from the media, which may be detected. Those techniques utilising the quadratic, or second harmonic (SH), response include second harmonic generation (SHG), second harmonic ellipsometry (SHE)[7] and sum frequency generation (SFG). The basis of all of these techniques is described in more detail in Chapter 2.2.

1.2.3 Other Experimental Techniques Applied to the Study of Liquid Interfaces

There are several other techniques which may be applied to the study of liquid-air interfaces. Many of these are linear optical methods, including ellipsometry and Brewster angle microscopy.

In ellipsometry, a polarised incidence beam is reflected off a surface. The change in the phase and amplitude of the reflected beam is recorded. From the change in these parameters, information about film thickness may be obtained,[8] and adsorption studies may also be carried out.[9] If a variable wavelength incidence source is applied, then dielectric properties may also be determined.

Brewster angle microscopy also uses a polarised incident light source, and the reflected light at the Brewster angle depends upon the thickness, roughness and anisotropy of a layer at the interface. It can be used to probe orientational changes in a surface active system.[10]

X-ray reflectivity is also often applied to liquid surfaces,[11,12] and the change in the reflectivity of a surface is measured. This technique gives information on the thickness or surface roughness and the density of thin films at an interface.

1.2.4 Computational Methods

Computational chemistry is an evolving field, and is becoming increasingly important due to the availability of greater computational power. There are many aspects of computational chemistry which model systems in different ways, from the quantum mechanical (QM) methods, which are, by their rigorous nature, limited to relatively small systems, through to the more approximate molecular mechanics (MM) methods which may not be able to model properties dependent purely on electronic distribution, but can accurately model other properties of very large protein systems.

In some cases, a small portion of a system under study will be treated by QM methods, and the rest of the system, whose effect is still of importance, but which is not the region of direct interest, will be treated using MM models. Such simulations are described as QM-MM.

In this work, molecular dynamics (MD) is used to simulate the systems. This is an MM method, and allows the behaviour of larger systems to be monitored with time.

1.3 Crown Ethers

Crown ethers are an important family of chemicals with the ability to bind ions in a very selective manner. Ions may be sequestered in the centre of the polyether cavity. This property lends them to applications within extraction chromatography, and the removal of ions from waste solutions. Another important property of crown ethers is the capacity for the solubilisation of inorganic salts or alkali metals in organic solvents. This means the family has applications in non-aqueous experimental chemistry, organic and inorganic syntheses, among many others.

Much research has been done, and is being done, with regards to possible ap-

plications of various crown ethers and crown ether derivatives, and there are clearly many fields in which these compounds are of great use.

Many studies have been performed on the thermodynamic properties of crown ethers, binding constants, and types of complex formed. In this project the emphasis lies on describing the orientation and behaviour of the uncomplexed crown ether at the aqueous solution/air interface using a combination of experimental and computational techniques. The effect of sodium complexation is briefly studied for the nitrocrown, but this is in order to determine the effect of glass storage on the compound, rather than to extend the study into complexed crown ethers.

The molecules investigated in this project, benzo-15-crown-5 and 4-nitrobenzo-15-crown-5, shown in Figure 1.1, are simple crown ethers which contain nonlinear-optically active chromophores, and so allow a detailed surface behavioural study by both experimental and computational methods. If a thorough characterisation of these uncomplexed molecules at the water-air interface may be performed with this combination of methods, then it lays the foundations for further work on more highly functionalised crown ethers, and also on complexed crown ethers, for which there are many very important applications.

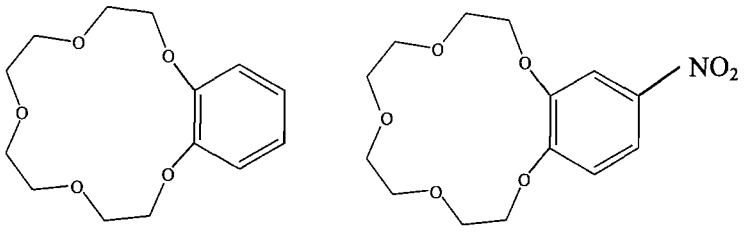

Figure 1.1: The molecules studied in this work, benzo-15-crown-5 (left) and 4-nitrobenzo-15-crown-5 (right).

1.4 Aims of Project

The aims of the project are:

- To fully characterise the behaviour of the uncomplexed crown ethers, benzo-15-crown-5 and 4-nitrobenzo-15-crown-5 at the solution-air interface, in terms of orientational properties, conformational properties, and position at the interface, through the use of surface tension and second harmonic generation experiments, and through molecular dynamics simulations.

- To investigate the assumptions underlying the optical experimental interpretation using the MD results, and to evaluate these assumptions, and their limitations, with reference to the studies carried out.

- To provide some general guidelines on the role of MD simulations in interpreting SHG data.

1.5 Structure of Thesis

This thesis is presented in three parts. Firstly, the experimental theory is reported, for both surface tension and second harmonic generation, followed by the experimental results for each crown ether. These results are discussed for each system.

The second part includes the computational theory, followed by the simulation results on each crown ether. The results obtained are analysed and discussed.

The final part of the thesis draws together the results from both experiment and simulation, and explains how the use of the three techniques in combination has enabled a thorough study of the interface in each system, and also evaluates the use of MD simulations as a means of improving the reliability of SHG results.

Part I

Experimental Work

Chapter 2

Experimental Theory and Methods

In this chapter, the theory behind both surface tension measurement and second harmonic generation (SHG) experiments is introduced, and the experimental methods are described.

2.1 Description of Surface Tension

Surface tension is the tangential force acting at the interface of fluids arising from imbalanced cohesive forces there. Surface, or interfacial, tension may be derived from either a mechanical or a thermodynamic approach. Both of these approaches will be introduced here, as both are used within the work - the thermodynamic approach leads to the analysis used for experimental work, and the mechanical approach is the basis for surface tension calculation within the simulations.

2.1.1 Mechanical Description

From a mechanical point of view, the surface tension is a force per unit length parallel to the interface. The system containing a liquid and a vapour phase may be represented as in Figure 2.1. In such a system, consider the way in which the mass density, $\rho(z)$, and the stress tensor, $\sigma_{ij}(z)$, defined below, change as the liquid surface is approached, where z is the surface normal. Within each bulk phase, $\rho(z)$ will be a constant, ρ_L, within the liquid, and a different, much lower value, ρ_V, in

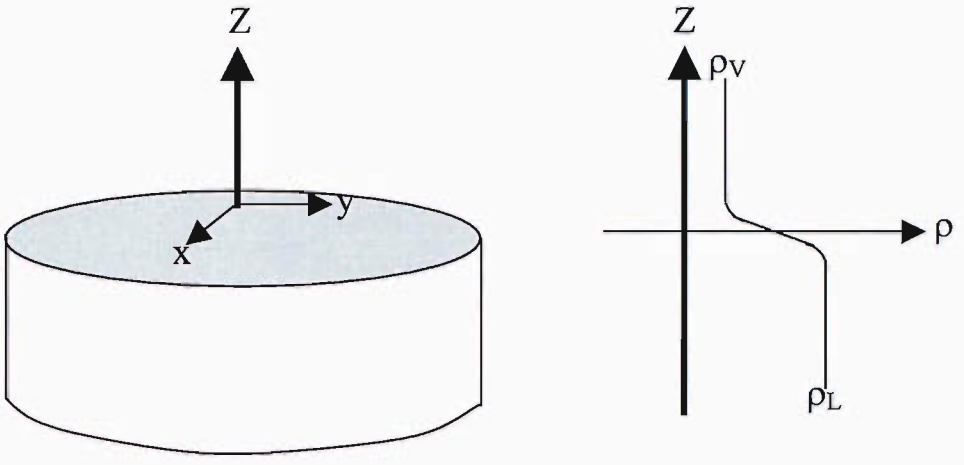

Figure 2.1: The laboratory axes, defined in terms of the surface layer which is shown in light grey. The density profile of the system is also shown, showing the gradual drop from ρ_L, the liquid density, to ρ_V, the vapour density.

the vapour. $\rho(z)$ does not change discontinuously from ρ_L to ρ_V, but varies over a distance of about two molecular lengths (about 1 nm), as illustrated in Figure 2.1.

The stress tensor, $\sigma_{ij}(z)$, is defined as the force per unit area in direction j acting across an imaginary interface in the fluid perpendicular to direction i, on the fluid with the smaller value of i-coordinate.[13] For any material, using classical mechanics, Newton's second law may be applied to a volume element at point r:

$$F_i(\mathbf{r})\rho(\mathbf{r}) + \sum_{j=1}^{3} \frac{\partial \sigma_{ji}(\mathbf{r})}{\partial x_j} = \rho(\mathbf{r}) \frac{du_i(\mathbf{r})}{dt} \tag{2.1}$$

where $F_i(\mathbf{r})$ is the body force per unit mass, describing effects such as gravitation, the second term on the left hand side of the equation involves the contact forces, σ_{ij}, between neighbouring elements of fluid, and u_i is the fluid velocity at point $(\mathbf{r})$. Gravitational effects are negigible at the interfacial region (the surface is of very small mass), and for the purposes of this work, we are concerned with a static fluid interface. Thus, $F_i(\mathbf{r})$ vanish, and u_i are zero, reducing Equation 2.1 to Equation 2.2.

$$\sum_{j=1}^{3} \frac{\partial \sigma_{ji}(\mathbf{r})}{\partial x_j} = 0 \tag{2.2}$$

Equation 2.2 gives rise to a set of three equations of hydrostatic equilibrium.

Within the bulk liquid and vapour phases, the stress tensor is:

$$\sigma_{ij}^{(bulk)} = \begin{pmatrix} -P_o & 0 & 0 \\ 0 & -P_o & 0 \\ 0 & 0 & -P_o \end{pmatrix} \tag{2.3}$$

Where P_o is atmospheric pressure. Equation 2.3 satisfies the equilibrium condition specified in Equation 2.2, but there is a more general tensor which satisfies the condition. This is derived by considering how the stress tensor is restricted by Equation 2.2. By symmetry, σ_{ij} can depend only upon z, and so Equation 2.2 may be written:

$$\frac{\partial \sigma_{zx}(z)}{\partial z} = 0, \quad \frac{\partial \sigma_{zy}(z)}{\partial z} = 0, \quad \frac{\partial \sigma_{zz}(z)}{\partial z} = 0 \tag{2.4}$$

The shear stresses σ_{xz} and σ_{yz} are seen, by a simple symmetry argument, to be always zero, and the normal pressure, $P_N(z) \equiv -\sigma_{zz}$, is constant throughout the interfacial region, and is equal to P_o. Therefore, only the tangential pressure, $P_T(z) \equiv -\sigma_{xx}(z) \equiv -\sigma_{yy}(z)$ may vary with z whilst the system remains at equilibrium. The most general tensor satisfying the condition is:

$$\sigma_{ij} = \begin{pmatrix} -P_T(z) & 0 & 0 \\ 0 & -P_T(z) & 0 \\ 0 & 0 & -P_N = -P_o \end{pmatrix} \tag{2.5}$$

In the bulk regions, all three diagonal components are equal, i.e $P_T = P_N$. In the surface region, however, the tangential pressure can decrease enormously, changing into a tension, as shown in Figure 2.2.

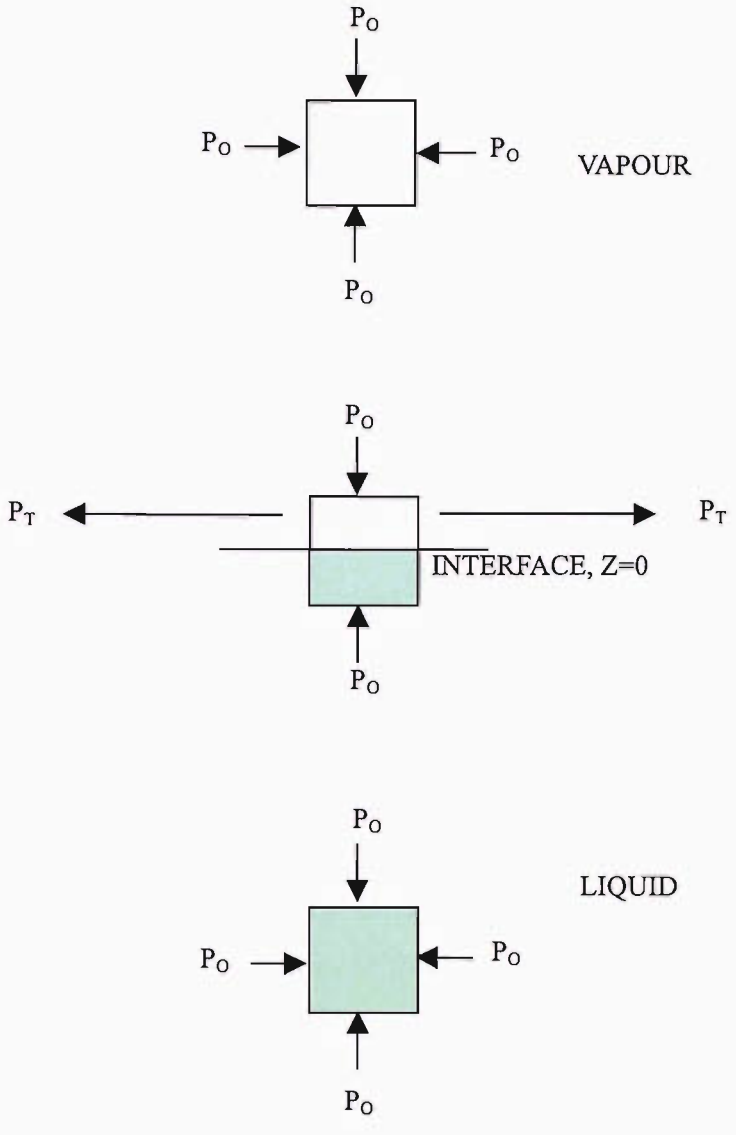

Figure 2.2: The pressures acting upon elements of bulk fluid, bulk gas, and across the interfacial region

If we assume the interface to be a plane of discontinuity, at $z = 0$, between liquid and vapour (and this is not unreasonable given the very small thickness of the interfacial region), then perpendicular to any line of unit length in the z=0 plane, there acts a force γ with which the liquid surface on one side pulls the liquid surface on the other, and this is the surface tension.

To obtain γ, the value of $P_N - P_T(z)$ is integrated over the surface:

$$\gamma = \int_{-\infty}^{\infty} [P_N - P_T(z)]\, dz \tag{2.6}$$

2.1.2 Thermodynamic Description

From a thermodynamic perspective, the surface tension is an additional free energy per unit area, arising from the presence of the interface. If the walls of the closed system were to be moved a small amount such that the area, A, of the liquid surface was increased by dA, under constant temperature and pressure conditions, then the work done on the system, dW, will be:

$$dW = \gamma dA \tag{2.7}$$

The enthalpy of the system will then change by dH:

$$dH = TdS + dW \tag{2.8}$$

where dS is the entropy change in the system. However, dS is not known at this stage. It is not zero, as the system was expanded isothermally, and not adiabatically. Looking at the expansion in terms of the Gibbs free energy of the system, G, defined as $G = H - TS$, the change is:

$$dG = dH - TdS - SdT = dW - SdT \tag{2.9}$$

And since this was an isothermal expansion, Equation 2.9 becomes $dG = \gamma dA$. In full:

$$\gamma = \left(\frac{\partial G(T,P,A)}{\partial A}\right)_{T,P} \tag{2.10}$$

This is a thermodynamic interpretation of gamma. Both Equation 2.10 and Equation 2.6 are valid ways to express surface tension. They are numerically equal,

and their units are equivalent: for the mechanical interpretation of γ as a force, the units usually used are N m^{-1}, and for the thermodynamic interpretation where γ is considered as a free energy change, they are J m^{-2}.

Whether considered from a mechanical or a thermodynamic basis, the main effect is that a system will act to reduce its interfacial area as much as possible.

2.1.3 Isotherms and Equations of State

Gibbs Surface Excess Quantities

Although the interfacial region has finite thickness, it is convenient to represent it as a mathematical surface of zero thickness. This is because such properties as area and curvature are well defined and the differential geometry of surfaces is understood.

Gibbs[14] introduced the idea of surface excess quantities as a reconciliation of the use of mathematical surfaces to represent a three-dimensional interface.

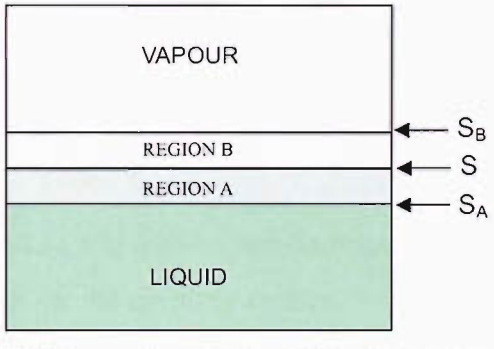

Figure 2.3: Illustration of the Gibbs definition of the interface

Consider a system consisting of two phases, A and B, which are in contact with one another, and which contain a species c. The interface as defined by Gibbs is a plane, S, between the two phases. This plane is chosen such that it is always perpendicular to the local density or concentration gradient in the system, and has a surface area $a_{surface}$. If we were to assume that the bulk phases A and B extended unchanged right up to the interfacial plane, S,then:

$$U_{TOTAL} = U_A + U_B \tag{2.11}$$

However, since the interface is in fact three-dimensional, and the transition between the bulk fluids is not sudden, the actual internal energy of the interfacial region differs from Equation 2.11 by the 'surface excess' internal energy, U_S. This excess is assigned to S.

$$U_S = U_{TOTAL} - (U_A + U_B) \tag{2.12}$$

Surface excess values of other quantities are defined similarly. For example, the amount of species c which is present in the system, n_c, is expressed as in Equation 2.13, and the Gibbs free energy, G, as in Equation 2.14.

$$n_{cS} = n_c - (n_{cA} + n_{cB}) \tag{2.13}$$

$$G_S = G - (G_A + G_B) \tag{2.14}$$

In Equation 2.13, n_{cA} represents the number of moles of species c which would be *expected* in the region between S_A and S if it was *occupied uniformly* by bulk fluid A, and n_{cB} represents the number of moles of c which would be *expected* in the region between S and S_B if that was *occupied uniformly* with bulk fluid B. Similarly for the Gibbs free energy, G_A and G_B represent the free energies of the regions between S_A and S and S and S_B respectively, assuming homogeniety of each phase right up the the dividing surface, S. The surface excess quantities may be positive or negative, indicative of either a deficiency or a surplus of species in the interfacial region in comparison to the bulk phases.

From Equation 2.13, the surface excess of species c, Γ_c, is defined (Equation 2.15). This represents how far in excess (or deficiency) the amount of species c at the interface is in comparison to its expected value in the case of two ideal phases.

$$\Gamma_c = \frac{n_{cS}}{a_{surface}} \tag{2.15}$$

If $\Gamma_c > 0$, then there is more of species c present at the interface than there is in the bulk. This indicates that the species is surface active.

The Gibbs adsorption equation expresses the surface excess as a function of concentration and surface tension:

$$\Gamma_c = -\frac{c_c}{RT}\left(\frac{\partial\gamma}{\partial c_c}\right)_T \tag{2.16}$$

Equation 2.16 uses the approximation that the surface excess is about equal to the surface concentration, which is reasonable for dilute solutions and molecules of high surface activity.[15]

From the Gibbs equation, with the introduction of certain conditions or assumptions about systems, there are several types of isotherm. Using Equation 2.16 and the correct (most appropriate) $\Gamma_c(c)$ isotherm, the corresponding surface equation of state, $\gamma(\Gamma_c)$, may be derived, and subsequently $\gamma(c)$. The most basic isotherm is the Henry isotherm:

$$\Gamma_c = K_H c \tag{2.17}$$

Where K_H is the Henry's equilibrium constant. This is a suitable model for systems with very low surface concentrations compared to the maximum surface concentration attainable for that system. Using Equation 2.16, the corresponding surface equation of state is:

$$\Pi = \gamma_o - \gamma = nRTK_H c = nRT\Gamma_c \tag{2.18}$$

where γ_o is the surface tension of the pure solvent, γ is the surface tension of the solution, and Π, the difference between the values of γ_o and γ, is called the surface pressure. For non-ionic systems such as those studied here, n = 1.[15] The Henry isotherm is valid for surface concentrations which are small compared to the maximum surface concentration attainable. This is therefore only valid in a

restricted concentration range.

The Langmuir isotherm is the most common non-linear isotherm used to describe behaviour:

$$\Theta = \frac{\Gamma_c}{\Gamma_{max}} = \frac{K_L c}{1 + K_L c} \tag{2.19}$$

Where Θ is the coverage of the surface by the surfactants, Γ_{max} is the theoretical maximum surface concentration, which is usually unattainable experimentally due to either solubility limit or micelle formation. The ratio of Γ_c to Γ_{max} gives the surface coverage by the species, Θ. K_L is the equilibrium adsorption constant for Equation 2.20.

$$M + ES \rightleftharpoons FS \tag{2.20}$$

Where M is the bulk species, ES are empty sites at the surface, and FS are filled sites at the surface. When $K_L c \ll 1$, Equation 2.19 may be approximated by the Henry isotherm.

The corresponding equation of state for this isotherm is the Szyszkowski equation:

$$\Pi = nRT\Gamma_{max} ln(1 + K_L c) \tag{2.21}$$

which may alternatively be written:

$$\Pi = -nRT\Gamma_{max} ln\left(1 - \frac{\Gamma_c}{\Gamma_{max}}\right) \tag{2.22}$$

Equation 2.22 gives $\Pi = f(\Gamma_c)$ instead of $\Pi = f(c)$, which is what is usually experimentally measured. It may be applied to data in conjunction with Equation 2.16. The Langmuir isotherm accounts for a lattice-type model of the surface molecules, and assumes no interaction between molecules or empty sites on the

surface (i.e solvent).

There are several isotherms which have been developed to account for non-ideal adsorption and which take into consideration the interaction between molecules on the surface. The least complex of these is the Frumkin isotherm:

$$c = \frac{1}{K_F}\frac{\Gamma_c}{\Gamma_{max} - \Gamma_c} exp(-b\left(\frac{\Gamma_c}{\Gamma_{max}}\right)) \tag{2.23}$$

K_F is the Frumkin equilibrium adsorption constant, b is an interaction parameter for the molecules at the interface. For $b = 0$ the surface is ideal, and the Frumkin isotherm reduces to the Langmuir isotherm.

The corresponding equation of state for the Frumkin isotherm is:

$$\Pi = -nRT\Gamma_{max}\left[ln\left(1 - \frac{\Gamma_c}{\Gamma_{max}}\right) + \frac{1}{2}b\left(\frac{\Gamma_c}{\Gamma_{max}}\right)^2\right] \tag{2.24}$$

This is appropriate mainly for non-ionic surfactants. Extensions of this model include the Volmer and Van der Waals isotherms.[16]

Summary

Surface tension measurements provide a good basis on which to begin further investigation. An area occupied per molecule may be obtained via the correct isotherm (that is, the relationship between the surface tension and the bulk concentration), and this can give some indication of surface coverage and the way in which the surfactants interact. Other techniques must be used to further probe the interfacial layer.

2.2 Second Harmonic Generation

Good characterisation of surfaces at the microscopic level is essential to further our understanding of the multitude of phenomena occuring at interfaces. Many early surface specific techniques involve the emission, absorption or scattering of charged particles, and so are limited to use under vacuum conditions.[17] Optical techniques do not have this limitation, but ordinary linear optical techniques are not surface specific. Even if the species under investigation is only present at the interface, the optical signal is generally sensitive to the interfacial layer being of thickness of the order of wavelength used.[18] Ellipsometry is one exception which has been applied extensively to the study of interfaces, often in conjunction with other methods.[19]

The use of non-linear optical (NLO) techniques, which has been possible since the advent of the laser, allows intrinsically surface specific probing, within the dipole approximation, of a system down to sub-monolayer levels. The most widely used NLO methods are second harmonic generation (SHG), which is used in this work, and the related sum frequency generation (SFG). The theory of SHG is described in this chapter.

2.2.1 The Macroscopic Geometry of the Interface

The experimental plane containing the surface normal and the beam before and after reflection is called the plane of incidence (Figure 2.4). Light waves with their electric field oscillating exclusively in the plane of incidence are denoted as being *p*-polarised. Waves with their electrical field oscillating perpendicular to the plane of incidence (i.e. parallel to the surface under investigation) are denoted as *s*-polarised.

The *x*, *y* and *z* axes in Figure 2.4 are the laboratory axes. The input polarisation angle, γ, is the angle made between the incident beam and the plane of incidence, and the output polarisation angle, Γ, is the angle made between the output beam and the plane of incidence. α is the angle between the incident beam and the sur-

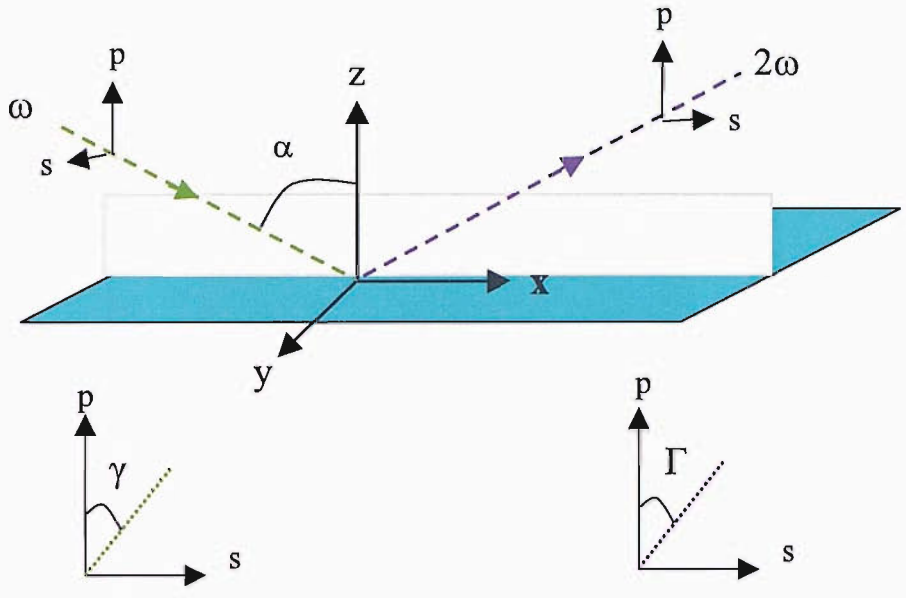

Figure 2.4: The experimental geometry used, showing laboratory axes and defining the incident plane. The direction of polarisation of the light is defined with respect to the incident plane (z-x plane). If the light is polarised parallel to the incident plane, then it is denoted p-polarised, and if it is polarised perpendicular to the incident plane (z-y plane), then it is denoted s-polarised.

face normal.

When light impinges on an interface between two media, some of it will be reflected, and some will be transmitted, in proportions which may be estimated using Fresnel's equations of reflection.[20] These equations relate the angle of incidence, the angle of refraction, the refractive indices to reflection, r, and transmission, t, coefficients.

$$r_p = \frac{n_2 \cos\alpha_i - n_1 \cos\alpha_t}{n_2 \cos\alpha_i + n_1 \cos\alpha_t} \tag{2.25}$$

$$r_s = \frac{n_1 \cos\alpha_i - n_2 \cos\alpha_t}{n_1 \cos\alpha_i + n_2 \cos\alpha_t}, \tag{2.26}$$

$$t_p = \frac{2 n_1 \cos\alpha_i}{n_2 \cos\alpha_i + n_1 \cos\alpha_t}. \tag{2.27}$$

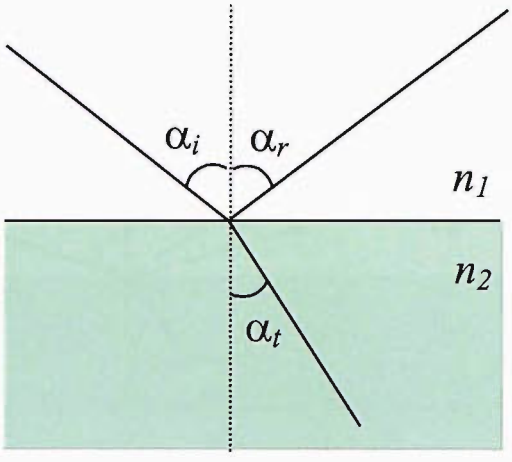

Figure 2.5: Light wave impinging on a surface between two layers of differing refractive index. A proportion of the light is reflected, and a proportion is transmitted (refracted) through the medium.

$$t_s = \frac{2n_1\cos\alpha_i}{n_1\cos\alpha_i + n_2\cos\alpha_t} \tag{2.28}$$

Once this light is of high enough intensity to allow non-linear effects, and thus, interfacial properties, to be detected, it is necessary to expand these equations to describe a more detailed interfacial geometry.

The Three-Layer Model

In order to fully describe the geometry of a system containing two bulk phases and an interfacial layer whose properties differ from each bulk phase, a three-layer model of the system was chosen.[21] Other models have been presented,[22] but the three-layer one is often used. The model is illustrated in Figure 2.6.

The properties of the interface region (medium S) are not those of either medium A or medium B, and need to be determined to enhance the accuracy of the SHG analysis.

The Fresnel coefficients of this system are given by:

$$e_x(\omega) = \cos(\alpha_i)\left[1 - \frac{n_B(\omega)\cos(\alpha_i) - n_A(\omega)\cos(\alpha_t)}{n_B(\omega)\cos(\alpha_i) + n_A(\omega)\cos(\alpha_t)}\right] \tag{2.29}$$

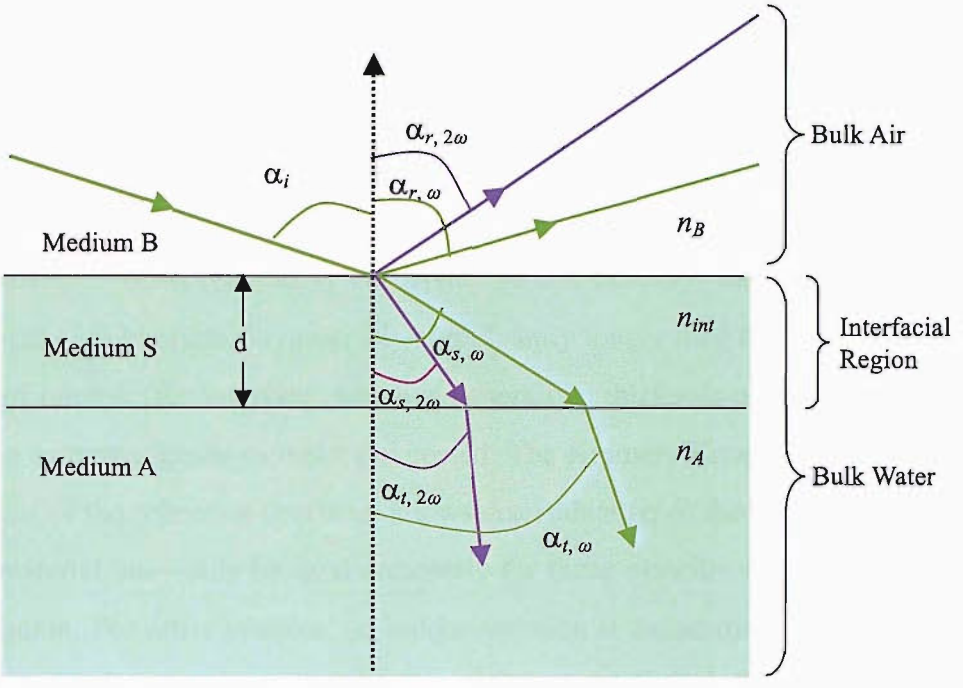

Figure 2.6: The Three-Layer description of the interface used for SHG interpretation. The angles made by the incident radiation (entering the medium from angle α_i to the surface normal), on reflection (α_r), transmission through the interfacial region (α_s) of refractive index n_{int}, and transmission through bulk medium A (α_t) of refractive index n_A. d is the thickness of the interfacial region.

$$e_x(2\omega) = -\frac{2n_A(2\omega)\cos(\alpha_i)\cos(\alpha_t)}{n_A(2\omega)\cos(\alpha_t)+n_B(2\omega)\cos(\alpha_i)} \tag{2.30}$$

$$e_y(\omega) = 1+\frac{n_A(\omega)\cos(\alpha_i)-n_B(\omega)\cos\alpha_t}{n_B(\omega)\cos\alpha_t+n_A(\omega)\cos(\alpha_i)} \tag{2.31}$$

$$e_y(2\omega) = \frac{2n_A(2\omega)\cos(\alpha_i)}{n_B(\omega)\cos(\alpha_t)+n_A(\omega)\cos(\alpha_i)} \tag{2.32}$$

$$e_z(\omega) = \frac{n_A^2(\omega)sin(\alpha_i)}{n_{int}^2(\omega)}\left[1+\frac{n_A(\omega)\cos(\alpha_t)-n_B(\omega)\cos(\alpha_i)}{n_B(\omega)\cos(\alpha_i)+n_A(\omega)\cos(\alpha_t)}\right] \tag{2.33}$$

$$e_z(2\omega) = \frac{1}{n_{int}^2(\omega)}-\frac{2n_A(2\omega)\cos(\alpha_i)\cos(\alpha_r)}{n_A(2\omega)\cos(\alpha_t)+n_B(2\omega)\cos(\alpha_i)} \tag{2.34}$$

Interfacial Refractive index

The interfacial refractive index, n_{int}, used in the analysis of the second harmonic response is difficult to determine. There are experimental methods which can be used to calculate n_{int}, such as ellipsometry and the use of the Kramers-Kronig analysis.[19,23] However, this is not trivial: in ellipsometry, the wavelength used (generally visible light) is invariably significantly longer than the width of the region of interest (the interface, which is generally a thickness of about 1 or 2 nm) and so accurate results cannot be expected. The Kramers-Kronig analysis, where analysis of the reflection spectrum allows determination of the dielectric function of a material, may only be used accurately for those systems with strong enough absorption. For other systems, no unique solution is found through this method. Even if n_{int} is calculated explicitly, several assumptions are made, and so it is more common to use direct assumptions of the value. The most common ways in which n_{int} is assigned within a system are to assume that $n_{int} = \frac{1}{2}(n_A + n_B)$, or to take n_{int} as being either n_A or n_B.

It is possible to get an estimate of interfacial refractive index from SHG measurements in certain cases. For example, if the microscopic geometry of a system is known, then it is possible to fit the value of n_{int}.[24]

In this project, as with many SHG studies, the microscopic geometry at the interface is unknown, and so for the initial experimental analyses, the interfacial layer was assumed to have a refractive index which was the average of the two bulk phases, water and air. The results of the simulations carried out are used to assist with the estimation of n_{int} at a later stage.

2.2.2 Polarisation Effects of an Electromagnetic Wave, and the Origin of SHG

If a light wave of frequency ω falls upon a dielectric medium, then it induces a polarisation within the constituents of the medium. The molecules within the medium act as anharmonic oscillators, and so overtone oscillations are excited at

frequencies 2ω, 3ω etc.[5]

At low light intensities, these overtones are negligible, and the induced polarisation in the medium, **P**, is proportional to the intensity of the incident light. For higher light intensities however, such as those emitted by pulsed lasers, the electric field generated, **E**, can induce a polarisation in the medium which may be approximated by a power series in **E**, shown in Equation 2.35.

$$\mathbf{P}(\omega, 2\omega \ldots) = \varepsilon_0 \left(\chi^{(1)}(\omega)\mathbf{E} + \chi^{(2)}(\omega, 2\omega)\mathbf{E}(\omega)\mathbf{E}(\omega) + \chi^{(3)}(\omega, 2\omega, 3\omega)\mathbf{E}(\omega)\mathbf{E}(\omega)\mathbf{E}(\omega) + \ldots \right) \tag{2.35}$$

Where ε_o is the permittivity of free space, and the coefficients $\chi^{(n)}$ are the *nth* order susceptibility tensors, which describe the material's response to the incident light. The term in the induced polarisation which gives rise to second harmonic generation (SHG) is:

$$\mathbf{P}^{(2)}(2\omega) = \varepsilon_0 \chi^{(2)} \mathbf{E}(\omega)\mathbf{E}(\omega) \tag{2.36}$$

where $\chi^{(2)}$ is the second order susceptibility tensor, a macroscopic property characteristic of the medium being impinged upon.

The electric field at the fundamental frequency, $\mathbf{E}(\omega)$ may be expressed as $\mathbf{E}(\omega) = E_0 \cos(\omega t)$. Through the trigonometric identity $\cos^2(\omega) = \frac{1}{2}(1 + \cos(2\omega t))$, equation 2.36 may instead be expressed:

$$\mathbf{P}^{(2)}(2\omega) = \frac{\varepsilon_o \chi^{(2)}}{2} E_0^2 (1 + \cos(2\omega t)) \tag{2.37}$$

Equation 2.37 illustrates that second harmonic generation arises from the second order term.

2.2.3 Surface Specificity of SHG

From Equation 2.36, it may be seen that in an isotropic medium, $\chi^{(2)}$ must be zero, since if the direction of the electric field is reversed, by the symmetry of the system, the direction of polarisation must also reverse, whilst the magnitude remains the same. Mathematically, this implies that:

$$-\mathbf{P}^{(2)} = \varepsilon_0 \chi^{(2)} (-\mathbf{E}(\omega))^2 = \varepsilon_0 \chi^{(2)} (\mathbf{E}(\omega))^2 = +\mathbf{P}^{(2)} \tag{2.38}$$

The only acceptable solution to equation 2.36 is that $\chi^{(2)}$=0 in such media. Thus, SHG is symmetry forbidden in isotropic media.

This is the basis of the surface specificity of SHG. At an interface between two media inversion symmetry is necessarily absent, and so SHG will arise. Thus, when both media are isotropic, second harmonic generation occurs only at the interface. This applies in the electric dipole limit.[5] There are other higher order processes which generate SHG and which are not forbidden in the bulk phases, such as magnetic-dipole and electric-quadrupole effects.[25,26] These are usually much weaker than the SHG arising from the interface, but for polar solvents such as water, the signal arising from these other processes may be significant. With surface active solutes which give a strong signal, though, the contribution from the water should once again be negligible.

2.2.4 The Elements of $\chi^{(2)}$, $\mathbf{P}^{(2)}$ and E

The second-order susceptibility of the interface, $\chi^{(2)}$ is a third rank tensor, and therefore has 27 components. This may be reduced, when the two-dimensional geometry of the surface is considered, to just 4 non-zero components, as long as the surface is isotropic in the surface, or x-y, plane. That is, as long as the intensity of the second harmonic response, $I_{2\omega}$, is invariant with rotation of the interface.[27]

With this assumption, which is reasonable for a liquid interface, and defining

the laboratory axes as in Figure 2.4, the non-zero components of $\chi^{(2)}$ are: χ_{zzz}, χ_{zxx}, χ_{xxz} and χ_{xyz}.

This allows the second-order polarisation, $\mathbf{P}^{(2)}$, components to be represented as:

$$\begin{pmatrix} P_x \\ P_y \\ P_z \end{pmatrix} = \begin{bmatrix} 0 & 0 & 0 & \chi_{xyz} & \chi_{xyz} & 0 \\ 0 & 0 & 0 & \chi_{xxz} & -\chi_{xyz} & 0 \\ \chi_{zxx} & \chi_{zxx} & \chi_{zzz} & 0 & 0 & 0 \end{bmatrix} \begin{pmatrix} E_x^2 \\ E_y^2 \\ E_z^2 \\ 2E_yE_z \\ 2E_xE_z \\ 2E_xE_y \end{pmatrix} \tag{2.39}$$

In fact, this is simplified further in cases of non-chiral molecules, such as those studied in this work, as the χ_{xyz} component is then also 0.

When the input polarisation angle is defined as in Figure 2.4, the components of the electric field vector, **E** incident upon the interface are:

$$\begin{pmatrix} E_x \\ E_y \\ E_z \end{pmatrix} = \begin{bmatrix} e_x \cos\gamma \\ e_y sin\gamma \\ e_z \cos\gamma \end{bmatrix} E_o \tag{2.40}$$

2.2.5 Intensities of Components

The intensity of the second harmonic signal $I_{2\omega}$, generated from a planar interface has been modelled with respect to the intensity of the incident beam, I_{ω}, and the induced second order polarisation, $\mathbf{P}^{(2)}$, at the interface. The intensity which has been derived, with geometry as in Figure 2.4 is:[27]

$$I_{2\omega} = \frac{32\pi^3\omega^2 sec^2\alpha}{c^3} |\mathbf{e}(2\omega)\chi^{(2)}\mathbf{e}(\omega)\mathbf{e}(\omega)|^2 I_{\omega}^2 \tag{2.41}$$

The **e** values represent products of the incident polarisation vectors and the

corresponding Fresnel coefficients for ω and 2ω.

The tensorial nature of $\chi^{(2)}$ indicates that the intensity of the output depends strongly upon the polarisation of the *input* beam, as well as upon the geometry of the experiment.

Theoretical Signal Intensities

The intensity of the second harmonic signal generated in the *s* and *p* planes can be predicted in terms of the non-zero elements of $\chi^{(2)}$ from Equations 2.39, 2.40 and 2.41:

$$I_s \propto |a_1\chi_{xxz}sin2\gamma + a_6\chi_{xyz}\cos^2\gamma|^2 = |E_s|^2 \tag{2.42}$$

$$I_p \propto |(a_2\chi_{xxz} + a_3\chi_{zxx} + a_4\chi_{zzz})\cos^2\gamma + a_5\chi_{zxx}sin^2\gamma - a_7\chi_{xyz}sin2\gamma|^2 = |E_p|^2 \tag{2.43}$$

where the a_i coefficients are combinations of the Fresnel factors given in Equations 2.29 to 2.34:

$$a_1 = e_y(\omega)e_z(\omega)e_y(2\omega) \tag{2.44}$$

$$a_2 = 2e_x(\omega)e_z(\omega)e_x(2\omega) \tag{2.45}$$

$$a_3 = |e_x(\omega)|^2 e_z(2\omega) \tag{2.46}$$

$$a_4 = |e_z(\omega)|^2 e_z(2\omega) \tag{2.47}$$

$$a_5 = |e_y(\omega)|^2 e_z(2\omega) \tag{2.48}$$

In fact, for non-chiral molecules such as those studied in this project, χ_{xyz} becomes 0, and so the equations simplify to:

$$I_s \propto |Csin2\gamma|^2 = |E_s|^2 \tag{2.49}$$

$$I_p \propto |Acos^2\gamma + Bsin^2\gamma|^2 = |E_p|^2 \tag{2.50}$$

Where:

$$A = (a_2\chi_{xxz} + a_3\chi_{zxx} + a_4\chi_{zzz}) \tag{2.51}$$

$$B = a_5\chi_{zxx} \tag{2.52}$$

$$C = a_1\chi_{xxz} \tag{2.53}$$

Note that the coefficients a_6 and a_7 are no longer involved in these equations. The intensity in other planes may be expressed as a combination of these equations, for example, the intensity in the planes $\pm 45^{\circ}$ to the incident plane is shown in Equation 2.54.

$$I_{\pm 45} = |E_{\pm 45}|^2 = |(\cos 45)E_p \pm (\cos 45)E_s|^2 = \frac{1}{2}|E_p + E_s|^2 \tag{2.54}$$

To deduce the relative values of the components of $\chi^{(2)}$ experimentally, polarisation dependence experiments may be carried out: that is, the second harmonic (SH) signal at fixed output polarisations is measured over a range of input polarisations. Using Equations 2.50 to 2.54, the curves produced at a number of fixed output polarisations (usually three) may be simultaneously fitted to derive the relative values of the χ components.

2.2.6 Relating SHG to Molecular Properties

The surface susceptibility is a macroscopic parameter: it is a property of the surface as a whole, describing the particular interaction of the medium with the incident electric field which results in the generation of radiation at twice the fundamental

frequency. The microscopic parameter which generates the response to the incident field is the molecular hyperpolarisability, $\beta^{(2)}$. This is also a tensorial property, and is reduced by the symmetry of the molecules.

The relationship between the susceptibility and the hyperpolarisability depends upon the relative positions of the laboratory and the molecular axis. To convert between the laboratory axes (x, y, z) and the molecular axes (O_x,O_y,O_z), represented in Figure 2.7, the Euler angles ϕ, θ and ψ are used.

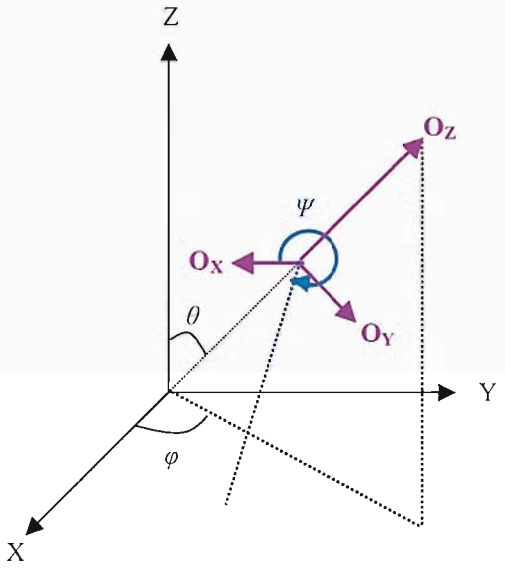

Figure 2.7: Relationship between the molecular and laboratory axis sets.

The rotation matrices required to transform the molecular axes onto the laboratory axes are R_ϕ, the rotation around the surface normal (that is, about the z-axis in the laboratory frame), R_θ, the rotation between the surface normal and the z-axis of the molecular frame (defined as the long axis of the molecule, and denoted O_Z), and R_ψ, the rotation around the molecular axis. To carry out the complete transformation from laboratory to molecular frame, the product of these matrices, $R_\psi R_\theta R_\phi$, must be carried out. Since the SHG response gives us direct information on the laboratory frame, the reverse transformation, T, needs to be applied to provide information on the molecular frame, where:

$$T = R_{\phi}^{-1} R_{\theta}^{-1} R_{\Psi}^{-1} \tag{2.55}$$

The matrix, T, resulting from the transformations is derived and given in Appendix A. This transformation links the second order susceptibility tensor to the molecular hyperpolarisability tensor, $\beta^{(2)}$, in the interface. This relationship can be expressed as:

$$\chi_{ijk} = N_s \langle T_{ii'} T_{jj'} T_{kk'} \rangle \beta_{i'j'k'} \tag{2.56}$$

N_s is the number density of molecules at the interface, and $\langle T_{ii'} T_{jj'} T_{kk'} \rangle$ is the matrix for the complete transformation from laboratory to molecular frames. If we consider a planar chromophore, such as those studied in this work, and very commonly elsewhere, then the only hyperpolarisability components of significance are those in the chromophore plane (the x-z plane). Through the transformation given in Equation 2.56 and with assumptions on the Euler angles, a system of equations for the non-zero components of $\chi^{(2)}$ is obtained. For liquid interfaces such as those studied in this work, the azimuthal angle ϕ may be assumed to be random, and this gives the system of Equations 2.57 to 2.59.

$$\chi_{xzx} = \frac{N}{2\varepsilon_o} \left[\langle sin^2\theta \cos\theta \rangle \beta_{zzz} - \langle sin^2\Psi \cos\theta sin^2\theta \rangle \left(\beta_{zxx} + 2\beta_{xzx} \right) + \langle \cos\theta \rangle \beta_{xxz} \right] \tag{2.57}$$

$$\chi_{zxx} = \frac{N}{2\varepsilon_o} \left[\langle sin^2\theta \cos\theta \rangle \beta_{zzz} - \langle sin^2\Psi \cos\theta sin^2\theta \rangle \left(\beta_{zxx} + 2\beta_{xzx} \right) + \langle \cos\theta \rangle \beta_{zxx} \right] \tag{2.58}$$

$$\chi_{zzz} = \frac{N}{\varepsilon_o} \left[\langle \cos^3\theta \rangle \beta_{zzz} - \langle sin^2\Psi \cos\theta sin^2\theta \rangle \left(\beta_{zxx} + 2\beta_{xzx} \right) \right] \tag{2.59}$$

Further assumptions must then be made regarding the angle ψ. Cases for various ψ assumptions are included in Appendix B. Additionally, the equations are

simplified according to significant $\beta^{(2)}$ components.

Through $\chi^{(2)}$ and $\beta^{(2)}$ it is possible to derive orientational information about the molecules in the system. For example, the order parameter D, given by Equation 2.60:

$$D = \frac{\frac{2}{5}\langle P_3 \rangle + \frac{3}{5}\langle P_1 \rangle}{\langle P_1 \rangle} = \frac{\langle \cos^3\theta \rangle}{\langle \cos\theta \rangle} \tag{2.60}$$

Where $\langle P_n \rangle$ represents $\langle P_n(\cos\theta) \rangle$, the Legendre polynomials of $\cos\theta$, shown in Equations 2.61 to 2.63.

$$\langle P_1(\cos\theta) \rangle = \langle \cos\theta \rangle \tag{2.61}$$

$$\langle P_2(\cos\theta) \rangle = \langle \frac{3\cos^2\theta - 1}{2} \rangle \tag{2.62}$$

$$\langle P_3(\cos\theta) \rangle = \langle \frac{5\cos^3\theta - 3\cos\theta}{2} \rangle \tag{2.63}$$

The value of D of an interface may be expressed by combining Equations 2.57 to 2.59. The expression for D in terms of $\chi^{(2)}$ components therefore depends upon which hyperpolarisability components are significant for a particular species. For example, for a common example of a system containing molecules of C_{2v} symmetry,[28] β_{zzz} and β_{zxx} are expected to be dominant,[29] and in that case, Equation 2.64 gives D. The expressions for D for various other dominant β_{lmn} are given in Appendix C.

$$D = \frac{\chi_{zzz} - \chi_{zxx} + \chi_{xxz}}{\chi_{zzz} - \chi_{zxx} + 3\chi_{xxz}} \tag{2.64}$$

This order parameter must be interpreted with care. SHG studies often culminate in a reported "tilt angle", between the surface normal and the long axis of the

surface molecule. This relies on the approximation that:

$$D = \frac{\langle \cos^3\theta \rangle}{\langle \cos\theta \rangle} \approx \langle \cos^2\theta \rangle \approx \langle \cos\theta^2 \rangle \approx (\cos\langle\theta\rangle)^2 \tag{2.65}$$

However, this equation only holds if the distribution of θ is very narrow. If this is not the case, then the reported tilt angle will not necessarily be close to the actual average tilt angle of the system.[30] This is discussed further in Section 3.2.

2.2.7 Resonant Enhancement of the SHG Signal

If either the fundamental or the second harmonic frequency coincides approximately with an electronic transition of the interfacial medium, then a two-photon resonance will occur, increasing the non-linear susceptibility, and consequently the SH signal intensity, significantly. If the molecules at the interface have a transition at both fundamental and second harmonic frequencies, then they are said to be doubly resonantly enhanced, and the SHG signal will be very strong.

There are clear advantages in the use of molecules with a resonantly enhanced signal, as any signal arising from weaker effects from the bulk will be further diminished relative to the signal of interest. There can, however, be major disadvantages, such as fluorescence at the second harmonic frequency, which will add to, or even completely mask, the second harmonic response. In some instances, the absorption may lead to heating of the sample or breakdown of the interface. Neither of these problems arise in the crown ether systems investigated in this work for the incident or second harmonic frequencies employed.

2.2.8 Adsorption Isotherms

It is possible to study the thermodynamics of adsorption using SHG. The Langmuir model treats the liquid surface as a lattice of sites which may be empty or filled. The adsorption process may be thought of as the exchange between the bulk liquid and the empty sites on the interface, as shown by Equation 2.20 in Section

2.1. At equilibrium, the coverage, Θ, of the surface by the surfactant molecules (that is, the number of molecules adsorbed at the surface compared to the maximum possible number of molecules adsorbed) may be modelled by the Langmuir adsorption isotherm:

$$\Theta = \frac{\Gamma}{\Gamma_{max}} = \frac{Kc}{1+Kc} \tag{2.66}$$

K is the surface adsorption equilibrium constant.

The intensity of the SHG signal is proportional to the number of adsorbed molecules, through Equation 2.67:[28,31,32]

$$I(2\omega) = S\Theta^2 \tag{2.67}$$

Where S is a scaling constant. Using Equations 2.66 and 2.67, it is possible to determine the adsorption free energy, ΔG^{o}_{ads} using Equation 2.68.

$$\frac{1}{K} = 55.5exp\left(\frac{\Delta G^{o}_{ads}}{RT}\right) \tag{2.68}$$

The constant 55.5, is the molarity of water.

There are several important considerations when carrying out such analysis on SHG concentration dependence, since SHG is not only sensitive to the number of molecules at the interface, but also to the orientation of those molecules. It is possible to account for any orientational change during the isotherm,[33,34] if the polarisation dependence of the signal from the surface has also been studied. It is also possible that there exists a phase between the substrate signal and the adsorbate signal. If this is suspected, then it is best to separate these signals in order to see the true behaviour of the adsorbate.[27,35]

Summary of SHG Applications

In this chapter, the ways in which SHG may be applied to investigate the behaviour of surfactants has been explained. Surface SHG, as an all-optical spectroscopy, has

the considerable advantage over other surface specific techniques such as electron energy loss or electron diffraction, in that neither media needs to be in a vacuum for the measurements to be carried out. Thus, it may be applied to liquid/liquid or liquid/vapour as well as solid interfaces.

SHG has the advantage, over linear optical techniques, that the surface need not be the most populated part of the system, as no signal will arise from the bulk part, at least in the electric dipole approximation.

The technique is sensitive to both the orientation and the number density at the surface layer. It is highly surface specific, with an active layer of about 2 nm thickness.

2.3 Experimental Methods

2.3.1 Sample Preparation

When measuring surface properties of solutions, it is of great importance to ensure that the solution being studied is free from any surface active impurities. The solution must be surface-chemically pure.[4] Impurities may arise from the synthesis route of the chemical (reactants or side-products), from the storage containers used (leaching or cross-contamination), from the experimental containers (cross-contamination) or from the experimental location (dust).

When buying chemicals to use, it is vital to be aware that, for non-surface experiments, a chemical may be considered pure far before it is suitable to be used in surface studies. If the impurity is surface active, and especially if the impurity has greater surface activity than that of the chemical of interest, then it may obscure, or at least significantly alter the behaviour of the target species. Because the surfactants used in this study are partially soluble, and present on the surface only in very small amounts, this purity is particularly important.

Column Chromotography of the Crown Ethers

The crown ethers used in this work were bought from Fluka (>99% purity). As they were stored in glass containers, it was considered good practice to ensure that no ions were sequestered within the ether cavity by chromatographic separation. This should also separate any side-product or reactant material present in the bought compound.

The same procedure was used for both the benzo-15-crown-5 and the 4-nitrobenzo-15-crown-5: the compound was run through a silica 60 column, using a highly pure ethyl acetate eluent (spectroscopic grade). The ethyl acetate was then evaporated off from the crown fraction, resulting in white crystals. The nitrocrown purification resulted in yellow crystals. There was no clear way in which to determine any sodium presence, due to the extremely small sodium contamination which would affect the crown behaviour. Instead, multiple surface tension measurements and

SHG experiments were carried out to determine the effect of sodium complexation upon samples and the purity of the samples was determined on this basis, as will be described in the following sections. Most samples were stored in lidded Teflon vials until used.

Solutions for the experiments were made up in cleaned glassware and were always freshly prepared on the day of use to avoid any deterioration of the sample or leaching of ions.

Water

Obtaining water free from ions and organic contaminants was vital in order to carry out this work. It is possible that any ions may be sequestered by the ether cavity, and affect the surface behaviour of the molecule; any organic content might contribute to the surface tension reading and the SHG signal. For the majority of the work, the water used was obtained from a Barnstead E-pure 4-module purifier. This consistently had a high resistivity (18.2 MΩ cm) and a surface tension comparable to the literature value (72.8 N m^{-1} at 20°C).[1] The second harmonic polarisation response of the water was checked before the solutions were made up to ensure that there was no undetected contamination (see Figure 3.1 for a typical set of water polarisations).

Cleaning of Glassware

The glassware used during the experimental work to make up the solutions was thoroughly washed using the following sequence: acetone rinse, soapy water wash, pure water multiple rinse, dilute nitric acid wash and pure water multiple rinse (five or six thorough rinses).

2.3.2 Surface Tension Measurements: The Wilhelmy Plate Method

In this work, the pressure sensor on a NIMA trough was used to carry out the surface tension measurements, by the Wilhelmy plate method. A plate made from

filter paper is lowered into a teflon dish of solution, and then it is raised until it breaks the surface. The force taken to break the surface is reported, and from this, the surface tension is derived by:

$$F = \gamma P cos(\theta_r) \tag{2.69}$$

Where F is the total force on the plate, P is the perimeter of the plate, and θ_r is the contact angle between the plate and the surface.

A stock solution of the crown ether was made up for the experiment, using pure water and columned crown ether. A Teflon dish was used to hold the sample whilst measurements were taken. The dish was partially covered to minimise dust contamination, and the trough itself was thoroughly cleaned with ethanol and water, sequentially, before use. Measurements were taken on pure water initially, with a known volume in the sample dish. A measured aliquot of the water was then removed using a micropipette, and the same volume of stock solution was added. The removals and additions to the solution caused disturbance to the surface, and so a time of about 5 minutes between increasing the concentration and taking the measurement was allowed to ensure an equilibrium reading. Several surface tension measurements were taken at each concentration, until about four consistent readings (within 0.2 mN m^{-1}) were obtained. By continuing in this way, the surface tension was measured over a range of concentrations.

2.3.3 Second Harmonic Generation Experiments

The laser source used for this work is a Q-switched Nd:YAG laser (Continuum Minilite) with an output wavelength of 1064 nm. This output is then frequency doubled to 532 nm, and it is this wavelength which was used to promote SHG. The laser has a 5 ns pulse and a repetition rate of 20 Hz.

As shown in Figure 2.8 , the beam is directed through the input section of the setup using mirrors, at an angle of 60^{o} to the surface normal. The beam passes through a half-wave plate and a beam-splitting polariser. The beam-splitter con-

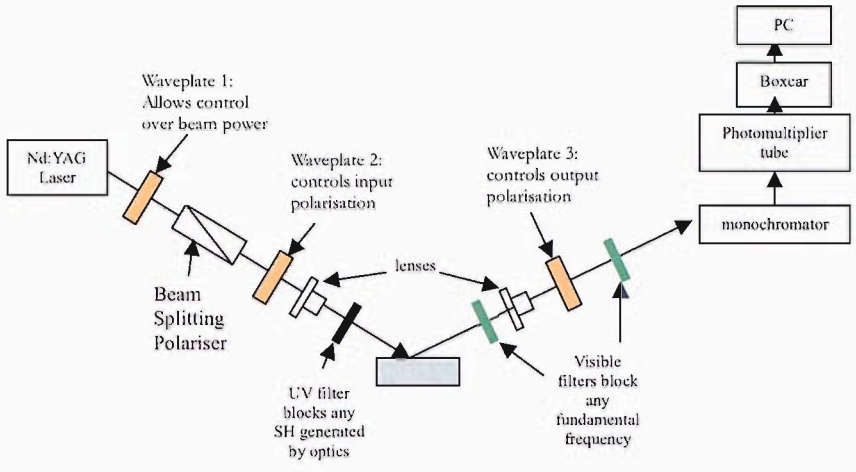

Figure 2.8: The laser setup used for the SHG experiments.

trols the input polarisation of the beam to allow the transmission of only *s*-polarised light - that is, light which is polarised perpendicularly to the plane of incidence. In this way, the half-wave plate before the beam-splitter may be used to control the power of the incident beam.

The beam then passes through a second half-wave plate, which is used to set the input polarisation angle, γ, of the incident radiation. At this point, the beam is passed through a double convex lens and is focused ($f \approx 160$ mm) on the surface being studied. A yellow glass schott UV filter is placed in front of the lens to remove any second harmonic signal generated thus far by the optics.

The beam is then reflected off the surface and is collected with a quartz plano-convex lens ($f \approx 150$ mm), and then through another polariser where the output polarisation of the beam, Γ, is set. The beam then passes through a focusing lens for recollimation, and on into the entrance slit of the monochromator (PT1, 1200 lines mm^{-1}). This is set at 266 nm. The beam then enters the photomultiplier tube, and further UG5 filters block out any remaining fundamental frequency. An A/D card linked to a PC digitises the outputs and a labView program is used to acquire the signal. The data is analysed using software written in Visual Basic (Version 5).

2.3.4 Experimental Procedure

For the polarisation dependence experiments, the intensity of the SH signal generated by the surface at three or four output polarisations, Γ, is recorded for several input polarisations, γ, covering the desired range (e.g 0-90°). At each $\gamma - \Gamma$ combination, the second harmonic signal generated over 1000 laser shots is recorded. These are then averaged to give the value for that combination. In this work, the input polarisation angle is usually increased in 7° increments over the range 0-90° for each value of Γ, giving 14 datapoints in each dataset. Between each change in Γ, a background signal reading is taken where the laser beam is blocked. This records the signal that is arising through electrical noise. The average background signal may then be deducted from each datapoint. For the concentration dependence experiments, the signal is measured at a specified $\gamma - \Gamma$ combination (chosen in order to maximise the signal, and the information which may be obtained) over a range of concentrations. The sample dish used in the SHG experiment was glass, as the laser will damage Teflon.

Summary

Great care must be taken in the preparation of solutions. The applications of crown ethers arise from their ability to selectively bind ions, and 15-crown-5 is of the correct size to bind with sodium ions. Unfortunately, this means that they cannot be stored for any period of time in glass containers (which is apparent from the work carried out during this project), as they will leach sodium ions from the glass. This means that the bought compounds, which are stored in glass, must first be run through a column to strip out any sodium, and then stored in Teflon. Solutions are made up in cleaned glassware, and are used only on the day they are made to prevent any sodium contamination.

Chapter 3

Experimental Results

3.1 The Pure Water/Air Interface

Numerous techniques have been employed in the study of the water/air interface, ranging from surface tension through to second harmonic generation (SHG) and sum frequency generation, and X-ray methods. The techniques used in this work are surface tension measurements and second harmonic generation experiments.

The second harmonic response of water is relatively weak. No resonant enhancement is seen, and in fact it is thought that the very weak response means that quadrupolar contributions may not be neglected in some instances. Consequently, many groups have studied the system at length to determine the actual SH response, and to separate it from any other contributions which may be affecting the measured signal.

3.1.1 Results from the Water/Air System

An initial important test on the purity of a water source is its resistivity. For pure water, this should be 18.2 MΩ cm at 25°C. This will decrease in the presence of ionic matter. Most modern water purification systems have a built-in resistivity monitor.

The surface tension of pure water has been widely studied, and is now accepted

as being 72.8 m Nm^{-1} at 20°C. The surface tension of water is a very good measure of its surface purity. Ion presence will tend to raise the surface tension, and organic presence will tend to decrease it.

Both the surface tension and the resistivity of the water from the source used were regularly checked. Small fluctuations were observed from day to day, but if the surface tension was found to be below 71 m Nm^{-1}, or a decrease in resistivity was seen, then the water was not used.

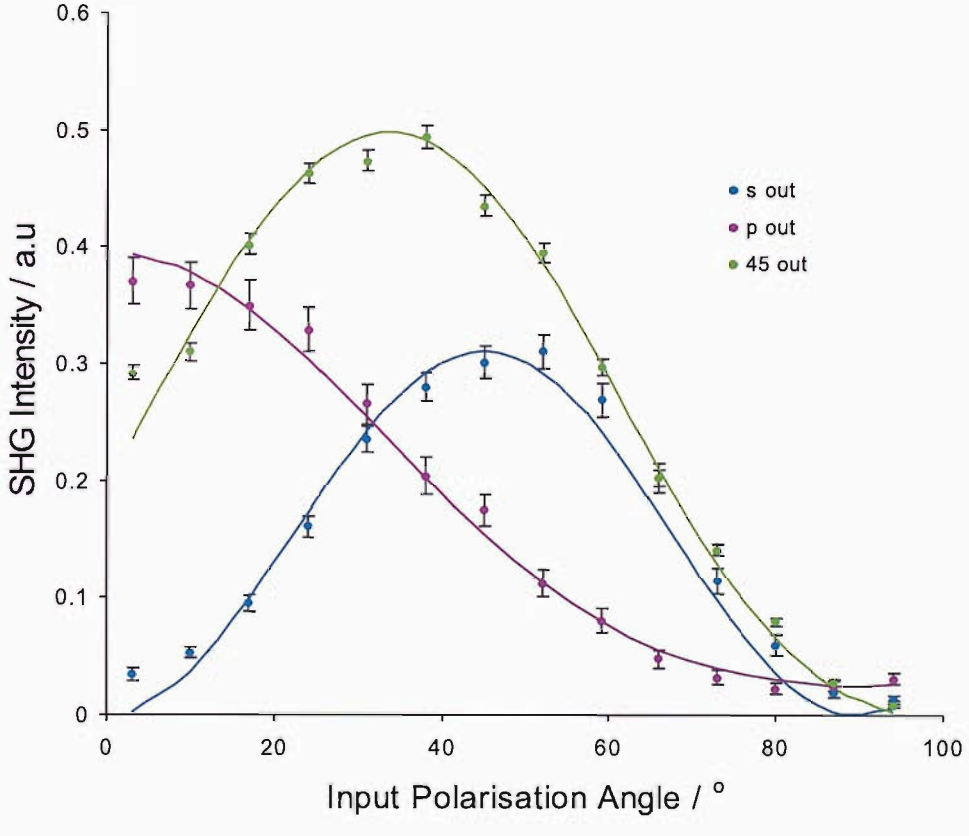

Figure 3.1: Typical set of polarisation dependence curves obtained from the pure water-air interface. The SHG signal is reported in arbitrary units (a.u.).

The second harmonic response of water has been measured many times throughout the course of this project, and has been compared to various other sources of purified water. A typical set of curves obtained from water with both surface tension and resistivity within the required range are presented in Figure 3.1.

Analysis of several datasets for the pure water/air interface throughout the project gives the parameters shown in Table 3.1.

χ_{zxx}/χ_{zzz}	χ_{xzx}/χ_{zzz}	B/A	C/A
0.121(0.01)	0.295(0.01)	0.273(0.02)	0.869(0.01)

Table 3.1: Average ratios from several datasets for the pure water/air interface, along with standard error values. A, B and C parameters are defined in Section 2.2, Equations 2.51 to 2.53.

These values compare well to those obtained by Tamburello-Luca *et al.*,[36] Fordyce *et al.*[37] and to the theoretically calculated data by Sokhan and Tildesley[38] (see Table 3.2). The data of Goh *et al.*[39] differs somewhat from the data reported in this project, and in the compared references.

Group	χ_{zxx}/χ_{zzz}	χ_{xzx}/χ_{zzz}
Goh *et al.*[39]	0.385	0.833
Tamburello-Luca *et al.*[36]	0.159	0.385
Sokhan and Tildesley *et al.*[38](MD simulations)	0.139	0.169
Fordyce *et al.*[37]	0.149	0.274
This work	0.121(0.01)	0.295(0.01)

Table 3.2: The χ_{ijk} ratios derived for the pure water/air interface in this work, and in the literature

Summary

The results obtained from the pure water interface in this project are compared to previous studies. There is good agreement with most of the literature, and consistent results are obtained from the water sources used for this work.

Using three techniques to verify different aspects of the purity of the water means that any deterioration in the water source could be noticed at an early stage, and use of contaminated water was avoided.

3.2 Benzo-15-Crown-5 at the Air/Water Interface

Previous Work

The literature resources on crown ethers with respect to complexation are massive, due to the high selectivity the compound show for specific cations. Since the first crown ethers were synthesised[40] through to a major study by the US Department of Energy,[41] crown ethers have been of great interest in applications from solubility to catalysis, and from supramolecular layers to radionuclide extraction from waste eluent. Much data is available with regards to complexation parameters. The crown ether size which has received much of this attention is 18-crown-6 (18C6). This is largely due to the applications of this compound in supramolecular chemistry. The 18C6 cavity is of the correct size, at 2.6 to 3.2 Å,[42] to sequester K^+ ions (ionic diameter of 2.66 Å) and Ba^{2+} (2.70 Å).

An early paper by Vandegrift[43] discussed some 18C6 compounds and complexes: 18C6, dicyclohexyl-18-crown-6 (two isomers) and the complex of the dicyclohexyl compound with $Ba(NO)_3$. The surface tensions of the compounds with concentration were measured, and from the data, using the Gibbs' isotherm, the minimum areas occupied per molecule were calculated. The dicyclohexyl (DCH) compounds were much more surface active than the non-functionalised crown, as expected, and the areas were reported as 70 $Å^2$ per molecule for the 18C6, 114 $Å^2$ per molecule for isomer A of DCH-18C6, 128 $Å^2$ per molecule for isomer B, and then 87 $Å^2$ per complex for DCH-18C6 (isomer A) in the presence of $Ba(NO)_3$. The hydration of free 15-crown-5 (15C5) and 18-crown-6 (18C6) has been studied as the conformations of hydrated crowns have implications in what ions will be bound by the crown, and how.[44]

Another major field in which crown ethers are rapidly establishing themselves is synthesis. The solubilisation of salts in organic solvents by crown ethers is one characteristic which has opened up synthesis routes previously unavailable.[45] Similarly, they have applications in catalysis.[46]

More recently, much more highly functionalised crown ethers have been studied by the US Department of Energy as a means of cleaning up nuclear effluent of radioactive ions.[41,47–49] This work has proved highly successful in functionalising calix-arene crown ethers to enhance their selectivity for caesium and strontium ions.

At the water-air interface, much work has been carried out on Langmuir films of hydrophobically functionalised crown ethers.[2,3,50,51] Again, the emphasis is on the addition of ions, and the ion-selectivity. Information on uncomplexed crown ethers is generally found within studies which then proceed to focus on the complexed behaviour. Clearly, it is in complexation applications that crown ethers are invaluable. However, it is important to understand how crown ethers behave in their free form in order to fully characterise the changes and behaviour which occur on the addition of ions. It is the aim of this project to characterise as fully as possible the surface behaviour of two crown ethers at the water-air interface.

Benzo-15-crown-5, studied at the water-air interface in this work, has previously been studied in aqueous-organic solvent mixtures,[52–54] and enthalpies of solvation are reported for several mixtures. The transfer of alkali metal ions between polar solvents using benzo-15-crown-5 has also been studied.[55] Some more surface active derivatives have been used for monolayer studies on aqueous electrolyte solutions using potentiometry.[51]

Benzo-15-crown-5 is an aromatic crown ether (Figure 3.2), and is estimated to have an area of about 74-77 $Å^2$ in its flattest conformation. The compound has a solubility of 29.51 g L^{-1} in water (at 25°C).[56]

3.2.1 Surface Tension Results

Benzo-15-crown-5 was obtained from Fluka (> 99% purity). Initial surface tension experiments on the aqueous solution of benzo-15-crown-5 were carried out on the compound as bought. The compound is delivered in glass bottles from the sup-

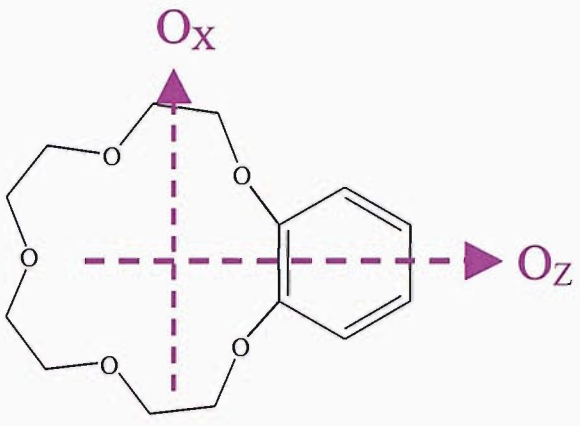

Figure 3.2: Diagram of benzo-15-crown-5, including the molecular axis convention used in the SHG work.

plier, and since it is known that the 15-crown-5 cavity size (about 1.7 to 2.2 Å diameter)[42] is suitable for sequestering sodium ions (ionic diameter of 1.9 Å), it is possible that storage in glass, which contains some sodium, may lead to the presence of a proportion of sodium-complexed crown ether. As the aim of this project is the study of uncomplexed crowns, the compound was then run through a silica column in ethyl acetate (spectroscopic grade) to strip out any sodium present. One batch of columned compound was stored in glass after columning, and surface tension measurements were taken within weeks of cleaning, and then again a few months later. Surface tension measurements on benzo-15-crown-5 aqueous solutions were taken over the bulk concentration range 0 to 5 mM. The results, plotted in Figure 3.3, show clearly that glass storage does affect the surface behaviour of the crown ether. The early data differs from that of the untreated, glass stored compound, but the later data is consistent with the untreated compound. It appears that the crown is more surface active after storage in glass, which is likely to be due to some promotion or stabilisation of surface behaviour by sodium ions. One sample of benzocrown (although not the most pure) was run both in the absence, and in the presence, of NaCl (excess), and the resulting isotherm, shown in Figure 3.4, does indeed correspond well to that of the crown ether which was not columned. Subsequent batches of columned compound were stored in Teflon vials, to assure that no complexation took place. Surface tension measurements

performed on such batches show consistent behaviour, even if left for some time in storage. This would seem to verify that glass storage of the compound is not acceptable for surface experiments. Consequently the results which shall be discussed hereafter are those for the columned crown ether which has been stored in Teflon.

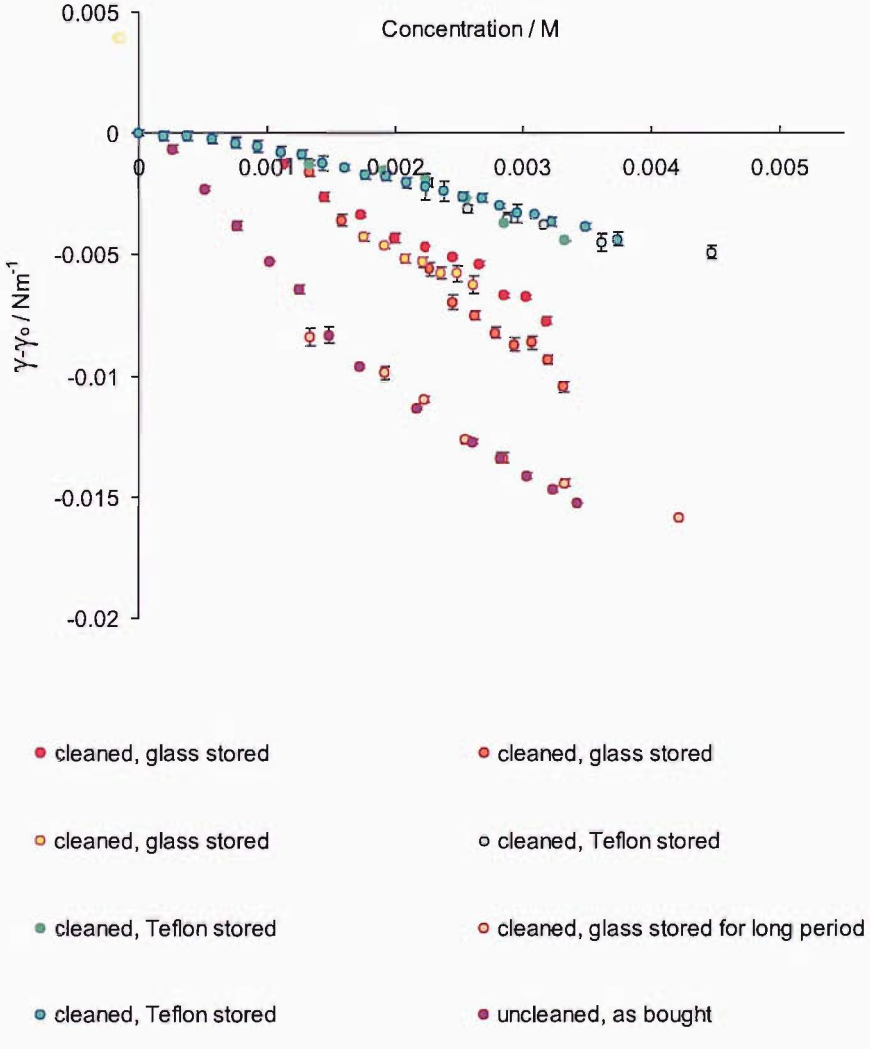

Figure 3.3: Plots of $\gamma - \gamma_o$ against bulk concentration for a series of samples of benzo-15-crown-5.

Taking a single representative dataset for the concentration range (Figure 3.5) which includes several readings in the very low concentration region, the surface

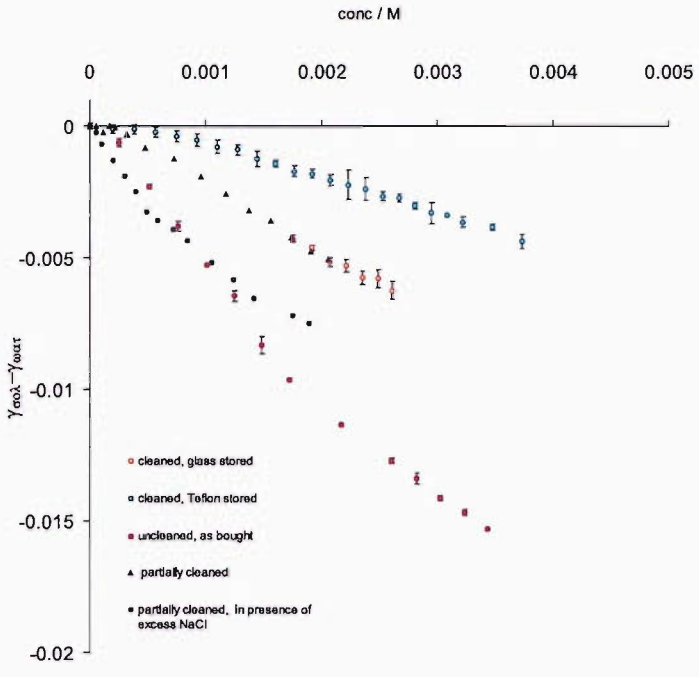

Figure 3.4: Plot of $\gamma - \gamma_o$ against bulk concentration for a batch of benzo-15-crown-5 with and without excess sodium chloride present in the solution. One cleaned, glass-stored and uncleaned sample from the previous plot are also included for reference.

tension data were first fitted using a cubic polynomial. From this, the derivative was obtained, and this was used to calculate the surface excess (using Equation 2.16). This may be used to obtain an estimate of the area per molecule as a function of bulk concentration, and this is plotted in Figure 3.6. The minimum area per molecule was then derived from the surface excess using the Szyszkowski equation of state (Equation 2.21) as being 67 $Å^2$ per molecule. This is a smaller area than the flat area of one crown ether, and suggests that the crowns pack fairly closely on the interface at higher bulk concentrations.

3.2.2 SHG Results

From the UV spectrum, shown in Figure 3.7, benzo-15-crown-5 is seen to absorb light at 266 nm. This indicates that a good second harmonic response should be obtained due to resonant enhancement of the signal.

The extinction coefficient is shown to be 1780 M^{-1} cm^{-1} at the second har-

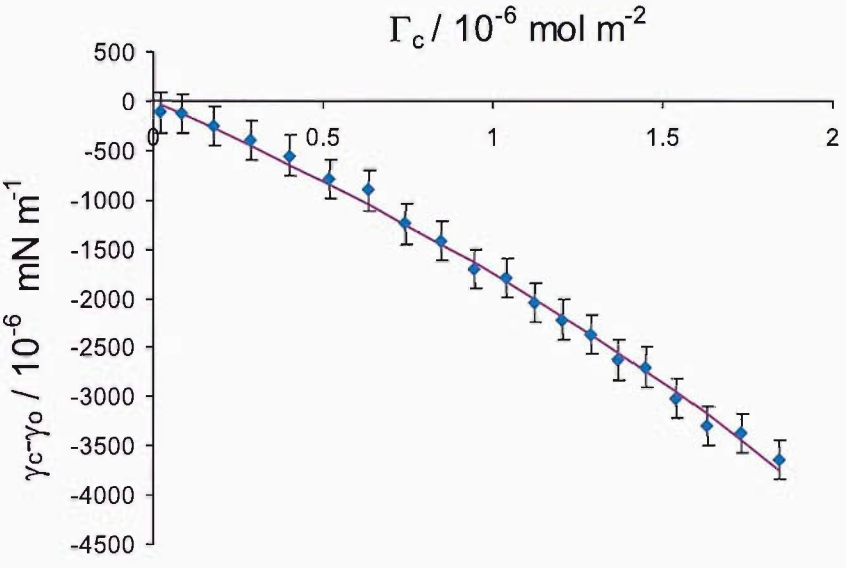

Figure 3.5: Plot of $\gamma_c - \gamma_o$ against Γ_c for a cleaned and Teflon stored sample of benzo-15-crown-5. 10% error bars are shown.

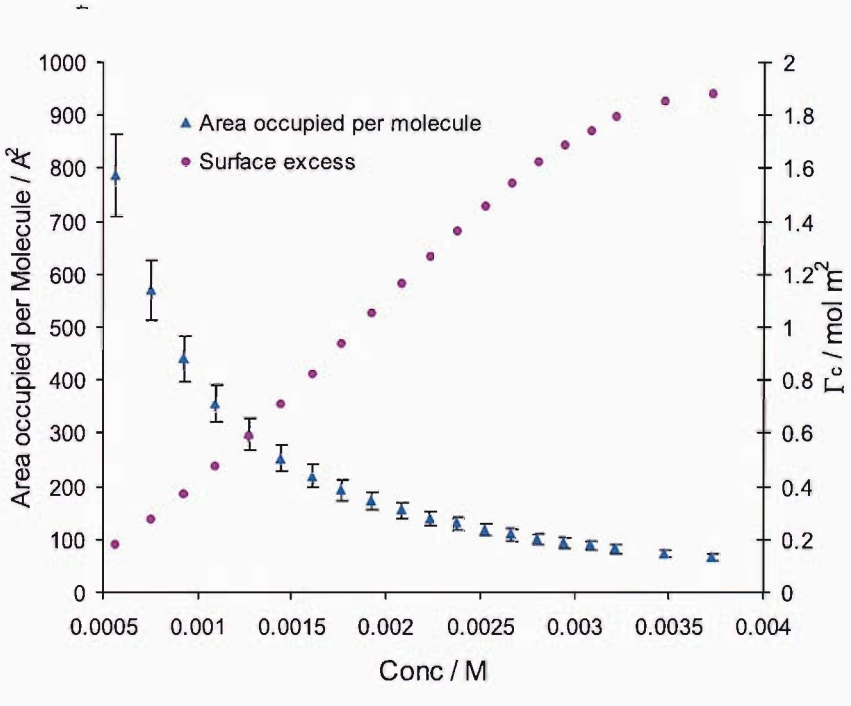

Figure 3.6: The derived area occupied per benzo-15-crown-5 molecule over the concentration range studied, for the cleaned and Teflon stored sample.

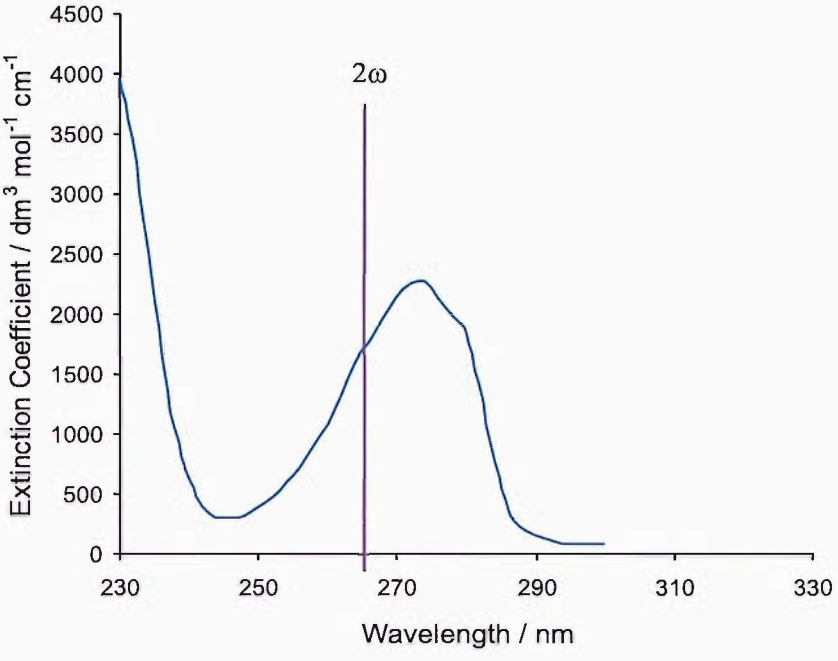

Figure 3.7: The UV-vis spectrum of a 0.5 mM benzo-15-crown-5 aqueous solution: the absorption around the second harmonic wavelength of the SHG experiment (266 nm) indicates that the SHG signal will be enhanced.

monic wavelength, and from this, along with the assumption that the interfacial refractive index is the average of that of the bulk water and that of the air (see Table 3.3), the a_i coefficients required for the SHG polarisation dependence may be calculated. These are presented in Table 3.4.

Parameter	For fundamental frequency	For Second Harmonic Frequency
Wavelength λ	532 nm	266 nm
Angle of Incidence	60°	-
Extinction Coefficient, ε		1780 M^{-1} cm^{-1}
n_{air}	1	1
n_{water}	1.334	1.334
n_{int}	1.167*	1.167*

Table 3.3: Parameters used to calculate the a_i coefficients. * indicates this is the preliminary value used.

a_i	Re	Im
a_1	0.259	0.00
a_2	-0.222	0.00
a_3	0.126	-0.006
a_4	0.157	-0.007
a_5	0.194	-0.009

Table 3.4: Calculated a_i coefficients for benzo-15-crown-5.

3.2.3 Polarisation Dependence

Two batches of columned, Teflon stored benzo-15-crown-5 are reported here. There are slight differences in the data obtained under the assumptions specified, although the datasets do compare well. The differences, and possible explanations will be discussed.

Polarisation curves were run at several bulk crown ether concentrations within the range studied using surface tension measurements. In terms of the appearance of the plots, no difference was apparent between concentrations, although the intensity of the signal rose with increasing concentration.

These results were analysed using Equations 2.49 to 2.54, but the graphical fitting procedure to these curves was carried out in two different ways: direct A, B and C fitting, and D, R and F fitting.

Direct A, B and C fitting (ABC)

In this case, the curves were fitted directly by Equations 2.49 to 2.54, using an Excel spreadsheet which optimised the values of χ_{ijk} (and thus A, B and C) through the least squares method. Once the data is fitted, it is possible to then calculate the order parameter D for several assumptions on both the dominant hyperpolarisability components, and on the Euler angle ψ, relating to the rotation of the molecule about its long axis (as shown in 2.2).

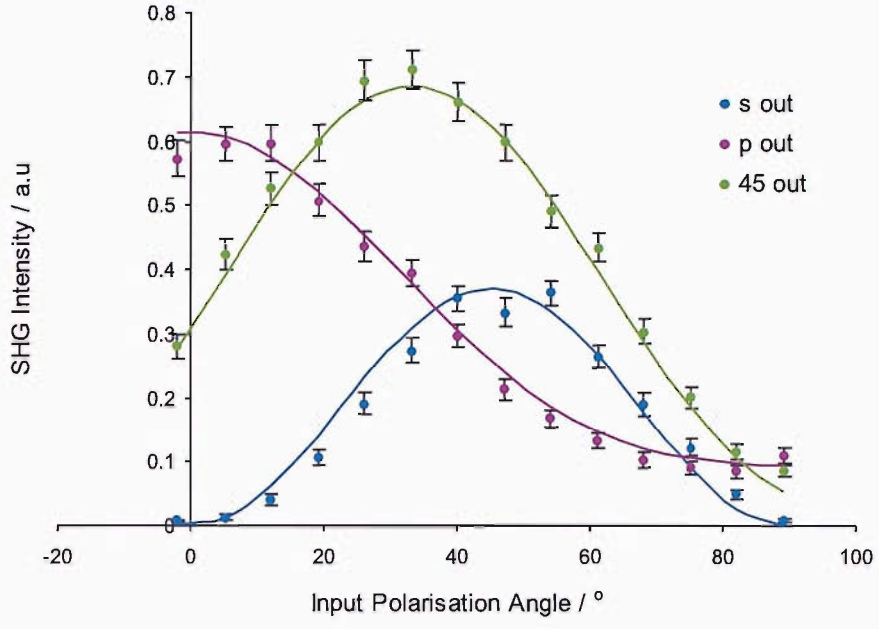

Figure 3.8: Typical set of polarisation curves for benzo-15-crown-5 (This set obtained from a 4 mM solution).

Fitting using D, R and F parameters (DRF)

The results of some *ab initio* calculations were obtained[57] on the chromophore of the crown ether to determine which hyperpolarisability components are likely to be the dominant ones. It is expected that the chromophore, having C_{2v} symmetry will have the dominant hyperpolarisability components β_{zzz} and β_{zxx}, as has been determined on systems of similar symmetry. The calculations support this assumption, and being confident in the dominance of these components allows a slightly different approach to the fitting of the SHG polarisation dependence data.

Once the significant hyperpolarisability components have been determined, expressions for each non-linear susceptibility component may be derived in terms of the order parameter, D, the ratio of the dominant hyperpolarisability components, R, and a scaling factor, F. Further assumptions are taken regarding the Euler angle distributions, which will be discussed in more depth in Section 6.1.

As discussed, for the case of benzo-15-crown-5 the β_{zzz} and β_{zxx} components are assumed to be dominant. Additionally, it is assumed that the angle of rotation

about the molecular axis, ψ, is random, and that the distributions of the angles ψ and θ are independent of each other. The equations for each χ component are:

$$\chi_{zzz} = F\left[2D + (1-D)R\right] \tag{3.1}$$

$$\chi_{zxx} = F\left[(1-D) - \frac{R}{2}(1-D) + R\right] \tag{3.2}$$

$$\chi_{xzx} = F\left[(1-D) - \frac{R}{2}(1-D)\right] \tag{3.3}$$

where:

$$D = \frac{\langle cos^3\theta \rangle}{\langle cos\theta \rangle} \tag{3.4}$$

$$R = \frac{\beta_{zxx}}{\beta_{zzz}} \tag{3.5}$$

$$F = \frac{N}{2\varepsilon_o}\langle cos\theta \rangle \beta_{zzz} \tag{3.6}$$

and R may be complex.

The χ_{ijk} found through Equations 3.1, 3.2 and 3.3 are then used within Equations 2.49 to 2.54 to fit the curves. Fitting in this way reduces the number of variables, but imposes extra restrictions on the analysis through the additional assumptions.

In fact, the results from these two fitting methods in this case were the same within experimental errors. The sets of ratios derived by both methods are included for comparison.

The difference between the two sets of data is surprising, as they are readings taken from data obtained on samples which were treated in exactly the same way. Looking at the appearance of the curves from each set of data, shown in Figures

3.9 and 3.10, the difference lies in the shape of the P-out curve. For Sample 1, the data has a P-out curve which tends to zero at a 90^{0} (S) input polarisation, but for Sample 2, the P-out curve does not fall to zero. It remains at significant intensity. The cause of this could be contamination by ions, since it was observed that the untreated compound gave a similar P-curve, but with a more pronounced tail, as seen in Figure 3.11.

Both sets of data do indicate that no significant change in the tilt angle is observed, and this is supported by the smoothness and simple fit of both the surface tension data and the SHG isotherm data.

Sample	Conc/mM	χ_2/χ_1	χ_3/χ_1	B/A	C/A	R	D	$\theta_{app}/^o$
1, ABC fit	1.5	0.144(0.010)	0.301(0.010)	0.271(0.014)	0.747(0.060)	0.225(0.030)	0.660(0.010)	35.3(0.30)
	3.0	0.192(0.010)	0.318(0.010)	0.358(0.020)	0.775(0.010)	0.146	0.640(0.010)	36.8(0.30)
	4.0	0.215	0.302	0.395	0.777	0.239	0.66	35.8
1, DRF fit	1.5	0.147(0.01)	0.301(0.01)	0.342(0.100)	0.763(0.040)	0.243(0.02)	0.66(0.01)	35.7(0.5)
	3.0	0.201(0.01)	0.322(0.002)	0.386	0.778	0.154(0.02)	0.635(0.01)	37.1(0.2)
	4.0	0.185(0.01)	0.318(0.01)	0.344	0.778	0.162	0.64(0.01)	36.8(0.4)
2, ABC fit	0.7	0.392	0.389	0.669	0.874	0.017	0.561	41.5
	0.8	0.361	0.412	0.649	0.975	0.055	0.562	41.4
	1.5	0.249(0.030)	0.355(0.010)	0.446(0.030)	0.838	0.125(0.014)	0.612(0.010)	39.9
	2.0	0.340	0.391	0.634	0.960	0.103	0.587	40.0
	3.0	0.339	0.374	0.561	0.825	0.074	0.584	40.2
	3.5	0.361(0.050)	0.370(0.050)	0.596(0.110)	0.804(0.140)	0.137(0.051)	0.589(0.030)	41.3(1.5)
	4.0	0.298	0.365	0.518	0.846	0.123	0.629	39.9
2, DRF fit	0.7	0.413	0.406	0.670	0.877	0.09	0.551	42.1
	0.8	0.360	0.413	0.602	0.920	0.296	0.573	40.8
	1.5	0.244(0.010)	0.355(0.010)	0.432(0.020)	0.838(0.010)	0.204(0.070)	0.616(0.01)	38.4(0.05)
	2.0	0.335	0.400	0.582	0.927	0.153	0.574	40.8
	3.0	0.328	0.379	0.557	0.859	0.059	0.581	40.3
	3.5	0.369(0.050)	0.381(0.060)	0.592(0.103)	0.818(0.153)	0.215(0.014)	0.581(0.040)	40.4(2.2)
	4.0	0.290	0.367	0.502	0.848	0.089	0.595	39.5

Table 3.5: Ratios and Parameters derived by the ABC and the DRF method. Both samples **1** and **2** were treated in the same way: that is, the bought compound was run through a silica column with ethyl acetate. Standard errors are reported in brackets for multiple dataset results.

Concentration Dependence

The concentration dependence of the (P-in, P-out) (γ, Γ) combination was measured over the same range as that studied by surface tension. This combination was chosen to ensure that a maximum signal was obtained. The intensity of the SHG signal can be related to the surface coverage through:

$$I(2\omega) = S\Theta^2 \tag{3.7}$$

Where Θ is the coverage of the surface by the species, as given by Equation 3.8, and S is a scaling factor.

$$\Theta = \frac{Kc}{1+Kc} \tag{3.8}$$

Here, K is the Langmuir adsorption constant, and is given by Equation 3.9, and c is the concentration of the species.

$$K = \frac{k_{adsorption}}{k_{desorption}} \tag{3.9}$$

It must be noted that care needs to be taken in relating the coverage to the intensity of the second harmonic signal, as this is known to be orientation dependent as well as coverage dependent. Thus, any intensity dependence on orientation must be studied alongside the concentration dependence. In this case, it has been seen that there is no change in orientation with concentration, or at least, no change detected by the SHG measurements. This simplifies the analysis of the isotherm.

The relationship between the effective susceptibility tensor ($\chi^{(2)}$ from which, hereafter, the superscript (2) will be omitted, as all χ terms are second order susceptibilities), and the intensity of the second harmonic signal is given by Equation 3.10.

$$I(2\omega) \propto \left|\chi^{eff}\right|^2 \tag{3.10}$$

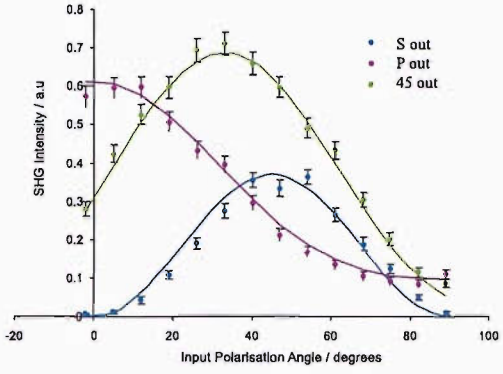

Figure 3.9: One set of polarisation curves from Sample 1

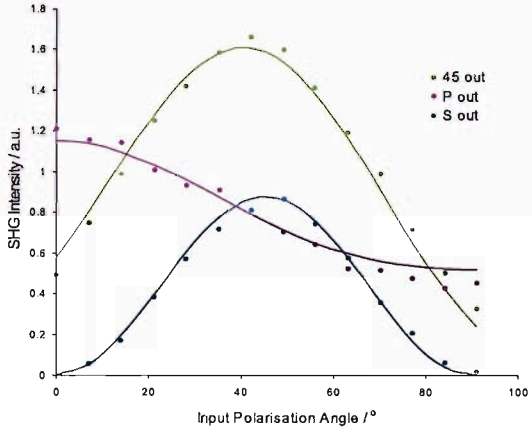

Figure 3.10: One set of polarisation curves from Sample 2.

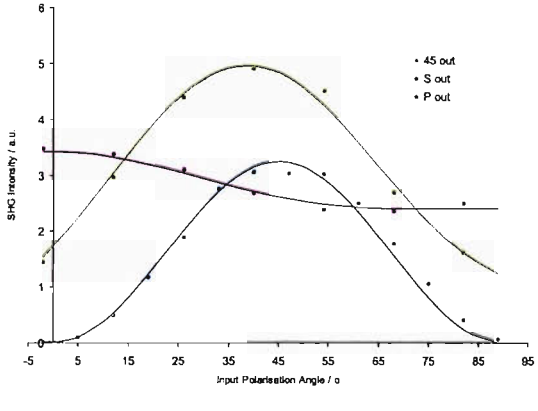

Figure 3.11: One set of polarisation curves from an uncolumned batch.

For the system studied the intensity of the signal from a crown ether solution is at most, over the range studied, only twice that of the bare water interface. Thus, the contribution from both crown and water should be considered separately. χ^{eff}, has two contributions, the χ^{wat} contribution, from water, and the χ^{cro} contribution, from the crown ether. The relationship from Equation 3.10 thus becomes:

$$I(2\omega) \propto I^{wat} + I^{cro} = \left|\chi^{wat} + \chi^{cro}\right|^2 \tag{3.11}$$

The expansion of the right hand side of Equation 3.11 depends upon any phase difference between the signals from the water and from the crown. The general expansion is shown in Equation 3.12.

$$I(2\omega) \propto \left|\chi^{wat}\right|^2 + \left|\chi^{cro}\right|^2 + 2\left|\chi^{wat}\right|\left|\chi^{cro}\right| cos\phi \tag{3.12}$$

Where *phi* is the phase between the electric field of the water signal and the crown signal. The quantity which is proportional to the coverage, as shown in Equation 3.7 is the square root of the intensity of the SH signal; that is, the electric field of the second harmonic signal. The correct expression for this depends upon the phase difference between the water and crown signals. For example, of the signals are in phase, then the expression for the electric field is shown in Equation 3.13. If the phase is 90^o, the electric field is given by Equation 3.14.

$$E(2\omega) \propto \left|\chi^{wat}\right| + \left|\chi^{cro}\right| \tag{3.13}$$

$$E(2\omega) \propto \sqrt{\left|\chi^{wat}\right|^2 + \left|\chi^{cro}\right|^2} \tag{3.14}$$

For the data from benzo-15-crown-5, two different cases were considered in order to obtain a good fit of the data: that where the phase between crown signal and water signal, ϕ, was 0^o and that where it was 90^o. An equally good fit is obtained under both these assumptions (see Figure 3.12), and the technique is not sufficiently sensitive to determine the phase accurately for low concentrations of

benzo-15-crown-5 in water.

The value of K was therefore derived for both cases, and subsequently the value of ΔG_{ads}. These are presented in Table 3.7.

Assumed Phase	K / dm^{3}mol^{-1}	ΔG_{ads} / kJ mol^{-1}
0	816±65	-26.3±0.1
90	2162±70	-28.7±0.1

Table 3.6: Parameters derived from the adsorption isotherm using two different assumptions of phase.

The successful fit of the Langmuir isotherm supports the findings that there is no significant change the way in which the benzo-15-crown-5 packs in this system with concentration; at least, no change which is detectable by SHG.

3.2.4 Discussion

Taking the results of all three experimental techniques on this compound, it can be concluded that there is no significant change in the orientation of the crown ether at the interface with increasing concentration. If there was, then the polarisation dependence studies would reveal this change. This is supported by the smooth concentration dependence of surface tension, and also by the good fit of a simple Langmuir isotherm to the concentration dependence of the SH response.

The difference between the surface excess derived from surface tension measurements and the SHG isotherm is pronounced at low concentrations. This is most likely to be due to the influence of the order parameter $\langle P_1 \rangle$ on the shape of the SHG data. The surface tension is affected by the number of crown ethers at the surface alone, whereas the SHG concentration isotherm is affected by the surface concentration and by the orientation at the surface. Although the data seems to be approaching the weak limit, it is not strictly weak limit, especially at low concentration, and thus, it is possible that the order of the molecules is influencing the shape of the adsorption isotherm.

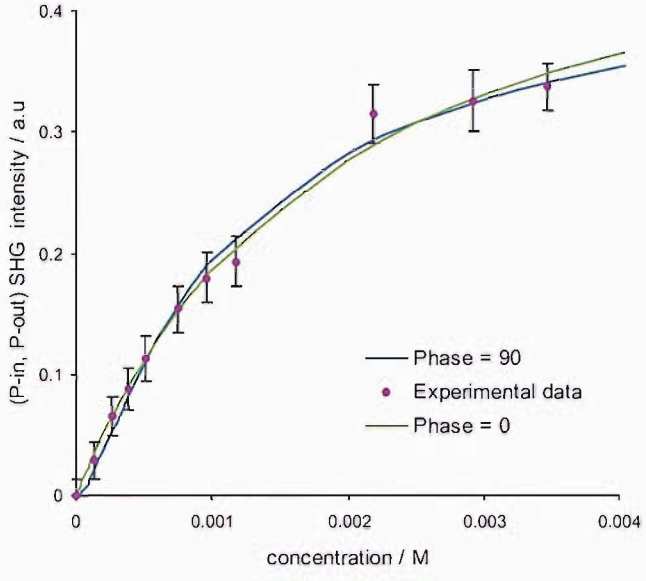

Figure 3.12: The SHG isotherm obtained for the P-in, P-out signal. The data has been fit by the Langmuir isotherm assuming a phase of 0, and of 90°

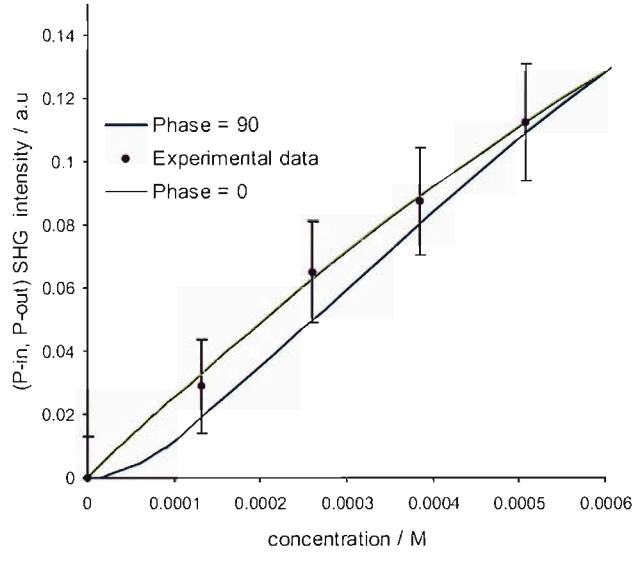

Figure 3.13: Low concentration region of the Langmuir plot showing the difference in shape between the phase=0 and phase=90 curves. The error bars indicate that this experiment is not sensitive enough to distinguish between these cases.

It is interesting to note that in fact the SHG technique may not be sensitive enough to probe this system fully. The signal enhancement is surprisingly weak in the system, and the conclusion which best explains the data is that the molecules are in the weak limit of interfacial order.

The tilt angle throughout the concentration range is between 35 and 45°. This suggests that the interfacial molecules are not well ordered enough to use the approximation that $D \approx cos\langle\theta\rangle^2$.[24,30] This approximation is valid only for systems where there is a very narrow distribution of tilt angles about the mean value. Except in the case of a tightly packed monolayer, it is reasonable to expect that there is some distribution about the mean tilt angle. Even slight deviation from a sharply unimodal tilt angle distribution leads to a D value which gives a θ value diverging from the true mean. It is found that the apparent tilt angle calculated using the approximation that $D \approx \langle cos^2\theta\rangle$ converges towards 39.2°, which has been called the "SHG magic angle".[30]

This magic angle may be derived from the expressions for D. If we take the example of a system, such as benzo-15-crown-5 at the water/air interface, where the dominant β components are β_{zzz} and β_{zxx}, then the order parameter may be expressed as in Equation 3.15.[27]

$$D = \frac{\langle cos^3\theta\rangle}{\langle cos\theta\rangle} = \frac{\chi_{zzz} - \chi_{zxx} + \chi_{xxz}}{\chi_{zzz} - \chi_{zxx} + 3\chi_{xxz}} \tag{3.15}$$

It has also been shown that when the system is weakly ordered, the components of χ are not independent; they are related through Equation 3.16,[58] for two equivalent incident fields.

$$\chi_{zzz} = \chi_{zxx} + 2\chi_{xzx} \tag{3.16}$$

Also, for two equivalent incident fields, $\chi_{ijk} \equiv \chi_{ikj}$. Thus, the dependence in Equation 3.16 simplifies Equation 3.15 to:

$$D = \frac{3\chi_{xzx}}{5\chi_{xzx}} = \frac{3}{5} \tag{3.17}$$

Using the approximation that $D \approx cos\langle\theta\rangle$ will therefore always result in a value of θ_{app}=39.2°, whatever the true value of the mean tilt angle may be.

If we assume the data to lie in the weak order limit, then it is possible to estimate the interfacial refractive index of the system,[24] which thus far has been assumed as the average refractive index of the two bulk phases, taking n_{air} as unity and n_{water} as 1.334.

Concentration / mM	n_{int}	water-like or air-like
0.7	1.122	air
0.8	1.172	water
1.5	1.219(0.025)	water
2.0	1.179	water
2.5	1.060	air
2.7	1.060	air
3.0	1.175(0.025)	water
3.5	1.189	water
4.0	1.199(0.03)	water
Average	1.179(0.01)	water

Table 3.7: Interfacial refractive index obtained assuming that data is in the Weak order limit. Where more than one dataset is used, the standard error is reported in brackets.

The average derived n_{int} is reported in Table 3.8. In general it appears that the refractive index of the interface is slightly weighted towards that of the water.

If the weak limit is assumed for the system, then the datasets may be fitted, using the D, R, F method with D fixed at 3/5. A good fit is obtained with the data when this is done, supporting the theory that the crown ether is weakly ordered. In itself, the weak order limit does not adequately describe the system, as there are several interfacial arrangements that could result in this outcome - for example, a tightly packed and ordered layer with alternating head to tail crowns. For this

reason, the computational simulations are of great interest. Molecular dynamics enables an atomistic study of the system, and no experimental technique can offer this on a liquid/vapour system to date.

3.3 4-Nitrobenzo-15-Crown-5

The 4-Nitrobenzo-15-crown-5 molecule (Figure 3.14) differs from the benzo-15-crown-5 only in the presence of the electron withdrawing nitro group. The axes used in the analysis of the data are also shown in Figure 3.14. These are defined based on the convention that the O_z, or molecular, axis runs from the donor to the acceptor group, and the O_x axis is perpendicular to O_z, and also in the plane of the molecule.[5]

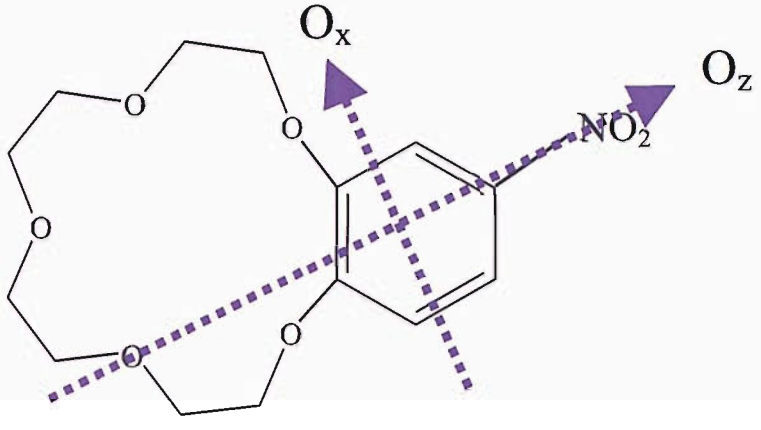

Figure 3.14: Diagram of 4-nitrobenzo-15-crown-5, showing the molecular axes used for the SHG work.

The solubility data on 4-nitrobenzo-15-crown-5 was not available, but it was not found to be very soluble in water. Treatment of solutions with heat and ultrasound were necessary even for low concentration solutions.

3.3.1 Surface Tension Results

The surface tension isotherm of the compound was very similar in shape to that of benzo-15-crown-5. Once again, it was found that the columned compound showed less surface activity than the bought compound: the surface tension of the bought (glass stored) sample decreased more steeply than that of the columned, Teflon stored sample (see Figure 3.15).

The surface excess was derived at each concentration along the surface tension isotherm using the Gibbs adsorption isotherm, and the area per molecule was de-

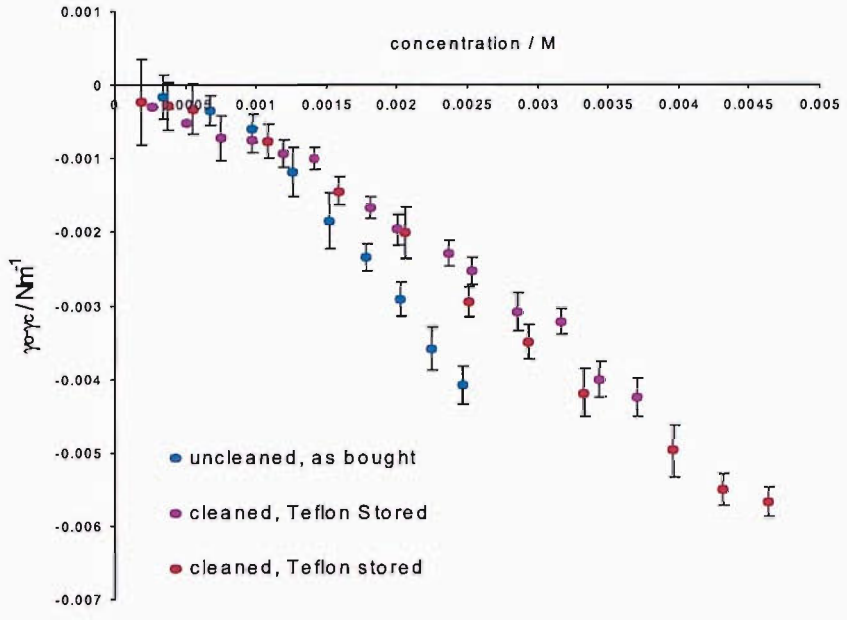

Figure 3.15: Three surface tension isotherms obtained from 4-nitrobenzo-15-crown-5, one of which is from an uncolumned sample.

rived. Both the surface excess and the area per molecule are plotted in Figure 3.16.

UV-visible Spectrum and Optical Data

The UV-visible spectrum of the nitrocrown indicates that there will be very little resonant enhancement of the SHG signal, as it only absorbs weakly at 266 nm. The optical data used for the SHG interpretation is given in Table 3.8.

Parameter	For fundamental frequency	For Second Harmonic Frequency
Wavelength λ	532 nm	266 nm
Angle of Incidence	60^{o}	-
Extinction Coefficient, ε		520 M^{-1} cm^{-1}
n_{air}	1	1
n_{water}	1.334	1.334
n_{int}	1.167*	1.167*

Table 3.8: Parameters used to calculate the a_i coefficients. * indicates this is the preliminary value used.

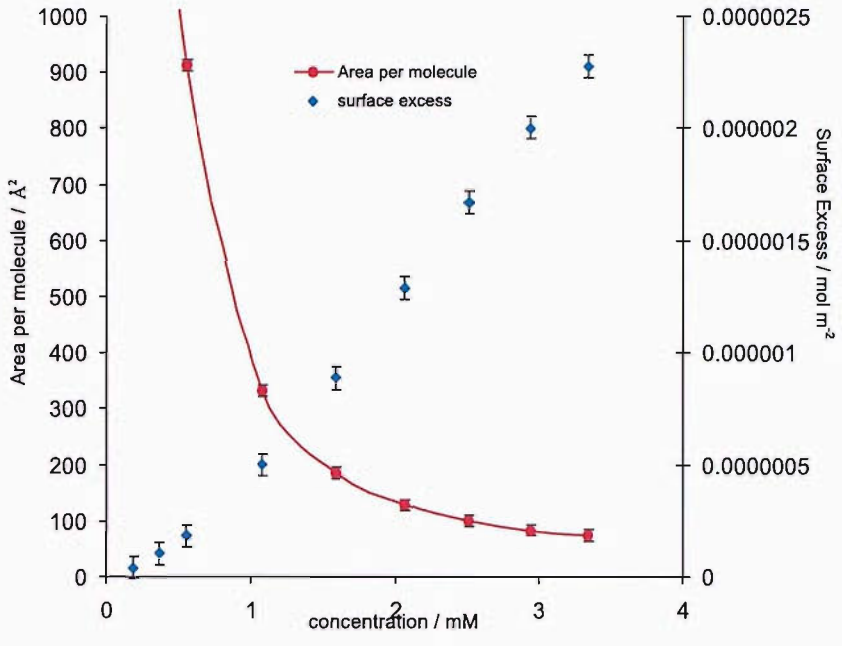

Figure 3.16: The derived surface excess and area occupied per molecule for a columned sample of 4-nitrobenzo-15-crown-5. The line through the area curve is to guide the eye.

3.3.2 Second Harmonic Generation

Polarisation Dependence

The polarisation dependence curves of 4-nitrobenzo-15-crown-5 were obtained over a similar concentration range as those for the benzocrown. At low concentrations, the S-out polarisation curves are visibly at lower intensity to those of the pure water/air interface, shown in Figures 3.18 to 3.20. As the concentration is raised, the intensities increase. At higher concentrations, the signal from the nitrocrown solution becomes much stronger than that of water. This behaviour suggests that there exists a phase difference between the SHG electric field of water and nitrocrown, both of which are contributing (and contributing significantly at lower concentrations) to the detected SH response.

Polarisation dependence curves at several concentrations were measured for both the glass-stored and the Teflon-stored samples. The signal from the glass-stored sample was of significantly higher intensity than that from the Teflon-stored sample, although generally, the shapes of the curves are not dramatically different.

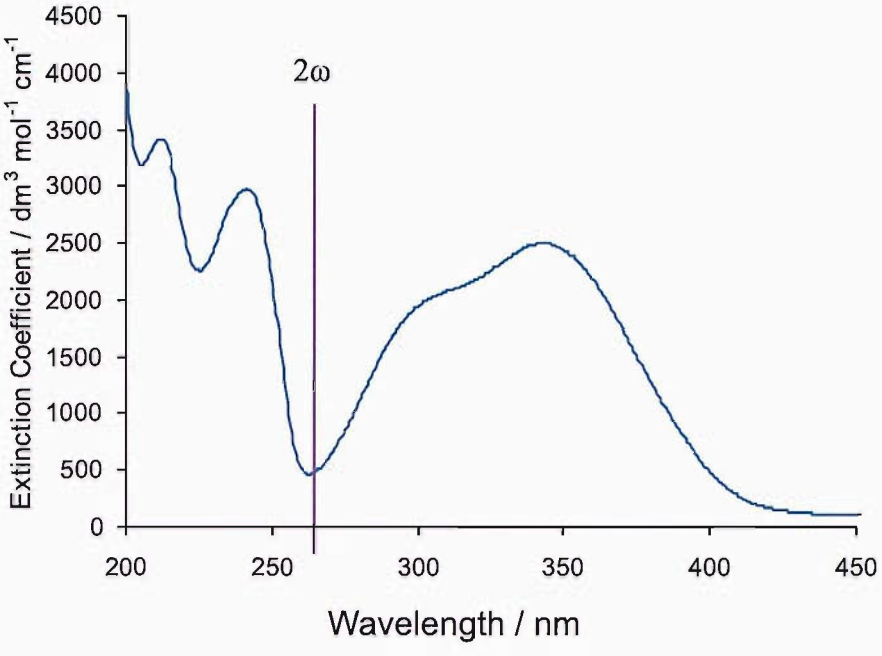

Figure 3.17: The UV-vis spectrum of a 0.17 mM 4-nitrobenzo-15-crown-5 aqueous solution: neither the second harmonic, or the fundamental, wavelength of the SHG experiment (266 nm) correspond to an absorption peak, and so the SHG signal is not expected to be resonantly enhanced.

This is illustrated later in the section. These two cases are discussed separately.

Significant Hyperpolarisability Components of 4-nitrobenzo-15-crown-5

Ab initio calculations on the significant hyperpolarisability components were obtained.[57] The analysis suggests that the significance of several components of $\beta^{(2)}$ are relatively high at 532 nm. The β_{zzz} component is the most significant, but there is almost certainly at least one other significant component. The calculation suggests that both the β_{zxx} and the β_{xzx} contributions could affect the second harmonic response. As a result, several different assumptions will be taken regarding $\beta^{(2)}$, and all will be reported here.

Glass Stored 4-Nitrobenzo-15-crown-5

The polarisation response of nitrocrown solutions was measured at several concentrations. There is a change in the B/A, C/A and χ component ratios with con-

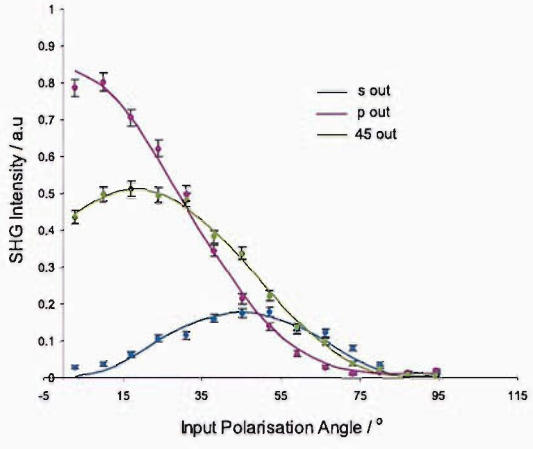

Figure 3.18: Polarisation response of glass stored 4-nitrobenzo-15-crown-5 at 0.52 mM concentration.

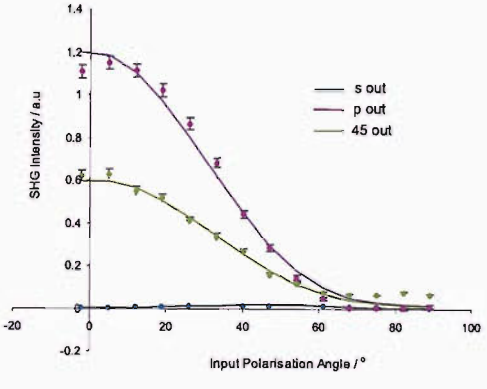

Figure 3.19: Polarisation response of glass stored 4-nitrobenzo-15-crown-5 at 1.5 mM concentration.

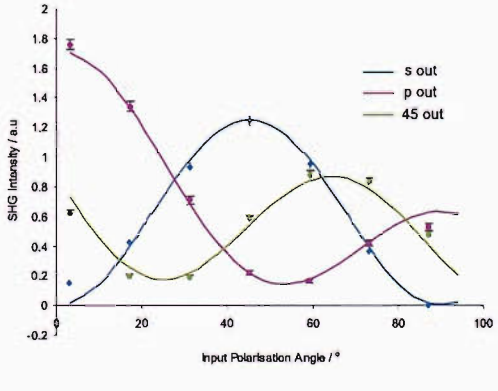

Figure 3.20: Polarisation response of glass stored 4-nitrobenzo-15-crown-5 at 5.1 mM concentration.

centration. The change in the response is seen in Figures 3.18 to 3.20. The results are given in Table 3.9.

Since there is some uncertainty as to the contributing hyperpolarisability components, the apparent tilt angle (θ_{app}, the angle between the experimental surface normal and the O_z axis as defined in Figure 3.14) is given for various β assumptions, which are denoted by superscripts:

a: assuming β_{zzz} and β_{zxx} to be dominant, and ψ to be 90^o

b: assuming β_{zzz} and β_{zxx} to be dominant, and ψ random

c: assuming β_{zzz} and β_{xzx} to be dominant, and ψ to be 90^o

d: assuming β_{zzz} and β_{xzx} to be dominant, and ψ random

Teflon Stored 4-nitrobenzo-15-crown-5

The same SHG experiments were carried out on a teflon stored sample. The results were slightly different, and are reported in Table 3.10. The general trends within the B/A, C/A and χ ratios are slightly different. These ratios for both the glass-stored and Teflon-stored samples are plotted in Figure 3.21, and the χ ratios are shown in Figure 3.22.

Conc/mM	χ_2/χ_1	χ_3/χ_1	B/A	C/A	θ^a_{app}/°	θ^b_{app}/°	θ^c_{app}/°	θ^d_{app}/°
0.52	0.125	0.373	0.117	0.461	70.7	42.3	15.6	-
1.0	0.004	0.081	0.0109	0.149	63.5	-	-	40.9
1.5	0.087	0.082	0.108	0.119	68.5	11.5	59.5	18.4
2.4	0.26	0.198	0.296	0.296	68.9	26.1	-	29.6
3.0	0.351	0.366	0.346	0.475	68.8	35.6	-	31.3
3.5	0.475	0.472	0.437	0.572	69.3	37.9	-	33.7
4.3	0.628	0.672	0.519	0.73	69.3	39.8	-	34.9
5.1	0.724	0.777	0.604	0.854	69.6	39.9	-	-
6.0	1.260	1.322	0.625	1.07	69.3	67.8	-	44.2
8.7	1.382	1.500	0.895	1.278	79.8	70.8	-	47.9

Table 3.9: Ratios and Parameters derived from the polarisation dependence of glass-stored 4-nitrobenzo-15-crown-5 over a range of concentrations

Conc/mM	χ_2/χ_1	χ_3/χ_1	B/A	C/A	θ^a_{app}/°	θ^b_{app}/°	θ^c_{app}/°	θ^d_{app}/°
3.0	0.291	0.300	0.358	0.480	74.1	27.2	9.0	45.4
3.1	0.388	0.396	0.444	0.596	71.7	41.1	10.7	39.7
4.0	1.155	1.238	0.698	0.945	74.8	64.9	5.4	23.5
4.6	1.450	1.585	0.743	1.069	73.6	66.2	4.6	19.0
6.0	1.396	1.507	0.779	1.106	78.2	67.7	2.9	19.5
7.0	1.611	1.668	0.829	1.129	82.3	-	3.6	9.6
10.0	1.12	1.155	0.894	1.221	67.1	71.3	4.0	20.9

Table 3.10: Ratios and Parameters derived from the polarisation dependence of teflon-stored 4-nitrobenzo-15-crown-5 at several concentrations with θ reported under various assumptions of significant β components. ψ is assumed random.

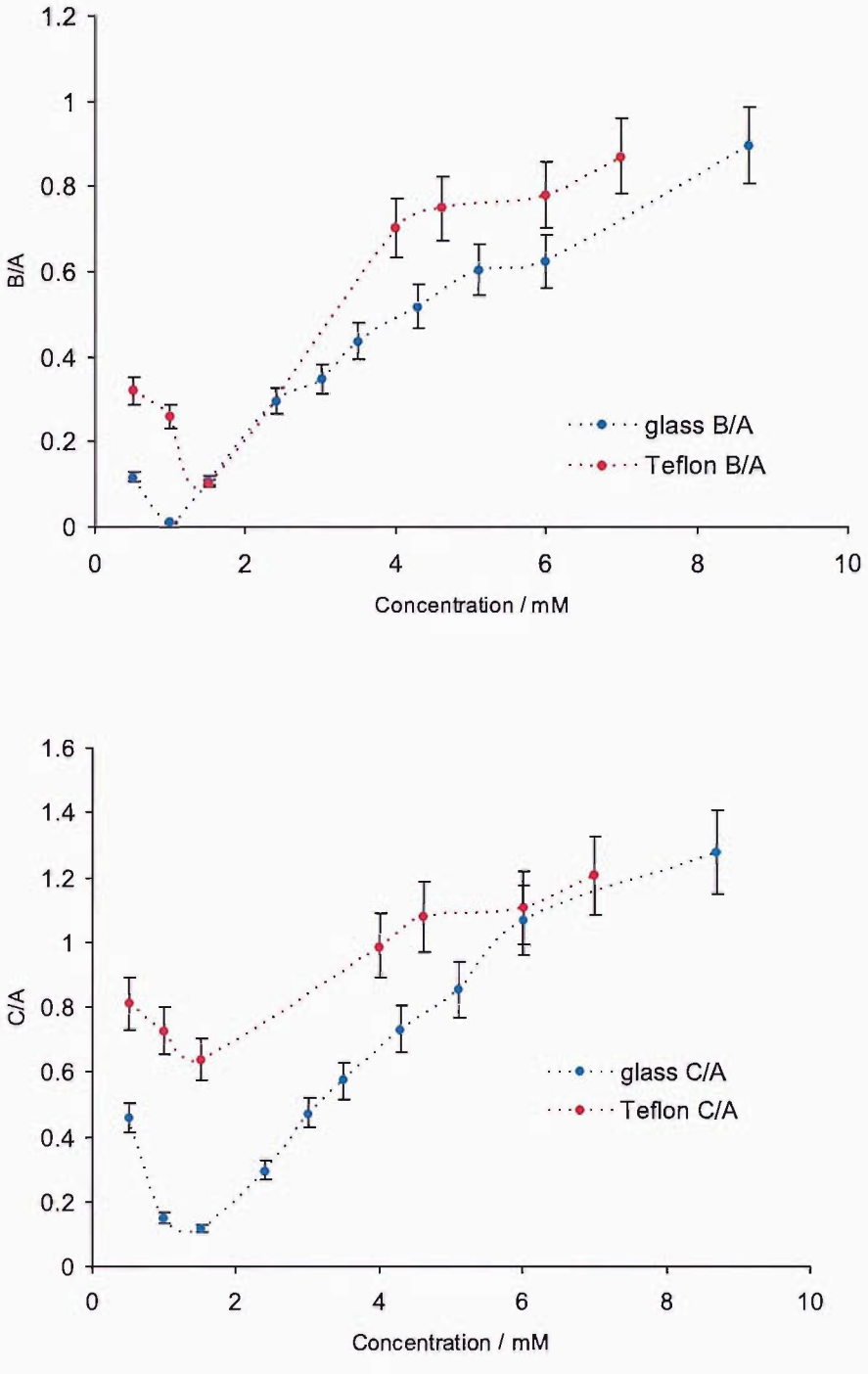

Figure 3.21: B/A and C/A ratios with bulk concentration for glass stored and teflon stored 4-nitrobenzo-15-crown-5 (error bars are 10%).

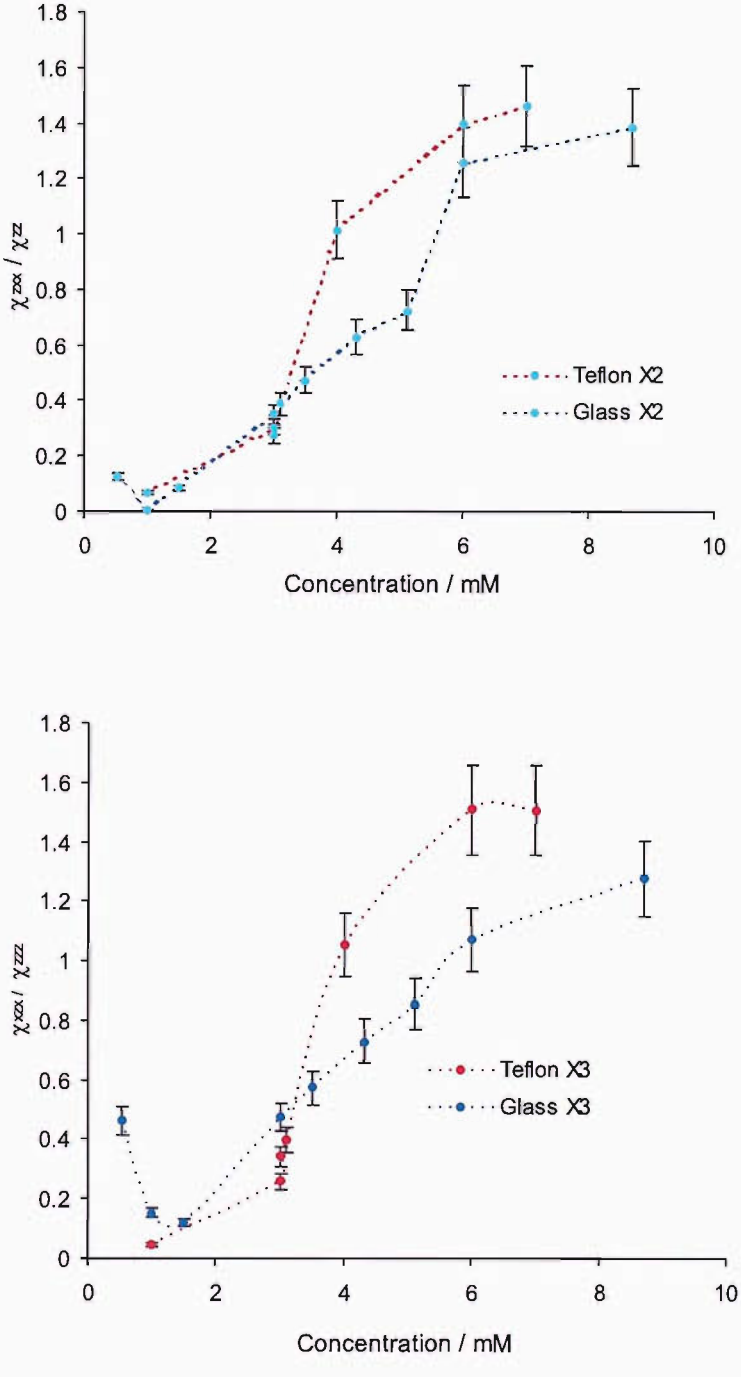

Figure 3.22: χ_{zxx}/χ_{zzz} and χ_{xzx}/χ_{zzz} ratios with bulk concentration for glass stored and teflon stored 4-nitrobenzo-15-crown-5 (error bars are 10%).

3.3.3 Glass Storage Effects

In order to clarify whether the differences between the Teflon and glass stored samples might be due to sodium ion leaching from the glass container, both the samples were run with an excess of sodium (NaCl). The results with and without sodium present for the glass stored sample are given in Figure 3.23, and those for the Teflon stored sample are given in Figure 3.24. In each case, the addition of excess sodium chloride resulted in a raised SHG intensity compared to that of the crown ether without salt added. Unfortunately, it is not possible to compare the intensities of the signals absolutely between the teflon stored samples and the glass stored samples, due to laser power fluctuations and alignment issues from day to day, although it has been observed throughout this project that in general the intensity of the glass-stored compound is consistently higher than that from the Teflon-stored sample. The addition of sodium chloride to the solutions results in a greater intensity increase for the Teflon-stored sample than it does for the glass-stored sample. Thus, it seems likely that sodium ion presence is indeed the source of any difference between samples cleaned in the same way but stored differently. Clearly, the glass stored sample is nowhere near saturated by sodium ions, as the increase in intensity on addition of salt is still pronounced.

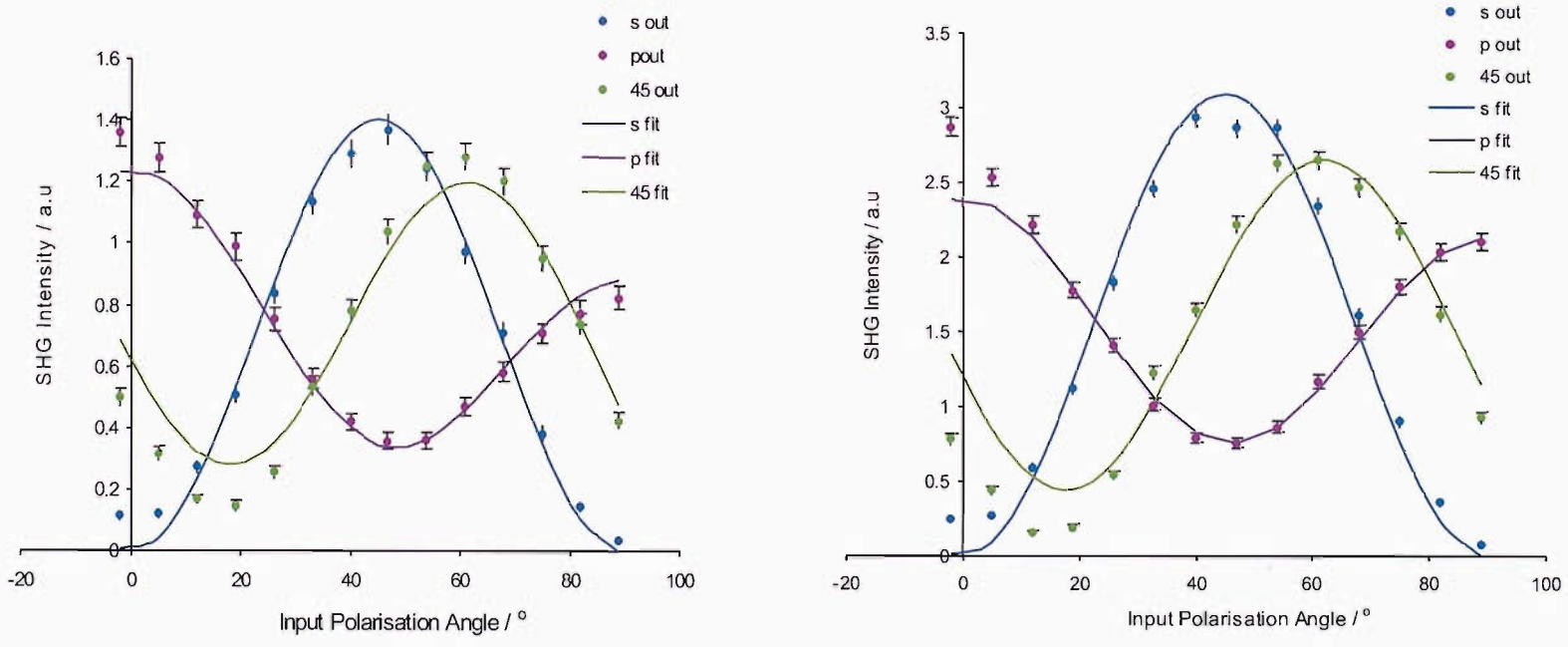

Figure 3.23: Polarisation response of glass stored 4-nitrobenzo-15-crown-5 at 6.0 mM concentration, and 6.0mM in the presence of excess NaCl.

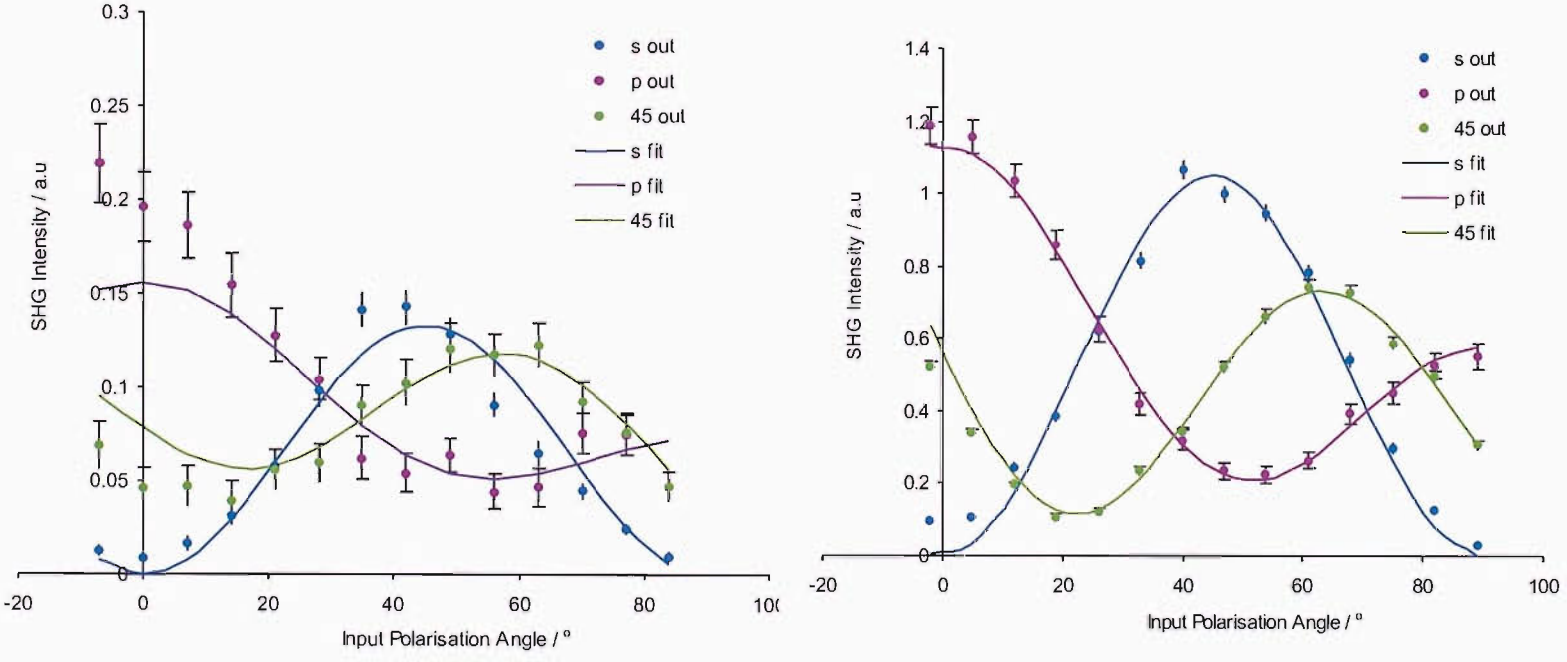

Figure 3.24: Polarisation response of Teflon stored 4-nitrobenzo-15-crown-5 at 6.0 mM concentration, and 6.0mM in the presence of excess NaCl.

Concentration Dependence

The concentration dependence of the 45-in, S-out signal was studied for the nitrocrown (Figure 3.25). There is clearly a phase difference between the nitrocrown and water signals, as is seen clearly in Figure 3.25 by the initial decrease in SH intensity with increasing concentration. Unlike the dependence of the signal obtained from benzo-15-crown-5, no plateau region was observed.

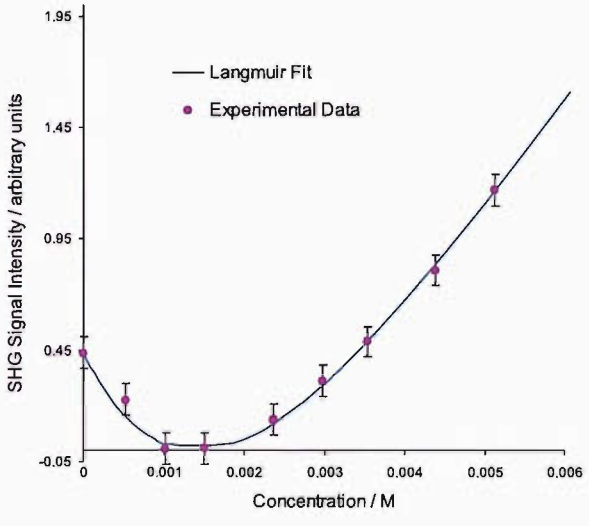

Figure 3.25: The adsorption isotherm of 4-nitrobenzo-15-crown-5 showing clearly the effect of the phase between the SH electric field of nitrocrown and water. The Langmuir fit assuming the phase to be 180^o is also shown.

The strongest solution made up was 15 mM, and this required a period of more than three hours in the sonic bath, with heating, to dissolve all of the solid. This maximum concentration is much higher than the point at which the plateau region became apparent for benzo-15-crown-5, and may indicate that the nitro compound forms multi-layers at the surface, which are still within the surface region affected by SHG. This would explain the lack of plateau in the SHG signal.

Several isotherms were recorded at different times, and the results are shown in Table 3.11.

Within errors, it appears that the Teflon stored and glass stored samples produce similar isotherms, with an adsorption free energy value of -22 kJ mol^{-1}.

	K/dm^3mol^{-1}	ΔG_{ads} / kJ mol^{-1}
Glass stored	118.4(10)	-21.6(1.4)
Teflon stored	232.4(15)	-22.2(1.1)

Table 3.11: Parameters of Langmuir isotherms, with an assumed phase of 180°.

3.3.4 Discussion

The surface tension isotherm of 4-nitrobenzo-15-crown-5 is quite similar in shape to that of the benzo-15-crown-5, suggesting a similar level of surface activity. The fact that several hyperpolarisability tensor components in the nitrocrown chromophore have a relatively high value raises issues regarding the best way to analyse the SHG results. A uniaxial approximation is certainly not sufficient for the system, but it may be that even the assumption of two dominant hyperpolarisability tensor components is not sufficient.

Another issue is raised by the difference between the glass stored and Teflon stored samples. Both of these are columned in exactly the same way, and yet the results are slightly different, illustrated by the B/A, C/A and χ ratios. The most likely explanation of this discrepancy is that the crown sample stored in glass has leached some sodium ions from the container. Unfortunately, this needs only occur on a very small scale to affect surface results since the sodium ions will enhance the surface activity of the crown. Addition of sodium chloride salt to the samples (both glass stored and Teflon stored) leads to an increase in second harmonic signal intensity, but this was more pronounced with the Teflon stored sample.

The SHG concentration dependence clearly showed that there was a phase difference in the SH electric field between the signal originating from the water from the nitrocrown. The data could be fitted well by a simple Langmuir isotherm once again, and from this, the phase difference was estimated to be about 180°. No plateau region indicative of a monolayer formation was found for this compound, and whether this was due to the physical concentration limitation (arising from the

very poor solubility of the compound in water) or whether the nitrocrown is more likely to form multi-layers which will still be within the interfacial layer, in that further layers will also contribute to the SHG signal, is unclear from this data. The isotherm data may be used in order to separate the contribution from the water from that of the crown ether.

Separation of Water and Adsorbate Signal

The water signal is relatively high in comparison to the nitro-crown signal, and from the Langmuir isotherm, it is also seen that there exists a phase of about 180° between the water signal and that of the crown ether. These contributions may be separated such that the crown only contribution may be analysed to give the susceptibility tensor components arising solely from the crown, χ^{cro}.

This is possible by using the relationships:

$$\chi^{eff}_{zzz} = \chi^{cro}_{zzz} + \chi^{wat}_{zzz} \tag{3.18}$$

$$\chi^{eff}_{zxx} = \chi^{cro}_{zxx} + \chi^{wat}_{zxx} \tag{3.19}$$

$$\chi^{eff}_{xzx} = \chi^{cro}_{xzx} + \chi^{wat}_{xzx} \tag{3.20}$$

Where χ^{eff} is the effective susceptibility tensor, that is, the susceptibility of the interface as a single entity. The polarisation combination used for the concentration dependence measurements on 4-nitrobenzo-15-crown-5 was (45-in, S-out). From Equation 2.49, the S-out polarisation dependence only depends on χ_{xzx}. The water polarisation data is known, and since this is a single component system, this can be used to extract the data arising from the crown ether, assuming that the water surface remains unchanged on addition of the adsorbate. The validity of this assumption will be addressed in Parts II and III of the thesis. Substituting for χ^{eff}_{xzx}, at this input polarisation of 45° gives:

$$I_s \propto |\chi_{xzx} sin2\gamma|^2 = |(\chi_{xzx}^{cro} + \chi_{xzx}^{wat})|^2 = |\chi_{xzx}^{cro}|^2 + 2\ cos\ \Phi\ |\chi_{xzx}^{wat}||\chi_{xzx}^{cro}| + |\chi_{xzx}^{wat}|^2 \quad (3.21)$$

Where Φ is the phase between the signals. It is possible to obtain χ_{xzx}^{cro} by solving this quadratic expression. Consequently, all other χ components may be obtained. The example of χ_{zzz}^{cro} is shown in Equation 3.22.

$$\frac{\chi_{zzz}^{eff}}{\chi_{xzx}^{eff}} = \frac{\chi_{zzz}^{cro} + \chi_{zzz}^{wat}}{\chi_{xzx}^{cro} + \chi_{xzx}^{wat}} \quad (3.22)$$

Within this equation, there is only one quantity which is not known, and that is the value of χ_{zzz}^{cro}. The remaining unknown component may be found in the same way. Once these χ components are known, D and θ may be derived for the crown contribution, under various assumptions of significant β components, and ψ values. The results found for one set of data is presented in Table 3.13, and can be compared to Table 3.10, for which the water contribution was not treated.

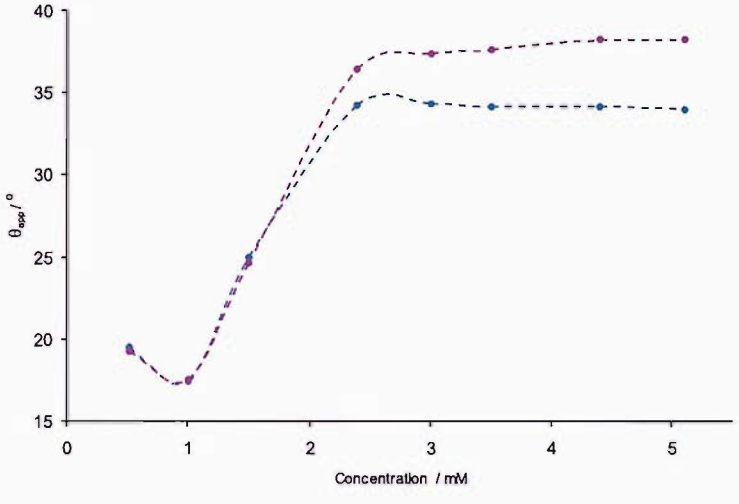

Figure 3.26: The apparent tilt angle, derived from the SHG polarisation dependence results, with the water contribution removed. Both datasets show the tilt angle calculated assuming β_{zzz} and β_{zxx} dominant. The blue data is under the assumption that ψ=90° and the pink is from the assumption that ψ is random. The dashed lines are just guides.

Once the water signal has been removed, the tilt angles derived (θ_{app}) are significantly changed. It appears that the most likely dominant $\beta^{(2)}$ components are

β_{zzz} and β_{zxx}, as these are the assumptions for which the change in θ_{app} is smooth over the concentration range. This assumption gives a high concentration tilt angle of about 34° for the assumption that ψ is 90°, and of about 38° when ψ is assumed random. The trend for θ_{app} is shown in Figure 3.26.

This may be a true tilt angle, and is quite different from that which was obtained without the extra treatment of the water signal. It may be, however, that the orientation of the surface molecules is weakly ordered. That is, it may be that the data is converging towards the weak limit. The width of the tilt angle distributions is something that will be examined in the molecular dynamics section.

Conc/mM	χ_2/χ_1	χ_3/χ_1	B/A	C/A	θ^a_{app}/°	θ^b_{app}/°	θ^c_{app}/°	θ^d_{app}/°
0.52	0.08	0.06	0.105	0.107	19.5	19.2	21.0	21.4
1.0	0.04	0.06	0.054	0.097	17.5	17.5	15.6	15.5
1.5	0.14	0.13	0.186	0.232	25.0	24.6	24.8	25.4
2.4	0.11	0.33	0.241	0.921	34.3	36.5	53.2	32.6
3.0	0.06	0.39	0.147	1.309	34.4	37.4	-	28.2
3.5	0.01	0.42	0.024	1.613	34.2	37.6	-	9.3
4.3	0.05	0.47	0.207	2.352	34.2	38.2	15.8	23.0
5.1	0.09	0.49	0.420	2.908	34.0	38.3	19.5	40.4

Table 3.12: Ratios and Parameters derived from the polarisation dependence of glass-stored 4-nitrobenzo-15-crown-5 once separated from the water contribution.

3.4 Summary of Experimental Results

Benzo-15-crown-5 and 4-nitrobenzo-15-crown-5 have been studied using surface tension measurements, second harmonic generation polarisation response and the concentration dependence of second harmonic generation. The results have been analysed and the information obtained has been discussed in terms of the possible structure of the interface.

The intensity of the signal obtained from the nitrocrown is in general somewhat larger than that of the benzocrown, which at first seems odd, as this is not a molecule which will be resonantly enhanced, but the intrinsic hyperpolarisability

is much higher, as calculated through the *ab initio* work.

The polarisation dependence of the benzocrown indicates no obvious change in orientation over the concentration range studied: there is no significant variation in any of the ratios derived at different concentrations. The orientational parameter, D for the benzo system within the concentration range consistently leads to an apparent tilt angle between 35^{o} and 43^{o} , which may indicate that the system is weakly ordered in terms of the model used to derive an average tilt angle for the system. Thus, it is desirable to further study the system with molecular dynamics.

The polarisation dependence of the nitrocrown shows some change with concentration. The B/A and C/A ratios, and the χ component ratios show first a decrease, below about 1.5 mM, and then an increase However, it is not clear that any change in the apparent tilt angle occurs. The derivation of θ_{app} is somewhat complicated by the uncertainty with this species as to which are the dominant hyperpolarisability tensor components, and so several assumptions are included in the reported results. Also, once the concentration dependence of the compound was fitted, it was possible to attempt to extract the pure crown contribution to the SH response. This relies upon the assumption that the SH response of the water is relatively unchanged with the addition of adsorbate. The derived tilt angle still showed a dependence on concentration once the contributions were separated, and rose to a maximum of either 34 or 38^{o}, depending upon the assumption on ψ. The concentration dependence of 4-nitrobenzo-15-crown-5 did not indicate any monolayer formation within the range studied, and this could be because a monolayer was not formed within the concentration range studied (that is, it could be due to the physical constraint of solubility in water) or it could be that the compound instead forms tight multilayers, which are within the region giving rise to the second harmonic response.

The next part of the thesis introduces the theory behind molecular modelling, and then the simulations run are presented in full.

Part II

Molecular Dynamics Simulations

Chapter 4

Simulation Methodology

The general theory and methods behind molecular dynamics simulation are presented in this chapter with emphasis on the techniques and algorithms utilised within this project.

4.1 Molecular Mechanics Methods

Molecular mechanics (MM) methods use a force-field approach to modelling: that is, they ignore electron motions and use only the nuclear positions to calculate the energy of the system. MM is used for systems containing a large number of atoms, and can provide information about structure and energetics, for example, on a timescale inaccessible to established quantum mechanical methods, that is approaching the accuracy of very high-level QM calculations, although it cannot provide detail about properties dependent on electronic distribution.

MM may be applied successfully as a result of the Born-Oppenheimer approximation, which allows the decoupling of electronic and nuclear motion, and thereby enables the energy of the system to be expressed purely based upon nuclear position.

Molecular mechanics is based upon a relatively simple view of the interactions within a chemical system being formed by contributions from such events

as bond stretching, angle opening and closing, and bond rotations. The models of these events begin with simple relationships such as Hooke's law. Without further modification, this model works well in some cases. Non-bonded interactions (electrostatic and van der Waals) are also considered.

A good MM force field will be transferable over a wide range of similar systems, over and above those for which the force-field was parameterised.

4.1.1 The AMBER Force Field

There are many available force fields which have been parameterised in slightly different ways, such as CHARMM,[59] AMBER[60,61] and OPLS.[62] The force field chosen in this work was the AMBER force field which is widely used in simulations on many types of system.

The general functional form of the AMBER force field is:

$$E_{ff} = \sum_{bonds} E_{ij}^{stretch} + \sum_{angles} E_{ijk}^{bend} + \sum_{dihedrals} E_{ijkl}^{torsion} + \sum_{pairs} E_{j}^{coul} + \sum_{pairs} E_{j}^{vdW} \quad (4.1)$$

E_{ff} is the potential energy of the system. The individual terms are expressed in Equations 4.2 to 4.6.

Bond stretching and bond bending are described by simple harmonic terms:

$$E_{ij}^{stretch} = \frac{1}{2} k_{ij}^{stretch} \left(r_{ij} - r_{ij0}\right)^2 \quad (4.2)$$

$k_{ij}^{stretch}$ is the force constant for the bond between atoms i and j, r_{ij} is the bond length, and r_{ij0} is the reference bond length.

$$E_{ijk}^{bend} = \frac{1}{2} k_{ijk}^{bend} \left(\theta_{ijk} - \theta_{ijk0}\right)^2 \quad (4.3)$$

k_{ijk}^{bend} is the force constant for the bond angle between atoms i, j and k, θ_{ijk} is the bond angle, and θ_{ijk0} is the reference bond angle.

$$E_{ijkl}^{torsion} = \sum_n \frac{1}{2} V_{ijkln}^{torsion} (1 + cos(n\phi + \delta_n)) \tag{4.4}$$

In this case, V_{ijkln} is the nth order force constant for the dihedral between atoms i, j, k and l. ϕ_{ijkl} is the dihedral angle and δ_n is the phase angle.

The non-bonded interactions (between atoms separated by at least three bonds) are broken down into electrostatic interactions, which are modelled by a Coulomb potential (Equation 4.5) and van der Waals interactions, which are modelled by a Lennard-Jones potential (Equation 4.6).

.

$$E_{ij}^{coul} = \frac{1}{4\pi\varepsilon_o} \frac{q_i q_j}{r_{ij}} \tag{4.5}$$

Here, q_i and q_j are the atomic charges and r_{ij} is the interatomic distance.

The Coulomb potential decays at a very slow rate of $\frac{1}{r}$. This means that the electrostatic forces will affect the system over a long range, and to simulate this type of force explicitly is extremely computationally expensive. The length over which these forces are significant means that the use of a short-range cutoff is a significant approximation, and can affect calculated quantities dramatically. Much work has been done with a view to improving the long-range force treatment, and methods have been developed to deal with long range terms which demand less computation than their total calculation, such as the particle mesh Ewald[63] used in the bulk of this work.

The Lennard-Jones model for van der Waals interactions, is:

$$E_{ij}^{vdW} = 4\varepsilon_{ij} \left[\left(\frac{\sigma_{ij}}{r_{ij}} \right)^{12} - \left(\frac{\sigma_{ij}}{r_{ij}} \right)^{6} \right] \tag{4.6}$$

Where ε_{ij} is the potential well depth for i and j and σ_{ij} is the distance at which E_{ij}^{vdW}=0.

Lennard-Jones interactions are not included for 1-2 and 1-3 bonded atoms (i.e those which are separated by 1 or 2 bonds respectively), and are scaled down between 1-4 bonded atoms. The interaction is a function which decays much more rapidly than the coulombic function describing the electrostatics, and so may be treated by the use of a cutoff without introducing significant errors.[64] When a simple truncation cutoff function is applied, the function becomes discontinuous at the cutoff point, and so usually a switching or shifting potential is used.

In order to define fully the force field, the various parameters present in the functional form must be specified. These are generally optimised to best reproduce the experimental properties that the user of that force field desires to simulate. Thus, force fields may have very different parameters, even if they have the same basic functional form. Other experimental properties may still be estimated using these force fields, but their original purpose, and any approximations introduced, should be considered.

4.1.2 Molecular Dynamics

Molecular dynamics is the solution of the classical equations of motion with time. The trajectory of the system is generated, through successive integration of Newton's laws of motion, embodied in Equation 4.7. This trajectory shows the evolution of the velocities and positions of the system's particles with time.

$$\frac{d^2x_i}{dt^2} = \frac{F_{x_i}}{m_i} \tag{4.7}$$

Equation 4.7 describes the motion of a particle i of mass m_i in one direction, x, and F_{x_i} represents the force acting on the particle in that direction.

Once we begin to deal with a force acting on particle i which is dependent on

the position of i relative to other particles, the calculation of the trajectory becomes very difficult, and in most cases, impossible, to deal with analytically. For this reason, finite difference methods are used.

Finite Difference Methods

To solve Newton's laws of motions numerically, the integration is broken down into small periods of time, of length δt, within which the force is assumed to be constant. Thus, the accelerations of the particles may be combined with the velocities and positions at time t to calulate the positions and velocities at time $(t+\delta t)$. Such methods are called finite difference methods, and these assume that the positions, velocities and accelerations of particles may be approximated as Taylor series expansions.

There are several ways in which finite difference properties are calculated in molecular dynamics. One family of integrators may be derived from the Verlet algorithm,[65] which used the expansions shown in Equations 4.8 and 4.9.

$$\mathbf{r}(t+\delta t) = \mathbf{r}(t) + \delta t \mathbf{v}(t) + \frac{1}{2}\delta t^2 \mathbf{a}(t) + \ldots \tag{4.8}$$

$$\mathbf{r}(t-\delta t) = \mathbf{r}(t) - \delta t \mathbf{v}(t) + \frac{1}{2}\delta t^2 \mathbf{a}(t) - \ldots \tag{4.9}$$

Where $\mathbf{r}(\mathbf{t})$ is the position of a particle at time t, $\mathbf{v}(\mathbf{t})$ the velocity, and $\mathbf{a}(\mathbf{t})$ the acceleration. Addition of Equations 4.8 and 4.9 gives Equation 4.10.

$$\mathbf{r}(t+\delta t) = 2\mathbf{r}(t) - \mathbf{r}(t-\delta t) + \delta t^2 \mathbf{a}(t) + \ldots \tag{4.10}$$

Although the velocities do not appear explicitly, there are ways in which they may be calculated from the algorithm, through either Equation 4.11 at timestep t or Equation 4.12 at timestep $t + \frac{1}{2}\delta t$. However, this does lead to some issues: for example, the velocity at timestep t cannot be calculated until the position at timestep $t + \delta t$ is known.

$$\mathbf{v}(t) = \frac{\mathbf{r}(t+\delta t) - \mathbf{r}(t-\delta t)}{2\delta t} \tag{4.11}$$

$$\mathbf{v}\left(t + \frac{1}{2}\delta t\right) = \frac{\mathbf{r}(t+\delta t) - \mathbf{r}(t)}{\delta t} \tag{4.12}$$

The velocity-Verlet[66] algorithm which is employed in this work is based upon the Verlet algorithm, but explicitly gives positions, velocities and accelerations at the same time:

$$\mathbf{r}(t+\delta t) = \mathbf{r}(t) + \delta t\mathbf{v}(t) + \frac{1}{2}\delta t^2\mathbf{a}(t) \tag{4.13}$$

$$\mathbf{v}(t+\frac{1}{2}\delta t) = \mathbf{v}(t) + \frac{1}{2}\delta t\mathbf{a}(t) \tag{4.14}$$

$$\mathbf{v}(t+\delta t) = \mathbf{v}\left(t + \frac{1}{2}\delta t\right) + \frac{1}{2}\delta t\mathbf{a}(t+\delta t) \tag{4.15}$$

$$\mathbf{v}(t+\delta t) = \mathbf{v}(t) + \frac{1}{2}\delta t[\mathbf{a}(t) + \mathbf{a}(t+\delta t)] \tag{4.16}$$

The important considerations in these integration methods are that they should conserve energy and momentum, be time-reversible and allow as long a timestep, δt, as possible to be used. The fewer the timesteps required to simulate a system over a given amount of "real" time, the more computationally efficient the simulation. The length of timestep is limited by the requirement to accurately model the fastest motions in the system avoiding atom overlaps and excess bond extensions. The method should also reproduce, within reason, the exact, analytical solution of the equations.

The choice of timestep must strike a balance between accuracy and computational cost. This is usually judged by the energy fluctuation observed in a 'constant energy' simulation over a reasonable period of time. If the energy fluctuation is very low, then a longer timestep may be used to decrease the computational expense of the simulations. However, a timestep which is too large will result in a simulation which does not properly conserve energy. A timestep between 1 and 2.5 fs is commonly seen in MD simulations of interfacial systems.[38,67,68] Another consideration is energy drift.

4.2 Periodic Boundary Conditions

It is not computationally efficient to set up a huge system and run a simulation. Instead, it is common practice to use periodic boundary conditions, where a small simulation cell is used, and replicated in two or three dimensions to surround the original cell. Within this periodic array, a molecule which leaves the (original) simulation cell will appear on the other side of the cell, rather than entering a vacuum region, as would happen without the image cells. To calculate forces (except Coulomb interactions), the interaction of an atom is only allowed with the closest image of each other atom (the minimum image convention).

For the electrostatic forces, decaying only with $\frac{1}{r}$, the interaction of molecules with all of their periodic images must be included. Full electrostatics evaluation would be extremely expensive, but methods have been developed which approxi-

mate this treatment efficiently, such as the particle Mesh Ewald (PME)[63] sum, as used in this work.

4.3 Temperature and Pressure Control

Molecular dynamics are performed under various ensembles, that is, with various conditions specified as constant. Two such ensembles are NPT (N indicates constant number of particles, P indicates constant pressure and T, constant temperature) and NVT (V indicates constant volume). Maintenance of conditions of constant temperature and/or pressure may be carried out in various ways.

The temperature of a system is related directly to its kinetic energy, E_K, by Equation 4.17.

$$\langle E_K \rangle_{NVT} = \frac{3}{2} N k_B T \tag{4.17}$$

Where N is the number of atoms, k_B is the Boltzmann constant, and T is the temperature.

It is possible to control the temperature of the system by rescaling the velocities, since the current temperature of the simulation may be calculated and the required temperature attained by a rescaling factor based upon the actual and desired temperatures.[69]

Alternatively, the system may be coupled to an external heat bath, a method developed by Berendsen *et al.*,[70] and that bath will supply or remove thermal energy from the system as required. This approach has the advantage that it does allow the temperature to fluctuate about the desired temperature.

However, neither of these methods generate a rigorous canonical ensemble. For example, velocity scaling, as implemented in both methods, artificially allows temperature differences among system components to remain, which may lead to

phenomena such as a solute being cold and a solvent being hot, because the overall average temperature of the system is correct.

There are methods which do result in a rigorous ensemble, for example, Stochastic collisions methods. The Langevin equation[71] introduces a collision-simulating term into the integrator as shown in Equation 4.18.

$$m\mathbf{a}_i(t) = \mathbf{F}_i(t) - \gamma_i m_i v_i(t) + \mathbf{R}_i(t) \tag{4.18}$$

where γ_i is a friction coefficient, and $\mathbf{R}_i$ is a stochastic (random) force. The stochastic force is influenced by thermal noise: it is linked to a temperature bath and will increase or decrease according to whether the system temperature is too hot or too cold. A Langevin thermostat is used in this work.

The pressure may be controlled by methods analogous to those for temperature control, such as volume scaling (isotropic or anisotropic), or coupling to an extended system.

Summary

The theory of molecular dynamics methods has been introduced, along with the methods employed in this work. The use of force fields has been considered, along with the calculation of both trajectories and properties of the system.

The reasons for the choice of timestep have been addressed as needing to balance computational efficiency and energy stability. The velocity-Verlet integrator, as used in this work, has been discussed.

Chapter 5

Computational Results

5.1 The Water/Air Interface

5.1.1 Modelling Water

Owing to its importance in so many systems, a huge amount of work has gone into the parameterisation of water force fields.[64,72,73] No single water model can, as yet, accurately reproduce all experimental properties, and therefore many different models are in use. Different water models are optimised for the most accurate representation of certain properties. The choice of water model for a particular simulation must be made with careful consideration of the properties which are most important to the type of simulation that is being carried out.

The types of water model which have been developed are broadly encompassed within four categories: rigid, flexible, polarisable and *ab intio*. The latter is noted for completion only: for studies such as this one, using large amounts of solvent, such a water potential would be incredibly computationally expensive.

Some of the most frequently used water models are based on classical effective pairwise potentials to treat water-water, water-solute and water-boundary interactions, with no explicit three-body terms or polarisation effects, although these may be accounted for to some extent through the value of the dipole moment. These "simple" water models use between 3 and 5 interaction sites and a rigid wa-

ter geometry. The advantage of such models lies in the computational efficiency with which the energies may be calculated, which is very important when simulating systems with large amounts of solvent present. These models have been criticised[74] as being a type of model which is unable to account for the directional properties of hydrogen bonding, a phenomena known to be of great importance in water. However, the models remain popular, and the literature indicates that a great deal of experimental observation may be reproduced and further understood using these models.

The rigid models include the 3 site SPC,[75] TIP3P,[76] SPC/E[77] models, the 4 site TIP4P,[76] and the 5 site ST2[78] and TIP5P[79] models. These have been extensively studied under different conditions[80,81] and for the calculation of various different properties,[72] and have been successfully used well outside their original parameterisation conditions.

Generally, the rigid models predict some properties of water reasonably well, including the density, which is particularly well reproduced by SPC/E and the 3, 4 and 5 site TIP potentials, and the enthalpy of vaporisation, but vary significantly in their prediction of other properties, such as the dielectric constant of water. To some extent, the radial distribution function of water is also better for some models. TIP5P reproduces the experimental distribution accurately, and TIP4P and SPC/E reproduce it very well, but TIP3P and SPC deviate slightly more.[82] The radial distribution of both SPC/E and TIP3P are reported in this section (Figure 5.1), and SPC/E does more faithfully reproduce the experimental distribution. The self-diffusion coefficient is another important property, but not one for which the models tend to be specifically parameterised. However, SPC/E, ST2 and TIP5P reproduce the experimental value well, while it is overestimated by TIP3P and TIP4P.

Clearly the rigidity of such water models means that certain properties cannot be calculated from them, such as vibrational spectra. There are models which have been developed for such simulations, such as the flexible SPC derivative,[83] which

was used by Morita and Hynes to run simulations which could then be compared to SFG spectra on water.[84] For this work, such detail is not necessary, as no vibrational data will be extracted.

The SPCP,[85] CKL[86] and PTIP4P[87] are all models in which a point polarisability is assigned to the oxygen atom. More recent parameterisations introduce a fluctuating charge on the sites of the molecule, which lead to the improved SPC/FQ and TIP4P/FQ potentials.[88]

However, the introduction of a flexible geometry and/or polarisability into a water molecule increases the computational expense compared to rigid, non-polarisable models. A considerable length of time is required for convergence of properties at low temperatures, and there are many questions about how best to parameterise such models. In fact, in a study comparing an *ab initio* approach to classical models, both rigid and polarisable, the conclusion was that in fact there is no real benefit in going beyond the simple rigid models such as SPC/E, TIP3P and ST2 for simulations of water under ambient conditions, even in the presence of charged species.[89] It is only when quantitative comparison is wanted a long way from ambient conditions that a polarisable potential is needed to improve comparison to experiment.

In this project a large amount of water will be simulated, and computational efficiency is therefore important. The TIP3P and SPC/E models are considered, both of which use three-sites to model the electrostatic interactions. The van der Waals interaction between two water molecules is computed using a Lennard-Jones function with just one interaction point per molecule centred on the oxygen atom.

The difference between the TIP3P and SPC/E models lies in the geometry of the water molecules, the partial charges assigned to the atoms and the Lennard-Jones parameters. These are presented in Appendix D for completeness.

Previous Work on the Water/Air Interface

Since the advent of computer simulation, many studies have been carried out on the water/air interface due to its fundamental importance. Early simulations produced surface tension results in very poor agreement with experiment, although trends in surface tension could be replicated.[90] A large amount of research has been carried out since this early work, and greatly improved comparisons have been achieved.

Perhaps the most successful simulations of interfacial water properties have been carried out by Alejandre *et al.*[67] and extended by Sokhan and Tildesley[38] using the SPC/E water model. The agreement found between simulation and experiment is extremely good for the surface tension, with a value of 66 ± 3 mN m^{-1} at 328 K compared to the experimentally determined 67 mN m^{-1}. The authors also report surface tension as a function of temperature, and find good agreement with experiment.

The only properties which do not reproduce experiment quite as well are the densities of the SPC/E water at high temperatures, but this is understandable since the SPC/E force field model is designed to reproduce water properties at 300 K. Sokhan and Tildesley report non-linear optical comparisons on the same water/vapour system and compare these to SHG data. The results offer some explanation of an apparent discrepancy between reported results from SHG and SFG spectroscopy, suggesting that they are in fact sensitive to different parts of the interface, where the simulations indicate that there are two distinct regions of water orientation.

Taylor *et al.*[91] carried out a similar study almost in parallel to that of Alejandre *et al.* The same water potential was used, and the same simulation methodology. The difference in the calculation of the surface tension was that a long-range cut-off was used, rather than the full electrostatic treatment which was applied by Alejandre. This provides a valuable comparison between different treatments of long range forces. The study provides some information on orientational properties of water at the water/vapour interface. The surface tension of the water/vapour

system at 298 K is calculated as 66±2 mN m^{-1}. This is not as close to the experimental value (which is 72.4 mN m^{-1} at 298 K) as Alejandre *et al.* achieved, and this is almost certainly due to the use of the cutoff treatment of the long range contribution. Nevertheless, this surface tension is very reasonable in comparison to that derived for other water models with either full electrostatic or truncation treatment of the long range contributions.

A study by Feller *et al.*[92] clearly illustrates the effect that truncation of long range forces has on surface tension calculations. They report a surface tension on a TIP3P water/vapour interface as a function of long-range force treatment. Using the Ewald sum, they acheive a surface tension of 52.7±1.5 mN m^{-1} at 293 K, which is significantly lower than the experimental value, 72.8 mN m^{-1}, at that temperature. With a cutoff (using potential shifting) of 12 Å, this value rose to 70.2±1.7 mN m^{-1}. This is thought to be due to induced long-range ordering. If this cutoff is increased to 18 Å, then the calculated surface tension is 54.6±1.6 mN m^{-1}, which is much closer to that predicted using Ewald treatment, but still some long-range ordering is apparent in the system. With a force field switching function from 10 to 12 Å the value drops to 43.8±2.1 mN m^{-1}.

Summary

The SPC/E model appears to be the best model to represent the experimental water/vapour interface, as illustrated by the comparisons to experiment by Tildesley *et al.* and Taylor *et al.*, and this is the model chosen for this work, although some preliminary simulations are carried out using TIP3P for comparison. For surface properties, one major consideration has to be the treatment of the long-range interactions, as this strongly affects the value of surface tension obtained.

5.1.2 Bulk Water Equilibration

The water slabs used in this study were created from equilibrated water boxes to ensure a suitable density was obtained. Six box sizes were originally used, and

each box was simulated using both SPC/E and TIP3P models. The box sizes and number of water molecules are listed for each box. All simulations were carried out using the NAMD package.[93] NAMD was developed by the Theoretical and Computational Biophysics Group in the Beckman Institute for Advanced Science and Technology at the University of Illinois at Urbana-Champaign.

Box 1: containing 265 water molecules, and with x, y and z dimensions (L_x, L_y and L_z) of 20 Å.

Box 2: containing 1345 water molecules, $L_x = L_y = 45$ Å, $L_z = 20$ Å.

Box 3: containing 3064 water molecules, $L_x = L_y = L_z = 45$ Å.

Box 4: containing 12916 water molecules, $L_x = L_y = 80$ Å, $L_z = 60$ Å.

Box 5: containing 17267 water molecules, $L_x = L_y = L_z = 80$ Å.

Box 6: containing 21581 water molecules, $L_x = L_y = 80$ Å, $L_z = 100$ Å.

The water boxes were first minimised, and then heated gradually to 298 K, using a timestep of 2 fs (20 ps at 100 K, 20 ps steps at 200 K and 40 ps at 298 K). After this, five 0.1 ns blocks were run under NPT conditions, with the Langevin thermostat damping set to 10 ps^{-1}. For 100 ps the Nosé-Hoover piston barostat with a pressure target of 1 atm, a piston temperature of 298 K, a damping parameter of 200 fs and an oscillation period of 400 fs were used. A further 400 ps was run with the barostat piston damping parameter at 400 fs, and the piston decay at 300 fs. The SHAKE algorithm was applied to all bonds throughout the simulations. An example NAMD input file is given in Appendix E for the bulk water production simulation. The radial distribution function (oxygen to oxygen) is shown for Box 5 of the TIP3P and SPC/E systems, calculated over the last 0.1 ns of the equilbration phase (Figure 5.1). The SPC/E data shows much more prominent second and third shells than are seen from the TIP3P data, as was noted in the literature.[82]

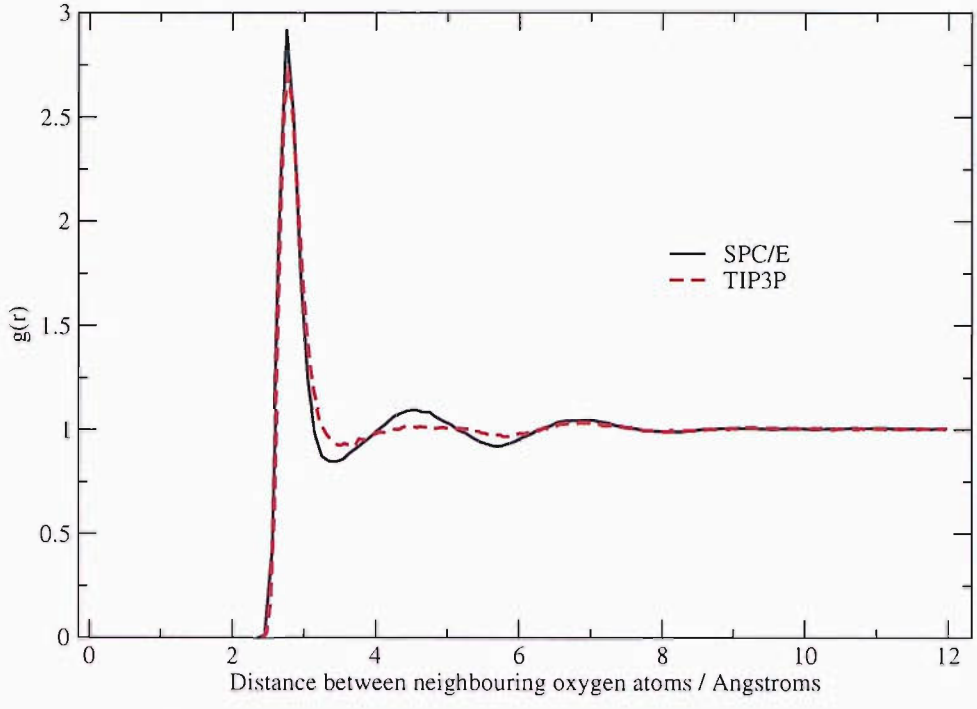

Figure 5.1: Radial distribution (oxygen to oxygen) for Box 5 (80 Å by 80 Å by 80 Å) for both the TIP3P and SPC/E simulations.

The density of each box size, for each model, is presented in Table 5.1. Again, the SPC/E model shows better agreement with the experimental density of water.

Label	Box size(N)	TIP3P ρ / g cm^{-3}	SPC/E ρ / g cm^{-3}
Box 1	265	0.9519	1.0010
Box 2	1345	0.9789	0.9990
Box 3	3064	0.9833	0.9934
Box 4	12916	0.9819	0.9937
Box 5	17267	0.9790	0.9813
Box 6	21581	0.9773	0.9822

Table 5.1: Densities for each box size for TIP3P and SPC/E equilibrated water boxes

The water boxes were well-equilibrated after this period, giving good radial distribution functions and densities. The boxes were then used to create the water slabs to be used in the interfacial simulations.

5.1.3 Slab Equilibration

The equilibrated water boxes were set up as slabs by the extension of their z-axis in both directions, following the method of Alejandre *et al.*[67] Thus, a simulation cell contains, effectively, two water/air interfaces. The gap above and below the water slab was twice the width of the slab. Slabs 1 to 6 were created from Boxes 1 to 6, and were run at 298 K. Slabs 1 and 3 were also run at increased temperatures of 316 K, 328 K, 367 K and 411 K to give a comparison to the surface tension data of Alejandre *et al.* This is reported a little later in the section.

The slabs were equilibrated over 0.5 ns of NVT ensemble simulation. An example input file for Slab 4 is given in Appendix E. The density profile of the slabs, normalised to the density of Box 4, was monitored to check their stability: that is, to ensure that the slab is remaining intact, and maintaining the correct density. At this stage, the centre of mass of the smallest system, Slab 1, of depth 20 Å, shows a large drift in the z-direction, shown in Figure 5.2. The z-axis of the simulation cell for this system was increased so that there were 130 Å of vapour above and below the central slab. This was to determine whether it was the proximity of the interfaces that was destabilising the system. From Figure 5.2 it is seen that the drift is still significant.

Slab 2, being of the same depth, showed similar drifting, although the drift was somewhat lessened in comparison to Slab 1. Slabs 3 to 6 showed no such drift. The density profiles of Slab 3 are shown in Figure 5.3. It is likely that the drift of Slab 1 occurred due to the very small number of water molecules present.

For further simulations, involving crown ether molecules at the interface, Slabs 3 and 4 were initially used. These represent systems which are stable, without being as computationally expensive as the larger Slabs 5 and 6.

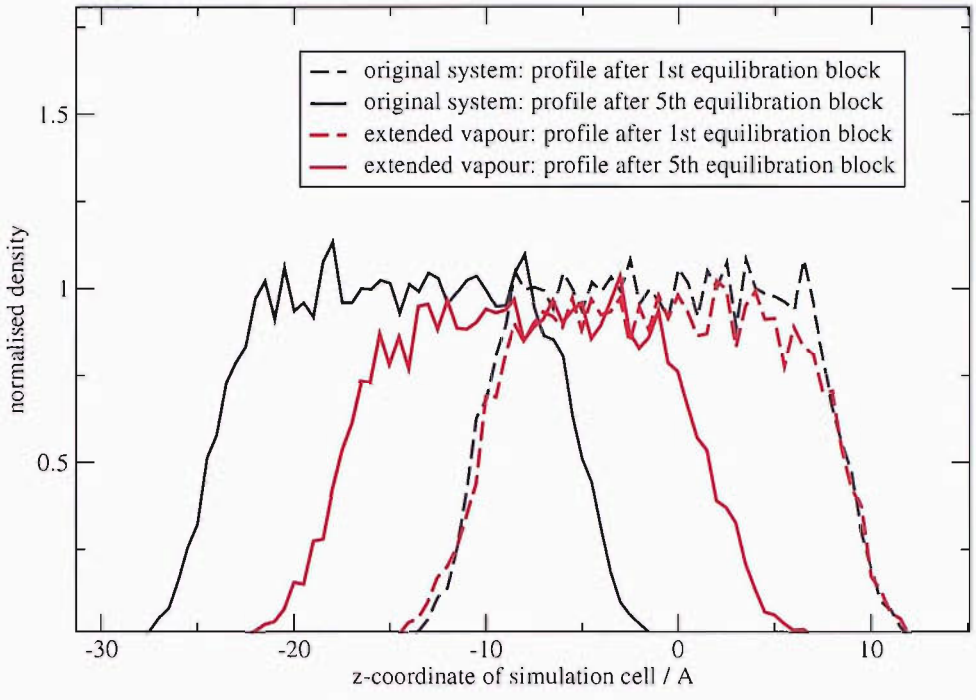

Figure 5.2: The density profiles at the start and finish of the equilibration period for Slab 1 with a 40 Å vapour regions above and below the water slab, and with 130 Å vapour regions. It is clear that although the drift is reduced with a larger vapour region, the movement is still significant.

Gibbs' Dividing Surface

The density profiles of the water slabs may be fitted, using a hyperbolic function[90,94] (Equation 5.1). This allows the z position of the Gibbs' dividing surface, as introduced in Section 2.1, to be calculated, which geometrically defines the interface of the system.

$$z = \frac{1}{2}(\rho_L + \rho_V) - \frac{1}{2}(\rho_L - \rho_V)\,tanh\left[\frac{z - z_o}{d}\right] \tag{5.1}$$

Where $d = \frac{t}{2.1972}$ and t is the 10-90% thickness of the interface, ρ_L is the density of the liquid, and ρ_V the density of the vapour.

Surface Tension of Water

The expression:

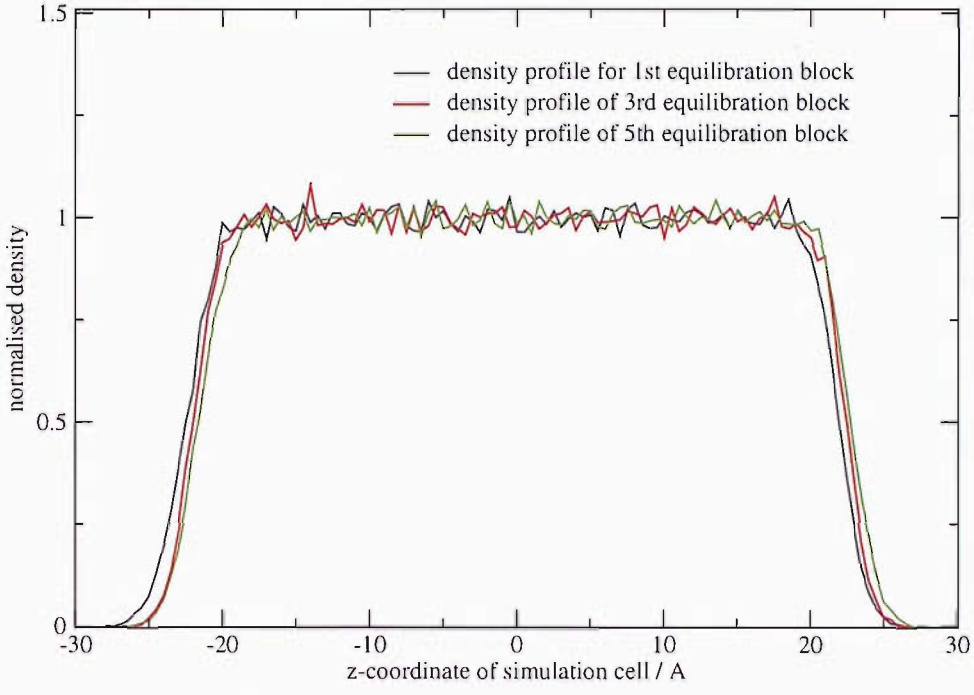

Figure 5.3: The density profiles at different stages of equilibration of Slab 3 (45 Å by 45 Å by 45 Å) with 90 Å vapour above and below the water.

$$\gamma = \frac{1}{2}\langle P_{zz} - \frac{1}{2}(P_{xx} + P_{yy})\rangle \tag{5.2}$$

is applied to the pressure tensor components to derive the pressure profile of the system. This is a general surface tension expression with an additional factor of $\frac{1}{2}$ included which takes into account the two interfaces present in the simulation cell. Pressure profiling is implemented within the NAMD package, and the calculation of the overall pressure profile is done using the method presented by Lindahl and Edholm:[95] in this method, the system is decomposed into individual thin slabs and pairwise contributions over each local slab are considered. This method presents a reasonable balance between the computational expense that a full calculation would involve, and the large number of values required to get a good estimate of the surface tension. The pressure profile in the simulations was calculated every 5 timesteps (10 fs).

Pressure profiling is incredibly sensitive to the treatment of the long-range part of the calculation. Several methods of surface tension calculation have been reported, and it is well-known that without full treatment of electrostatic interac-

tions, this calculation is dramatically affected.[67,91,92,95] It is not possible to use the full electrostatic treatment for pressure profile calculation within NAMD, and so a long range cutoff is used. However, this is a large cutoff and, as was illustrated by Feller,[92] this should minimise the effects on the pressure profile calculation.

Big fluctuations in the long-range parts of the pressure profile calculation mean that it is necessary to average over a greater period of time than is usually required to calculate most thermodynamic properties.

For any property calculated using truncation of the long-range van der Waals forces, it is useful to calculate the contribution to the property from those particles for whom $r > r_c$,[96] where r_c is the cutoff radius. This may be done by assuming that the radial distribution, g(r), at these distances, is approximately unity. For the calculation of surface tension, this correction is significant, and should be included. This long range correction, γ_{LRC}, may be expressed as:[97]

$$\gamma_{LRC} = 12\pi\varepsilon\sigma^6(\rho_L - \rho_v)^2 \int_0^{+1} ds \int_{r_c}^{\infty} dr \, coth\left(\frac{rs}{d}\right)\left(3s^3 - s\right) r^{-3} \qquad (5.3)$$

Where ε and σ are the Lennard-Jones parameters for the molecules, ρ_L and ρ_V are the densities of the liquid and vapour respectively, r is the distance between particles, r_c is the cut-off applied to the van der Waals forces, d is the interfacial thickness parameter, and is equal to $t/2.1972$, where t is the 10-90% thickness of the interface.

This correction may be shown to have an upper bound (see Appendix F), applicable for very sharp interfaces.[98] This is given in Equation 5.4.

$$\gamma_{LRC} = \frac{3\pi\varepsilon}{2r_c^2}\left(\rho_L^{*2} - 2\rho_L^*\rho_V^* - \rho_V^{*2}\right) \qquad (5.4)$$

Where ρ^* represents the Lennard-Jones reduced density, $\rho\sigma^3$. Both the full correction (Equation 5.3) and the upper bound estimate (Equation 5.4) have been

applied to the pure water slabs at each temperature. As the interfacial region broadens with increasing temperature, so the long-range correction decreases. This correction is only dealing with the van der Waals forces which decay with $1/r^6$. The pressure profile calculations have been carried out with an electrostatic truncation, and it is likely that there will be significant error introduced into the surface tension due to the truncation of these forces, which decay with $1/r$.[98] However, the cutoff used is a very long one,[92] and thus, the errors from the van der Waals cutoff are likely to be the more significant.

This addition of a long-range correction term which is included only at the end of a simulation run has been criticised recently,[99] in favour of including consistent calculation of the contribution throughout the simulation. This is not trivial to implement, and so the long-range correction addition at the end of a simulation run is still used extensively.

The interfacial 10-90 thickness and surface tension has been calculated on pure water Slabs 1 and 3, and is shown in Table 5.2 at a range of temperatures between 298 and 411 K, for comparison to the work of Alejandre *et al.*[67] and Taylor *et al.* The general trends in the data are very similar, and the values obtained for the surface tension are reasonably close, being within 5 mN m^{-1}. All three sets of data compare favourably to experimental data on the surface tension of water, with the data from Alejandre being the closest. This is almost certainly due to the full electrostatic treatment used by this group. The interfacial 10-90 thickness cannot easily be compared to experimental data, as this is difficult to quantify through experiment. X-ray reflectivity has been used to estimate the ''surface roughness''' of the water interface, but the values obtained have not been consistent.

	N	Temperature / K	10-90% thickness / Å	γ / mNm^{-1}	γ_{LRC} / mN m^{-1} (full integration)	γ_{LRC} / mN m^{-1} (upper bound estimate)	γ_{total} / mN m^{-1}
Slab 1	265	298	2.80(0.03)	59.0	5.33	5.52	64.3
Slab 1	265	316	3.11(0.05)	54.6	5.33	5.55	59.9
Slab 1	265	328	3.19(0.07)	55.1	5.29	5.52	60.4
Slab 1	265	367	4.20(0.03)	54.4	4.78	5.11	59.2
Slab 1	265	411	9.65(3.5)	42.4	3.62	4.67	46.2
Slab 3	3064	298	3.99(0.1)	62.4	4.36	4.60	66.8
Slab 3	3064	316	4.65(0.05)	58.1	4.29	4.59	62.4
Slab 3	3064	328	5.00(0.1)	58.2	4.23	4.56	62.4
Slab 3	3064	367	7.53(0.3)	50.0	3.64	4.22	53.6
Slab 3	3064	411	12.0(5.0)	42.1	2.85	3.86	45.0
Alejandre *et al.*[67]	512	328	2.99	60.5	5.5	-	66.0(3.0)
	512	367	3.62	53.5	5.0	-	58.5(3.2)
	1000	316	3.13	67.4	4.1	-	71.5(3.5)
	1000	411	5.05	49.9	3.3	-	53.2(3.7)
Taylor *et al.*[91]	526	298	3.32	-	-	-	65.0(2.0)
	526	323	3.42	-	-	-	58(2.0)
	526	348	4.21	-	-	-	51(1.0)
	526	373	4.50	-	-	-	47(1.0)

Table 5.2: Surface tension and interfacial thickness derived from Slabs 1 and 3 (SPC/E water) at various temperatures. Also shown are the results which Alejandre and co-workers[67] and Taylor and co-workers[91] reported within the same temperature range.

Orientational Profile of Water

The orientational profile of the water dipole has been calculated as a further comparison to the work done by Sokhan and Tildesley. Figure 5.4 shows the $\langle P_1 \rangle$ order parameter profile as a function of the z-coordinate of the slab. As Sokhan and Tildesley observed, there is clearly a preferred orientation of the water molecules at the interface, with the dipoles tilted towards the liquid phase. The feature of a two-layer interface is also visible, where, at the Gibbs' dividing surface, the orientation of the water flips. The orientation preference below the dashed line (i.e. on the water side of the dividing surface) is dipole facing the centre of the slab. On the vapour side, the dipole has a tendency to point towards the bulk vapour. Beyond this region, the data becomes noisy due to the very small number of molecules present.

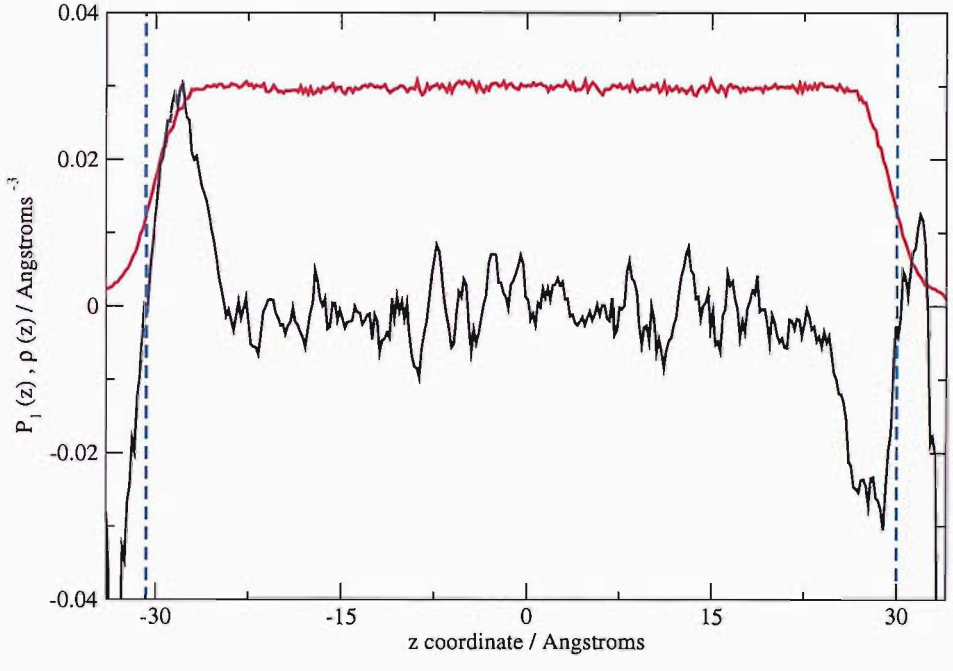

Figure 5.4: The orientational ($P_1(z)$) profile of the SPC/E Slab 4 (black line), shown alongside the density ($\rho(z)$) profile of the system (red line). The dashed blue line indicates the calculated position of the Gibbs dividing surface.

5.1.4 Summary

In this section, previous molecular dynamics simulations carried out on the water/vapour interface have been reviewed, and used as a basis for verifying that the water systems set up for use in this project are modelling water correctly. Some more detailed comparisons have been made to the work carried out by Alejandre and co-workers, and Sokhan and Tildesley, since their work links very closely to experimental observations on surface tension and indeed non-linear optical properties.

The water slabs larger than Slabs 1 and 2 (20 Å depth) appear to be stable and equilibrated, and are displaying reasonable surface tensions and density profiles. The orientational profile is also in good agreement with the literature, and the calculated surface tensions are in good agreement with experiment and previous work.

5.2 Crown Ether Simulations

Previous Work

The majority of the literature for theoretical studies on crown ethers appears to focus on 18-crown-6 and its derivatives (due to their applications in supramolecular chemistry),[100] and calix-arene type compounds (due to the scope for design to enhance ion capture).[101,102]

Wilson *et al.* carried out NMR and *ab initio* studies on the structure of 18C6, benzo-18-crown-6 and dibenzo-18-crown-6.[103] From the *ab initio* studies, they derived structural changes on complexation, binding energies and changes in electron distribution. The effects of solvation were also studied theoretically. Qualitative agreement was reported with available experimental data for ion selectivity, and for structural data. Agreement is also reported between the group's NMR data and *ab initio* results in terms of the changes in conformation and the atomic charge distribution.

The study carried out by the US Department of energy,[41] previously mentioned in Part I, utilised both *ab initio* and molecular mechanics methods very successfully.[104] The researchers found that the molecular mechanics force fields available at the time (1997), were not sufficiently parameterised to reproduce experimental conformations of the crown derivatives being studied, and so *ab initio* work was carried out to generate suitable parameter sets based on the MM3 force field. These parameters were optimised then by comparison of MM simulations to NMR observations. The group found that subsequently very strong agreement was found in terms of conformations observed and increased cation specificity with certain modifications, when the molecules were synthesised and experimental work carried out.[105] The computational modelling in this study was of great use in the choice of modification of the calix[4]arene crown compounds.

Simulations carried out on crown ethers using the AMBER force field, or modifications of it, are plentiful. Kollman and co-workers carried out several molecu-

lar mechanics simulations on 18-crown-6 with and without cation presence.[106–109] These simulations reproduced the experimental trends relating to binding preferences and complexation free energies. The behaviour of 18-crown-6 (18C6) at the water-chloroform interface was studied by Troxler and Wipff,[110] again using the AMBER force field, as part of a series of simulations of ionophoric compounds and their complexes.[111] They studied 18C6 in its uncomplexed form, and then in its complexed form with K^+Pic^- and with $Sr^{2+}2Pic^-$. The simulations were carried out in the NVT ensemble, and the interface was created by two adjacent boxes, one of water (TIP3P) and one of chloroform (OPLS). These simulations were 1 ns in length. For the uncomplexed crown ether, a standard treatment of electrostatics was employed - that is, a cutoff treatment was used even for nonbonded interactions. This is justified by the authors due to the 18C6 being neutral and only weakly polar. The free 18C6 showed a strong affinity for the interface, which is consistent with a number of other studies involving extractant molecules. The orientation of the crowns at the interface in the free 18C6 simulation matched that obtained in the simulations with ion presence: that is, adsorption at the interface appears to result in a preorganisation of the crown ether for complexation. Generally, the simulation timescale was too short to allow much complexation, although a small amount did occur. Also, different starting conditions and configurations did not converge in this time, supporting the argument for longer simulation times. The simulations indicate that the complexed crown ether is more surface active than the free crown ether. This has been observed in other simulations by the authors for other systems, and is also reported in experimental systems, as well as being observed in the experimental work done in this project. Some simulations on 21-crown-7 and derivatives were also carried out using the AMBER force field by Lamare *et al.*[102]

In general, the study of surface active molecules at the water/air interface is a heavily researched area due to the range of molecules which function there. For example, there are molecules with applications which range from detergents to macromolecular structures, catalysis and ion transfer. Lipid bilayers are also formed from surfactants, and are important when looking into drug design.[112–114]

Of the many computational studies on such molecules, a few will be reviewed here in relation to this project. In simulations of any surface behaviour at the water/air interface at ambient temperature, even that of partially soluble surfactants, the species of interest is almost invariably placed at the interface from the beginning of the simulation. The timescales of most simulations carried out (up to a few nanoseconds) are not yet long enough to allow the simulation of diffusion from bulk to interface and equilibration at the interface, unless the surfactant is somehow constrained to encourage migration. For example, Tomassone *et al.* carried out an investigation into the bulk to surface migration using an interaction potential to determine the degree of migration observed.[115]

Sokhan and Tildesley's study on the behaviour of phenol at the water/air interface[116] is particularly relevant to this work as they apply the same methodology, and also analyse their findings with direct relation to SHG experimental results on the system.[117] The simulation looks at a range of surface coverages of phenol. These are acheived by treating each interface of the water slab as entirely independent and placing a different number of phenol molecules on each interface. In this way, the authors manage to effectively simulate two systems simultaneously. However, some migration across the water was observed, so that the system concentrations did not remain exactly as they were at the beginning of the simulation. The simulations reported in this paper were 2 ns long, with a 0.6 ns equilibration period. Orientational distributions of the molecules are calculated, and the average tilt angle between the long axis of the molecule and the surface normal is reported to be approximately 128 ± 8^{o} throughout the concentration range. This is in good agreement with the experimental studies, which reported a tilt angle of 130 ± 5^{o}. The authors also note that the orientational profile of the water slab was altered in the presence of phenol molecules, as compared to the pure water slab.

A combined SHG and MD study on polarisable anions at the liquid water surface has also been recently published by Petersen *et al.*[118,119] The purpose of this study is largely to broaden understanding of how such anions behave in the interfacial region. The simulations showed that the concentration of species was not

uniform throughout the interfacial region, that is, the region which has been studied through experiment. In fact, the species has a high concentration very near to the boundary between phases, but is at much lower concentration slightly below that.

In Michael and Benjamin's MD study on N,N'-Diethyl-p-nitroaniline (DEPNA) at the water/air interface,[120] the agreement with experiment is not as good, with the DEPNA average tilt angle from the MD studies being 73°, and that from SHG being 55°.[121] However, as discussed in Section 2.2, this discrepancy could be due to the limitations of the SHG analysis, rather than the simulation. The study uses a flexible SPC potential to model water, and the simulation is just 1 ns in length, with an equilibration period of 0.1 ns.

A study was carried out on Monododecyl Pentaethylene Glycol at the water/air interface by Kuhn and Rehage.[122,123] The authors of this study used the SPC model for water, and a simulation length of 1 ns. The reported the average tilt angle for the surfactants as about 11° for the hydrophobic part and 169° for the hydrophilic part. These values are not then compared to experimental studies.

Borodin and Kiselev carried out MD simulations on the porphyrazine monolayer at the water/air interface,[68] using the SPC water potential. In this study, the authors found that the tilt angle was distributed such that three preferred values were seen: 76°, 56° and 23°. This study again highlights the issue that the surface species modifies the underlying water layer.

Recent studies include that of Chanda *et al.*,[124] on Aerosol-OT surfactants, and Roeselová *et al.*[125] on the hydroxyl radical at the water/air interface. Both of these studies have atmospheric implications.

5.2.1 Benzo-15-Crown-5 Simulations

The starting structure for the benzo-15-crown-5 simulations was the crystal structure of the experimental sample,[126] shown in Figure 5.5, which compared well to

the published crystal structure of the molecule.[127]

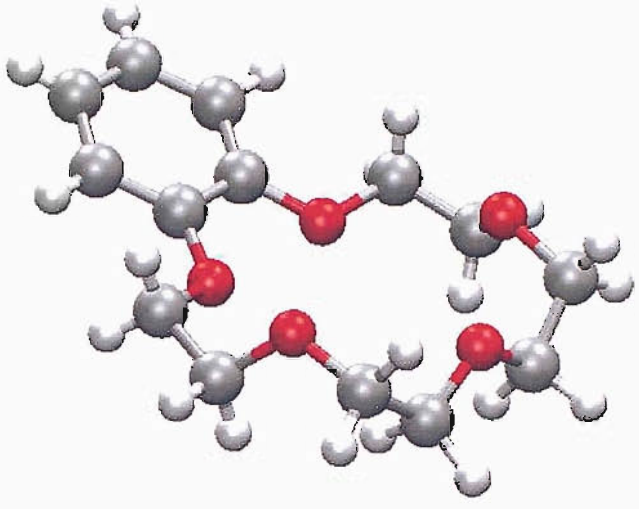

Figure 5.5: The crystal structure of benzo-15-crown-5.

To determine suitable parameters for the simulation of the crown ether, the geometry of the molecule was first optimised semi-empirically, using the PM3 method in MOPAC 97,[128] to remove any crystal structure defects. This was followed by *ab initio* optimisation which was carried out at the Hartree-Fock / 6-31G* level in Gaussian 94.[129] The atomic charges on the molecule were subsequently generated using the RESP (restrained electrostatic potential) method.[130] These are shown in Figure 5.6. The Lennard-Jones parameters taken from the 1999 parameter file (parm99),[131] are shown in Table 5.3.

The crown ether molecules were minimised in the gas phase (1000 steps) using the NAMD molecular dynamics package as detailed in Section 5.1, using the conjugate gradient method, and these minimised structures have been used as a starting point for all subsequent simulations.

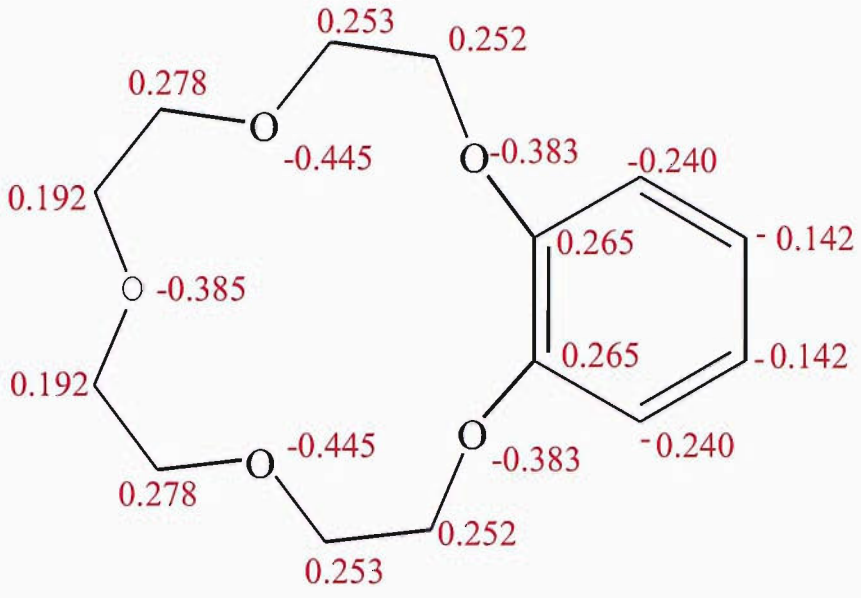

Figure 5.6: The RESP charges generated for benzo-15-crown-5.

Atom	Atom Type	σ	ε	parameter set
Aromatic Carbons	CA	1.9080	0.0860	parm99.dat
Crown Ether Carbons	CT	1.9080	0.1094	parm99.dat
Crown Ether Oxygens	OS	1.6837	0.1700	parm99.dat

Table 5.3: Lennard-Jones Parameters for Benzo-15-Crown-5 Atoms

5.2.2 Benzo-15-crown-5 in Bulk Water

A simulation of a single crown molecule in bulk water was set up so that conformational properties in solution could be compared to those at the interface. A crown ether was placed roughly centrally in a cubic box, originally consisting of 3064 water molecules (Box 3). Water molecules within 2 Å of a heavy crown atom were then removed to avoid overlaps during equilibration.

To equilibrate the system, the crown ether in bulk was minimised (for 5000 steps) using the conjugate gradient method in NAMD, heated to 298 K (10 ps at 100 K, 10 ps at 200 K and 20 ps at 298 K) under NVT conditions using a 2 fs timestep, a Lennard-Jones cutoff of 11 Å, with a switching function applied from 9 to 11 Å, and a Langevin thermostat with a damping parameter of 5 ps^{-1}. Once brought to the desired temperature, the system was run in the NPT (isothermal-

isobaric) ensemble: the Langevin thermostat damping was set to 10 ps^{-1}, and for 100 ps the Nosé-Hoover piston barostat with a pressure target of 1 atm, a piston temperature of 298 K, a damping parameter of 200 fs and an oscillation period of 400 fs was used. A further 400 ps was run with the barostat piston damping parameter at 400 fs, and the piston decay at 300 fs. The SHAKE algorithm was applied to all bonds, and test simulations run under constant N, V and E conditions confirmed that the energy fluctuations were smaller than 1 in 10^3 (usually 1 or 2 in 10^4) for a 2 fs timestep, which was the fluctuation quoted by Sokhan and Tildesley[116] in their simulations of phenol at the water/air interface. The production phase (10 ns) was run under identical NPT conditions to the last 400 ps of equilibration.

Analysis

Two sets of planes were selected in order to look at conformations preferred within the molecule, as shown in Figure 5.7. The simulation cell sides after equilibration are approximately 45 Å. Thus, the crown is at high dilution.

The angle between the planes within the crown ether part remains constant throughout the bulk simulation (Figure 5.8). Thus, it appears that no puckering of the crown ether ring occurs.

From Figure 5.9, which shows the angle between the benzene plane and the crown ether plane, it can be seen that the molecule has a preferred conformation, where the angle between the planes is about $\pm 20^{\circ}$: that is, a roughly "flat" conformation, but that there is significant population of a "bent" conformation where the angle between the planes is approximately $\pm 90^{\circ}$.

5.2.3 Benzo-15-crown-5 at the Water-Air Interface

Using the equilibrated water slabs discussed in Section 5.1, a range of interfacial simulations were set up to represent the experimentally determined surface concentration over the range studied. The derived area per molecule as calculated from the surface tension measurements on benzo-15-crown-5 is shown in Figure

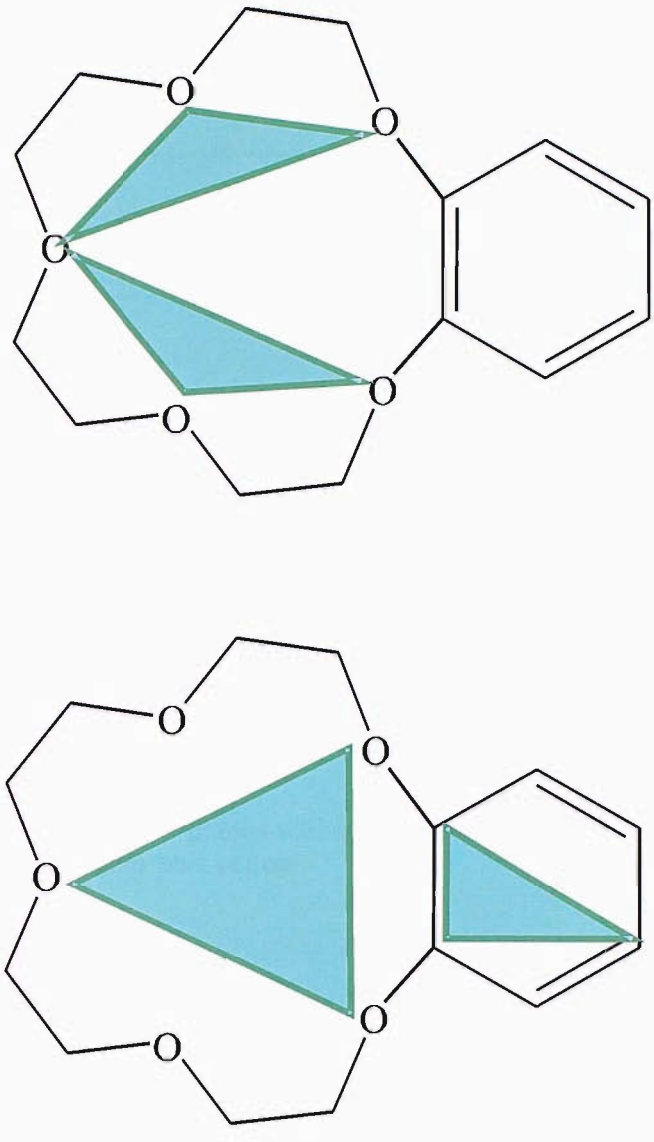

Figure 5.7: The angle between the planes within the crown ether part (top) will show whether any puckering of the crown ether part occurs, and the angle between the benzene part and the crown part (bottom) will show whether the molecule is flat or bent.

5.10. The circled points are those which have been used for the initial setup of the MD simulations, and indicate how the approximate bulk concentration represented by each simulation has been estimated. This may not give an exact value of the concentration being simulated, as in experiment there will be effects from the presence of molecules in the bulk which will not be experienced by the simulated molecules. From Figure 5.10, the area occupied by each crown was created by placing an evenly spaced grid of N_s crowns at the interface, where N_s is found

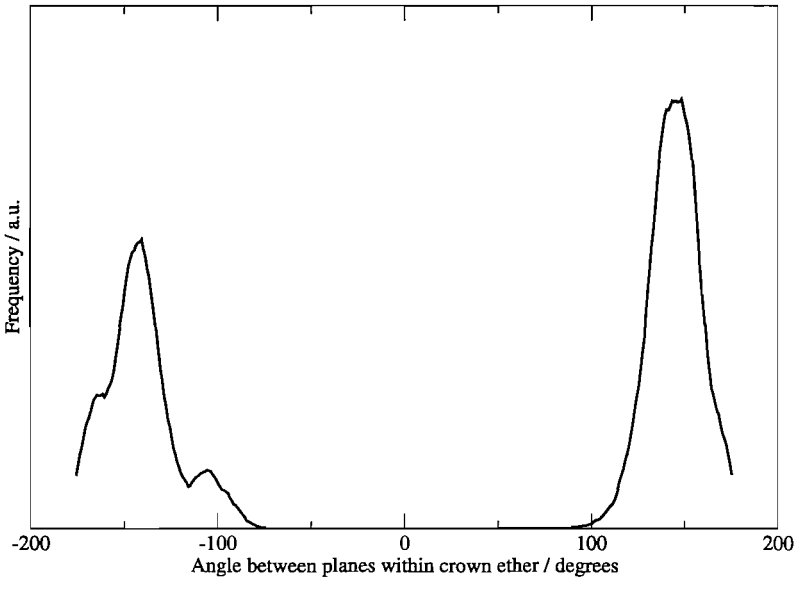

Figure 5.8: The angle between the planes within the crown ether part indicate that no puckering of the crown ether part occurs.

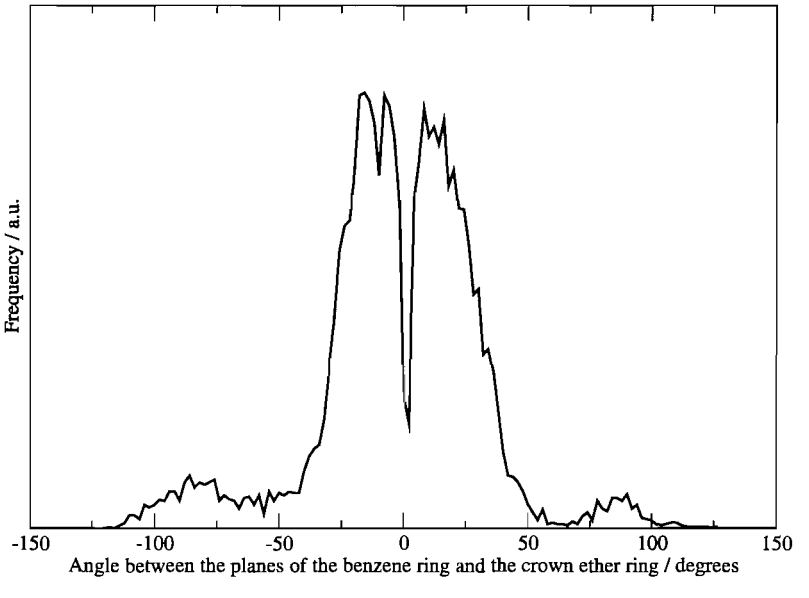

Figure 5.9: The normalised distribution of the angle between the benzene ring and the crown ether ring in bulk water.

by taking the desired area per molecule at each point, and then dividing the area of the water slab surface by the area occupied per molecule. A schematic of the initial setup of a simulation (in this case, a simulation where N_s=9) is shown in Figure 5.11.

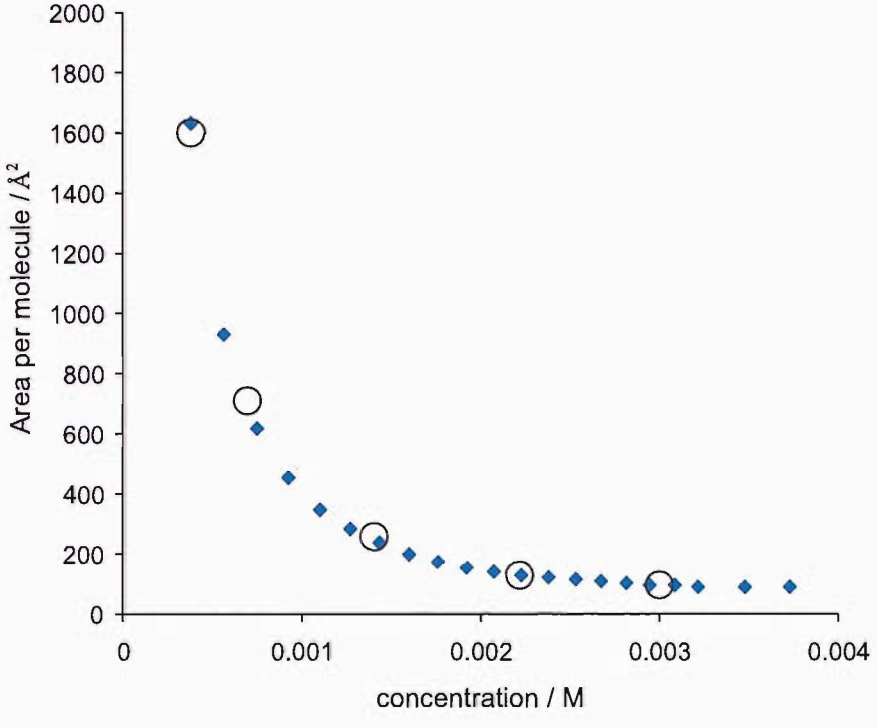

Figure 5.10: The plot of area per molecule derived from the surface tension experiments. The circles indicate the points along the plot for which an interfacial simulation has been set up. Simulations were also carried out on an infinitely dilute interface (1 crown), and on a saturated interface, according to the isotherms obtained experimentally (100 crowns).

No attempt was made to simulate the bulk concentration as an initial setup as the timescale for MD would be insufficient to allow diffusion and equilibration at the surface. The approximate bulk concentration represented by each surface grid is estimated from the experimental isotherms, and included in the table. For the grids of 4, 9 and 25 crown ether molecules, two different initial configurations were set up and run, as illustrated in Figure 5.12. This allows the effects of different starting configurations to be monitored. For the benzo-15-crown-5 the simulations run, along with information about the represented concentration according to the experimental isotherm, and the area per molecule, are shown in Table 5.4. The simulations will henceforth be labelled as in Table 5.4, where the label comprises

the number of crowns, N_s, followed by the starting configuration of the crowns, where I indicates a grid of crown ethers parallel to the interface (flat configuration, Figure 5.12 (a)) and II indicates a grid with crown ethers perpendicular to the interface (upright configuration, Figure 5.12 (b)).

The grid was placed such that the closest atoms of the crown ethers did not touch the water slab, so that no water molecules needed to be removed, but were close enough that the crown molecules were quickly adsorbed onto the surface during the equilibration phase.

Initially, the water molecules were fixed, and the crown molecules were minimised (5000 steps). The equilibration period (under NVT conditions) was then 0.5 ns, which is a relatively long period, and was intended to remove any dependence on the starting orientation of the molecules. The thermostat damping parameter was 1 ps^{-1}, with the Lennard-Jones and electrostatic treatments as detailed for the bulk system. Subsequently, for the production runs of 10 ns, the systems were under the same NVT conditions, but the pressure profiles were reported every 5 timesteps (10 fs).

A range of early simulations were run on the various water slabs discussed (Slabs 3 to 5) with a single crown ether on each interface. The results showed that there was significant corellation between the movement of the crowns. This is unacceptable, as it implies the interfaces are not independent as desired, and indicates that there are size issues with this slab depth ($\approx$45 Å). Test simulations were run using a long range cutoff instead of PME treatment for the electrostatic interactions, but no improvement was seen. For this reason, this slab was not used for the simulations. Slab 4, with dimensions $L_x = L_y = 80$ Å, $L_z = 300$ Å, and water depth of 60 Å (containing 12916 water molecules) did not show this behaviour. Consequently, all production runs were carried out using this size of slab. The greater surface area of this slab also enabled the investigation of a wider range of surface coverages.

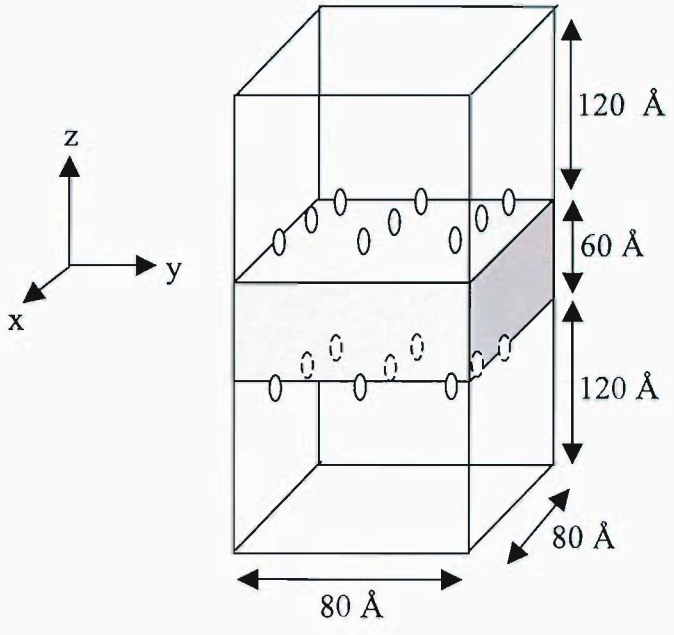

Figure 5.11: The simulation cell as set up for a 9 crown simulation, with an evenly spaced square grid of molecules on each interface. The cell dimensions are shown for Slab 4, as used for the 10 ns simulations reported.

Simulation Label	N_s	Starting Configuration	Area Occupied per Crown / Å^2	Bulk Concentration represented / M
1I	1	Flat	6400	Infinite Dilution
4I	4	Flat	1600	< 0.0005
4II	4	Upright	1600	< 0.0005
9I	9	Flat	710	0.0007
9II	9	Upright	710	0.0007
25I	25	Flat	256	0.0014
25II	25	Upright	256	0.0014
49II	49	Upright	131	0.0020
64II	64	Upright	100	0.0025
100II	100	Upright	64	0.0035+ (monolayer)

Table 5.4: The simulations run on benzo-15-crown-5, including the configuration of the molecules, the area occupied per molecule, and the bulk concentration represented at the start of the simulations.

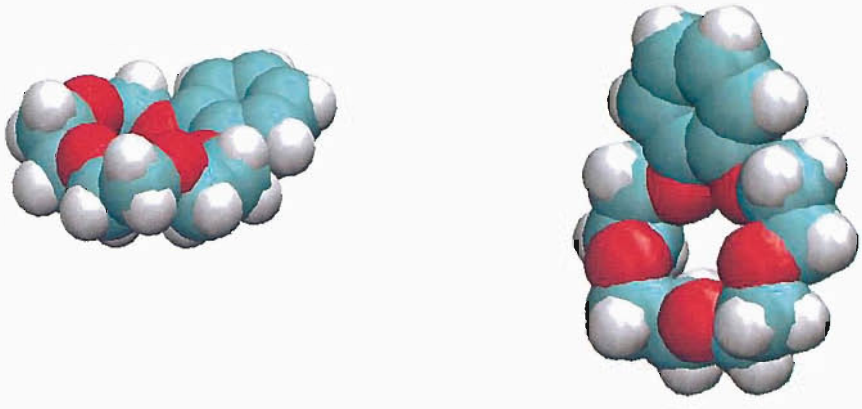

(a) Flat starting configuration, I (b) Upright starting configuration, II

Figure 5.12: The two starting configurations used in the simulations, taking the interface as parallel to the bottom of the page.

5.2.4 Results and Discussion

The analysis performed on the crown ether systems has been chosen with a view to the comparison with experimental data gathered in this project. However, it will be presented purely in terms of a description of the computational system in this section, and will be compared to the experimental work in Part III of this thesis. For clarity, though, in the list of analyses given in this section, some reference to the relevance of the parameters derived is useful.

For each system several parameters describing the behaviour of the molecules are reported. These are:

1. The angles formed between various planes within the molecules are investigated to highlight conformational preferences of the molecules.

2. The extent to which the benzene ring is submerged or above water is calculated with respect to the position of the interfacial Gibbs dividing surface.

This may be used to estimate an interfacial refractive index of the system which can then be related directly to the SHG analysis.

3. Calculation of the Euler angles, θ, ψ and ϕ, between the molecular and the simulation cell axes, as defined in Section 2.2. Assumptions on these angles are made when fitting SHG data, and their explicit calculation from the simulation trajectories will aid with the evaluation of the assumptions employed.

4. The order parameters $\langle P_1 \rangle$ to $\langle P_3 \rangle$ which are the first three Legendre polynomials in cos θ.

$$\langle P_1 \rangle = \langle \cos\theta \rangle \tag{5.5}$$

$$\langle P_2 \rangle = \langle \frac{3\cos^2\theta - 1}{2} \rangle \tag{5.6}$$

$$\langle P_3 \rangle = \langle \frac{5\cos^3\theta - 3\cos\theta}{2} \rangle \tag{5.7}$$

These polynomials in $\cos\theta$ are once again related to the SHG analysis. In this case, the order parameter, D, whose value is derived through the analysis of SHG polarisation data, may be calculated and compared to the experimental work.

5. The functions $\langle \cos^3\theta \rangle$, $\langle \cos\theta \sin^2\theta \sin^2\psi \rangle$, $\langle \cos\theta \sin^2\theta \rangle$,$\langle \sin^2\psi \rangle$ are also derived from the simulations. The functions will determine various inter- dependencies of the Euler angles, and again, will help to clarify the validity of the assumptions made for the SHG analysis. These results are discussed in section III, in relation to their implications for experimental analysis.

6. The pressure profile for each simulation is calculated, giving the surface tension of that system.

7. The inter-crown distances and positions are investigated, using radial distributions and 3-dimensional plots. This is to give a clearer picture of how the crowns are influencing each other on the interface.

System averages are taken over all crown ethers on each of the interfaces over the entire 10 ns trajectory. Individual crown ether averages are also observed over the entire trajectory for clarification of the situation at the interface. The parameters are calculated every 0.5 ps and are then averaged for all crowns in one simulation.

Interfacial Conformations

The angles between the planes illustrated in Figure 5.7 were calculated for the interfacial simulations. The conformational distribution showed little difference to the bulk simulation, although it can be seen in Figure 5.13 that the molecule preferentially folds less at the interface than it does in bulk: this is probably due to the additional effects of the hydrophobicity of the benzene ring and the hydrophilicity of the crown. At the lower surface concentrations, N_s=4 and 9, a significant population of the interfacial crown ethers have an angle of $\pm 70^{o}$ between the normals of the crown ether plane and the benzene plane. This was not seen in the bulk simulation. It is apparent in the high surface concentration simulation, although less significant. The small population for which the angle is $\pm 100^{o}$ is seen at all concentrations, and is also apparent in the bulk simulation. The conformation leading to an angle of $\pm 85^{o}$ seen in bulk (Figure 5.8) is absent from all of the interfacial simulations. This is likely to be a conformation stabilised by hydration of the entire molecule.

The planes within the crown ether, shown in Figure 5.14, were fairly rigid, as seen for the bulk simulation. A snapshot of the straight conformation (Figure 5.15) and the bent conformation (Figure 5.16) are shown.

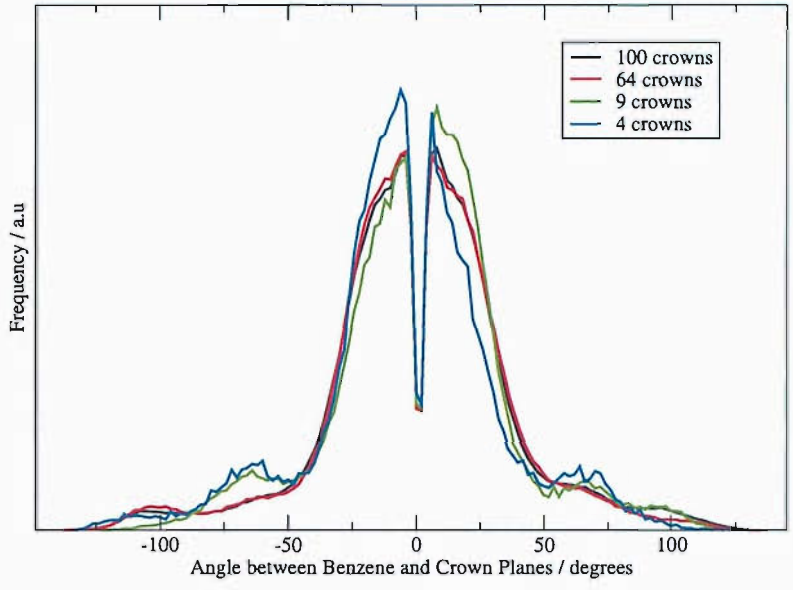

Figure 5.13: The distribution of the angle between the plane of the benzene part and that of the crown ether part for benzo-15-crown-5 at four interfacial concentrations.

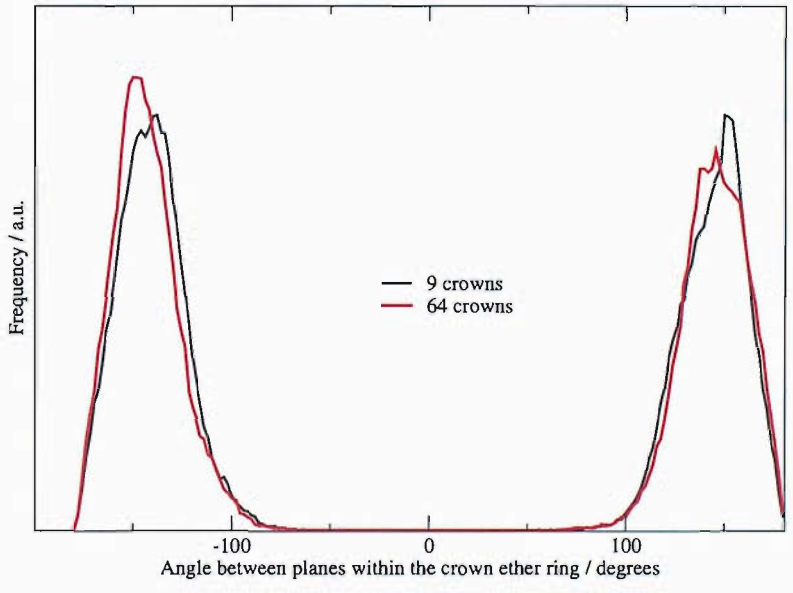

Figure 5.14: The distribution of the angle between two planes within the crown ether part for benzo-15-crown-5 at two example interfacial concentrations. Again, no evidence of any puckering or deformation of the ring is observed.

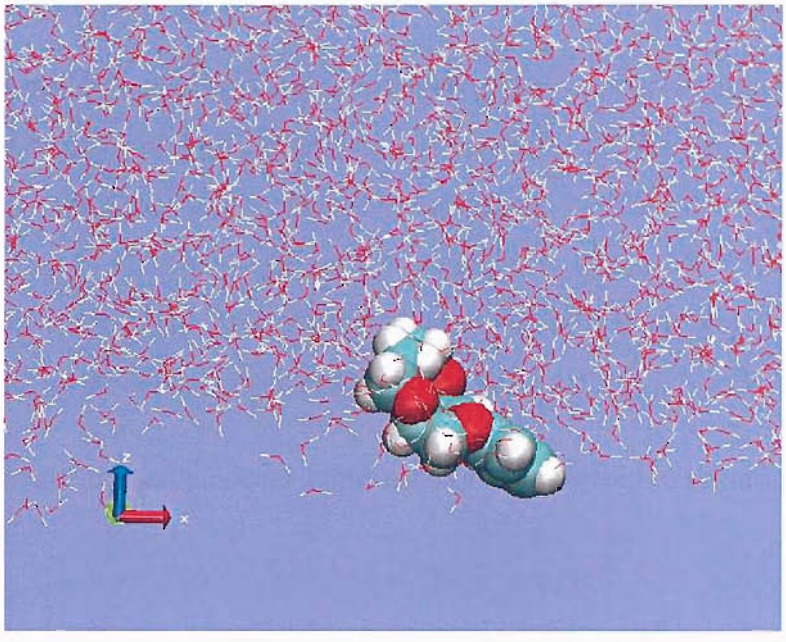

Figure 5.15: The straight conformation of benzo-15-crown-5 at the interface. This Figure shows a crown ether on the lower interface of the water layer. The red and white lines represent water molecules.

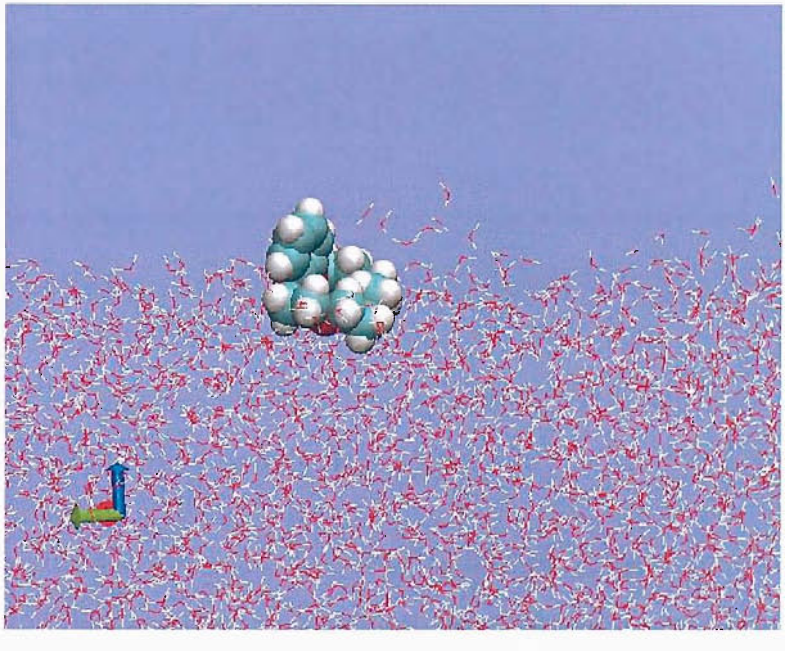

Figure 5.16: The bent conformation of benzo-15-crown-5. This molecule is on the upper interface of the water.

Interfacial Order Parameters

The way in which the crown ether is oriented at the water-air interface is of great interest for many of its applications, such as catalysis and phase transfer. Molecular dynamics simulations allow detailed examination of this ordering, and several parameters have been calculated here to characterise it. The tilt of the molecular axis (defined in Section 2.2) with respect to the surface normal is one such parameter and gives a good idea of the order at the interface.

The average tilt angle at each concentration is presented in Figure 5.17.

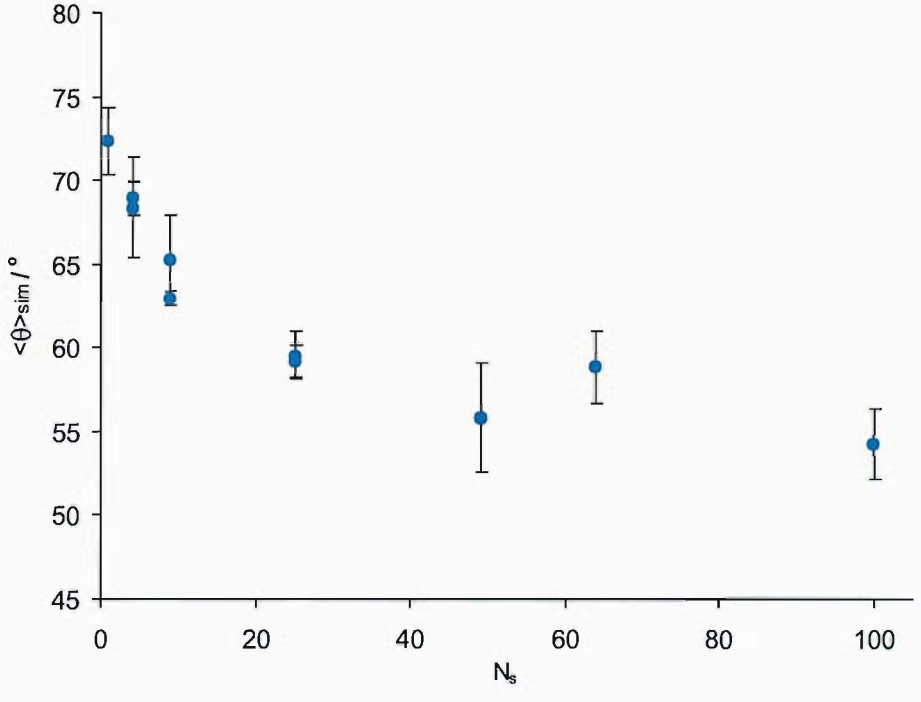

Figure 5.17: The average tilt angle calculated from the simulation as a function of concentration. The errors are estimated as the standard error of the average tilt angle on the two interfaces within each system.

From Figure 5.17 there is a clear trend in the average tilt angle with increasing concentration. As the surface concentration increases, the tilt angle decreases - that is, the molecular axis of the chromophore pushes towards the surface normal. The apparent increase in tilt angle for N_s = 64 can be explained if the distributions of the tilt angle for each concentration, shown in Figure 5.18, are also examined. The distributions show a skew with tilt angles below 90° favoured by the molecules. As

concentration increases, so does the population of the tail end of the distribution. The majority of the crown ethers still have an acute tilt angle, but some stabilisation effect of close neighbouring molecules is causing some molecules to remain with the benzene part submerged in the water.

In terms of comparison to the experimental data, it is the tilt angle which is of interest. However, from a mathematical point of view, the cosine of this angle gives a clearer indication of any preference away from a random distribution: the distribution of θ, if θ is uniform, will appear to have a peak at 90^{o}, whereas $\cos\theta$, for a uniform distribution will give a flat line, with no preference seen. Thus, the distribution of the cosine of θ for each of the concentrations is also given (Figure 5.19). It is clear from this data that there truly is a strong deviation from a uniform distribution, and that the crown ethers therefore have a preferred orientation.

The average value of $\langle P_1 \rangle$ is plotted with concentration in Figure 5.20, to show that the average deviates from the value 0, which would be obtained from a uniform distribution. Similarly, $\langle P_2 \rangle$ and $\langle P_3 \rangle$ are plotted with concentration in Figure 5.21.

A summary of the averaged values of the order parameters at all concentrations is presented in Table 5.5. From this data, it can be seen that the simulations carried out with different initial configurations, but the same number of crown ether molecules (denoted by I and II, where I indicates a simulation starting from a crown ether aligned parallel to the interface, and II represents one started with the crown ether perpendicular to the interface, with the crown ether ring closest to the water), the values obtained are equivalent, within the error bars. This suggests that the systems are well-equilibrated.

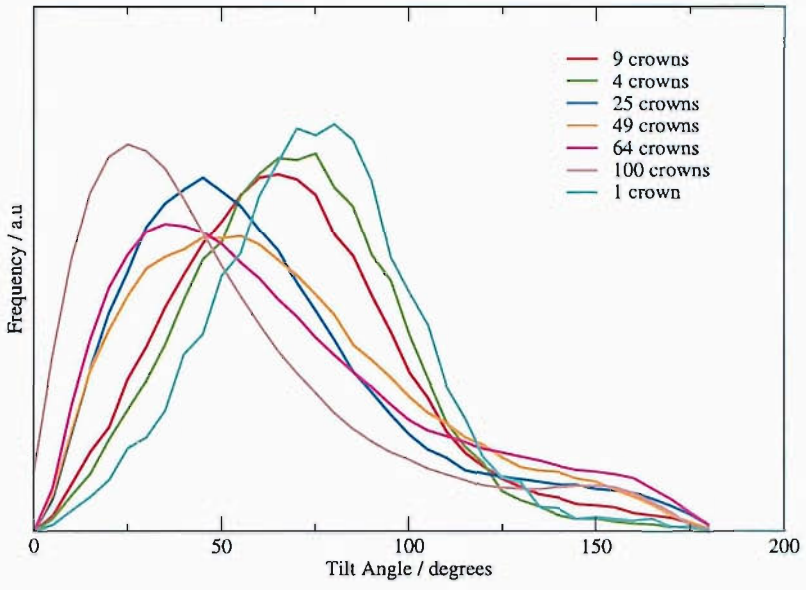

Figure 5.18: Tilt angle distributions at each concentration. The distributions are all normalised for comparison.

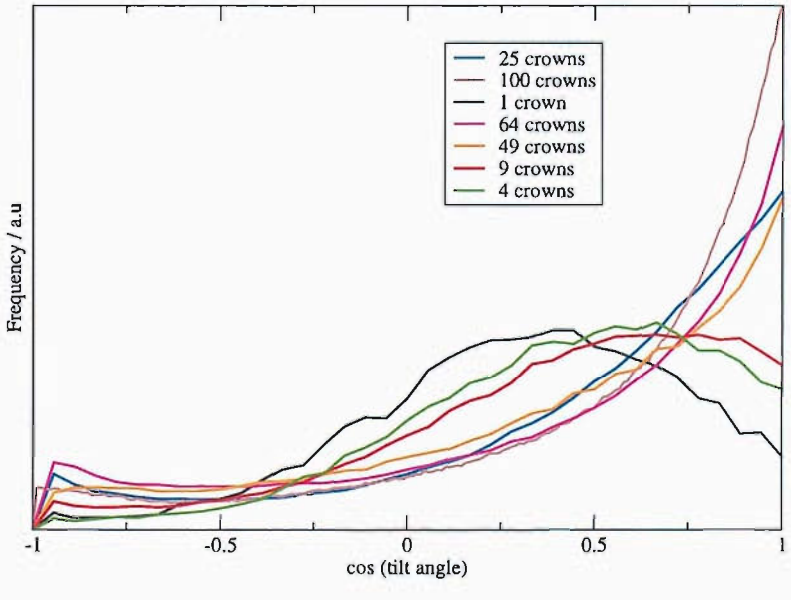

Figure 5.19: Distributions of cosθ at each concentration. Distributions are normalised.

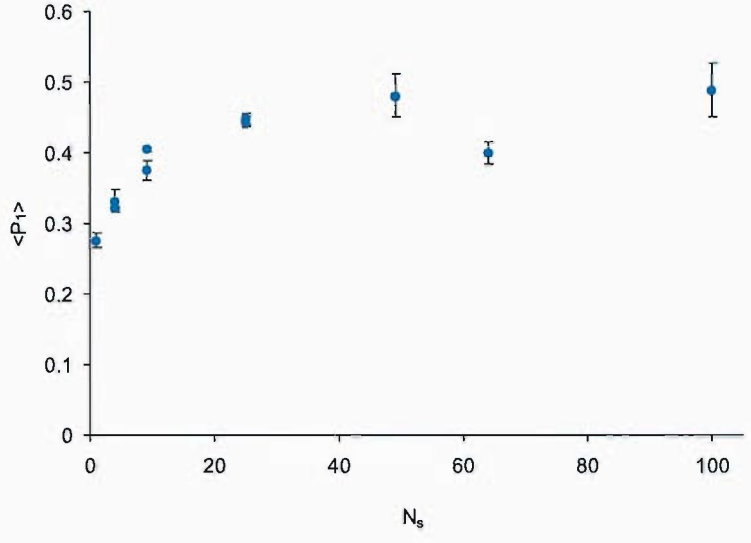

Figure 5.20: $\langle P_1 \rangle$ as calculated from the simulation as a function of number density of crowns.

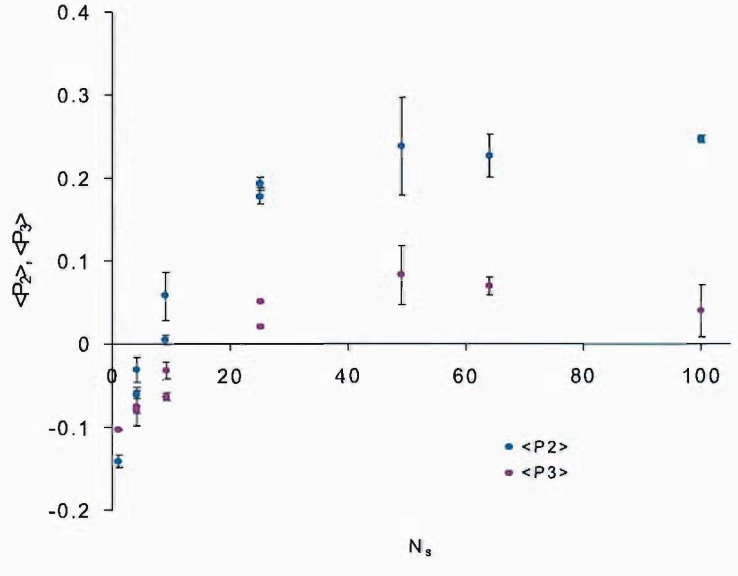

Figure 5.21: $\langle P_2 \rangle$ and $\langle P_3 \rangle$ calculated from the simulation as a function of number density of crowns.

Simulation	Bulk Conc/mM	$\langle P_1 \rangle$	$\langle P_2 \rangle$	$\langle P_3 \rangle$	$\theta_{sim}/^{o}$
1I	infinite dilution	0.2943(0.02)	-0.1369(0.02)	-0.1025(0.01)	72.0(4.0)
4I	below 0.5	0.3375(0.03)	-0.0591(0.02)	-0.0823(0.01)	68.0(2.0)
4II	below 0.5	0.3227(0.01)	-0.0317(0.01)	-0.0758(0.04)	69.5(0.2)
9I	0.7	0.3754(0.03)	0.0069(0.03)	-0.0639(0.01)	65.3(2.0)
9II	0.7	0.4072(0.01)	0.0617(0.01)	-0.0316(0.02)	62.8(2.0)
25I	1.4	0.4494(0.02)	0.1774(0.06)	0.0194(0.01)	59.8(2.0)
25II	1.4	0.4475(0.01)	0.1944(0.02)	0.0502(0.01)	59.3(2.0)
49II	2.0	0.4802(0.05)	0.2383(0.08)	0.0835(0.07)	55.9(0.5)
64II	2.5	0.3987(0.03)	0.2262(0.06)	0.0701(0.02)	62.4(2.0)
100II	3.5	0.4881(0.07)	0.2469(0.08)	0.0409(0.06)	54.3(0.5)

Table 5.5: Parameters derived from 10 ns of MD on each system, errors reported in brackets are 2 standard errors

For the Euler angle ψ, there are slight preferences apparent, as shown in Figure 5.22.

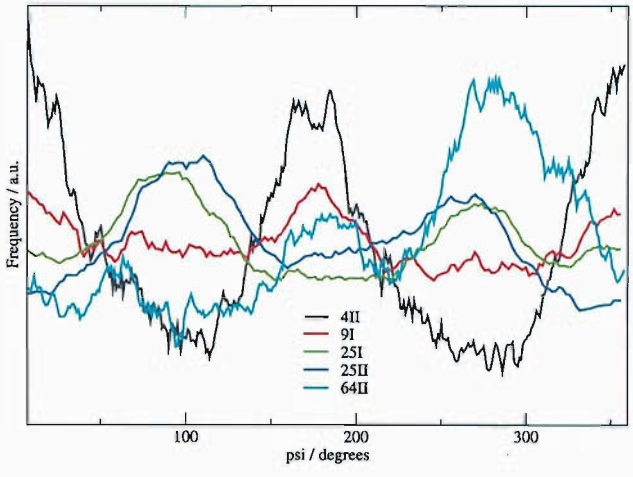

Figure 5.22: The distributions of ψ (over all crown ethers) for various benzocrown simulations.

At low concentration, there appears to be a strong preference for ψ=180°, which implies that the crown ether is sitting so that the plane of the molecule is parallel to the interface. At higher concentrations, this configuration is still apparent to varying extents, but the preference appears to be for ψ= 90 or 270°, which implies that the plane of the molecule is perpendicular to the interface (when projected onto the interface).

Interfacial Refractive Index

The interfacial refractive index of the system is an important parameter for optical surface studies. To investigate this property, the position of the chromophore centre (where the chromophore is the benzene ring and the nearest oxygens to it) has been calculated relative to the Gibbs' dividing surface throughout the simulation. This distance is reported in Table 5.6. The proportion of chromophore centres lying each side of the dividing surface is calculated, and the interfacial refractive index has then been estimated assuming linear interpolation between the refractive index of air (n_{air} = 1), and that of water (n_{water} = 1.334). That is, using the density profile of the water to determine the dividing surface position, and measuring the relative positions of the chromophores throughout the simulation, the interfacial refractive index of the layer has been calculated. Experimentally, there is a formulation for the measurement of bulk refractive index which includes the density of the species.[132]

Simulation	Dist from Dividing Surface / Å > 0 = vapour side < 0 = liquid side	$\langle n_{int} \rangle_{sim}$	Water-like or Air-like
1I	0.75(0.2)	1.140(0.071)	air
4I	0.60(0.2)	1.139(0.069)	air
4II	0.70(0.0)	1.004(0.007)	air
9I	0.75(0.2)	1.132(0.051)	air
9II	0.40(0.1)	1.135(0.063)	air
25I	1.1(0.1)	1.119(0.044)	air
25II	1.15(0.1)	1.107(0.062)	air
49II	1.75(0.2)	1.093(0.009)	air
64II	2.6 (0.3)	1.092(0.009)	air
100II	4.0(0.5)	1.050(0.060)	air

Table 5.6: Interfacial refractive index for the benzo-15-crown-5 system estimated from the simulations. The standard errors, as calculated over the two interfaces of each simulation, are given in brackets.

If the chromophore centres are, on average, exactly at the dividing surface, then an estimate of the interfacial refractive index as $\frac{1}{2}(n_{air} + n_{water})$ (that is, 1.167) for the SHG analysis is reasonable. However, it appears that on average, the chro-

mophore in the benzo-15-crown-5 simulations is slightly more air-like: Figure 5.23 is a plot of the average distance of the chromophore centre above the Gibbs' dividing surface.

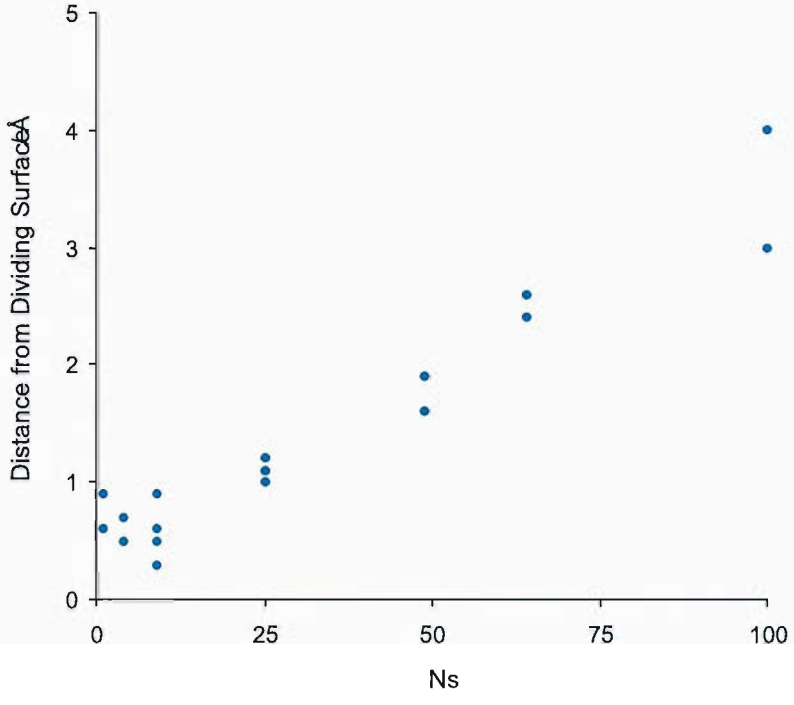

Figure 5.23: The relative position of the chromophore centre to the Gibbs' dividing surface. The dividing surface is located at y=0. For the benzocrown systems, it is seen that the chromophore centre is always on the vapour the dividing surface . The data is shown for both interfaces of each simulation to indicate the size of the errors.

The data indicates some concentration dependence, with the surface layer becoming more air-like as N_s increases. This implies that the refractive index assigned to the interfacial layer may also be concentration dependent.

Surface Tension

The surface tension of each system was calculated throughout the simulation, and is given in Table 5.7. The value of the surface tension, taking into account the magnitude of the adjustments seen in section 5.1 due to the long-range correction (between 2 and 6 mNm^{-1}), gives a value comparable to experiment (from 72.8 to 62 mNm^{-1}). However, the MD derived surface tension is not expected to change

(within the estimated errors) over the range of concentrations simulated, simply because the experimental changes in surface tension over this concentration range are so small: for the entire range, the experimental change in surface tension is no more than 3 or 4 mNm^{-1}. The calculation of surface tension from molecular simulation leads to large fluctuations between timesteps, and so this technique is not sensitive enough for the small changes in system seen here.

Simulation	$\langle\gamma\rangle_{sim}$ / mNm^{-1}
1I	57.3
4I	58.1
4II	58.8
9I	57.0
9II	58.0
25I	58.1
25II	58.2
49II	59.4
64II	59.4
100II	61.4

Table 5.7: The surface tension calculated for each benzo-15-crown-5 system.

Inter-crown order: Correlation between crowns

The inter-crown order has been investigated by means of the angle between the molecular axes of pairs of crowns, which will be denoted δ, and the distance between the benzene ring centres. The molecular axis, O_z, has been defined in Section 3.2. By calculating the distance between the benzene centres of neighbouring crowns, the effective radial distribution functions (rdf's), shown in Figure 5.24, were obtained. From these rdf's, a definite preference for neighbours to sit about 5.5 Å apart is seen. This value matches that reported by La Rosa *et al.*, from their simulations of poly(ethylene oxide) surfactants.[133] As stated by La Rosa, this is not due to π-stacking between the aromatic rings, which might be expected, as the distance between benzene rings which are π-stacking is about 3.4-3.6 Å. Note that the way in which the low concentration radial distributions tail off after the slight

second peak is due to the small number of crowns present in the system.

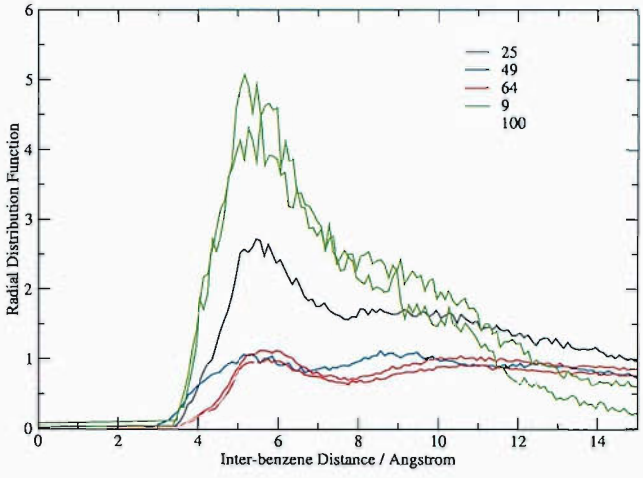

Figure 5.24: Radial distribution plots of benzo-15-crown-5 at each surface concentration. Two datasets represented by the same colour indicate the rdf derived from two starting configurations I and II. The lower concentration rdf's do not tend to 1 as there are very few crown ether molecules present.

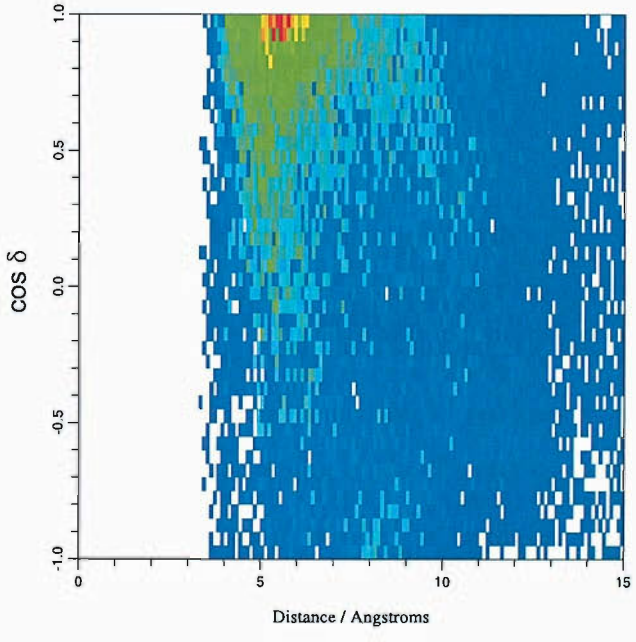

Figure 5.25: Distance correlation plot for a 9 crown molecule simulation showing a strong positive correlation peak at about 5.5 Å distance, where δ is the angle between the O_z axes of neighbouring molecules.

The preference for this separation is apparent even at low concentrations. With increasing concentration, a significant population with a separation of 10 Å is seen,

indicating ordered packing of the molecules. Two-dimensional plots illustrating the population of combinations of the cosine of the angle between the molecular axes of pairs of crowns against the distance between the benzene rings of those crowns are presented. The colour in these plots indicates the population density at each point on the plot, with red indicating a very high density of points, yellow a high density, down through green, pale blue (significant population) through to dark blue which indicates no significant population, and white showing no data. From such plots, the amount of "correlated" crown packing (that is, where the molecular axes are aligned and in the same direction), versus the anti-correlated packing (that is, where the axes are aligned, but in opposite directions) may be investigated. Looking at the 2-dimensional plots for benzo-15-crown-5 (Figures 5.25 to 5.27), the crowns clearly prefer to be positively correlated, which is in agreement with the behaviour seen for the tilt angles, which all tend to be acute with respect to the surface normal.

In Figure 5.25, which is the plot from a 9 benzocrown simulation, there is one dominant feature, and that is a high population of crown pairs for which the cosine of the angle between their molecular axes is 1.0 (i.e. they are aligned and in the same direction) and the distance between them is 5.5 Å.

However, at N_s = 64, a small proportion of anti-correlation is seen (Figure 5.26): there is a small amount of pale blue on the plot where cosineθ=-1 and distance=5.5 Å. Again, this is in agreement with the tilt angle distributions shown in Figure 5.18, as some crown molecules at this surface concentration do have a tilt greater than 90°. A similar patch of colour is seen on the same plot at about 8.5 Å. This is likely to be a result of some head to tail packing. At the highest concentration, shown in Figure 5.27 where N_s = 100, no anti-correlation is seen. This is probably an artefact of the number of crowns packed into the surface space when N_s = 100. It is likely that because of the tight packing of this number of crown ethers, the freedom to move away from the original configuration is very limited. At some future stage, it might be interesting to test this by starting from the unfavourable "benzene-down" position.

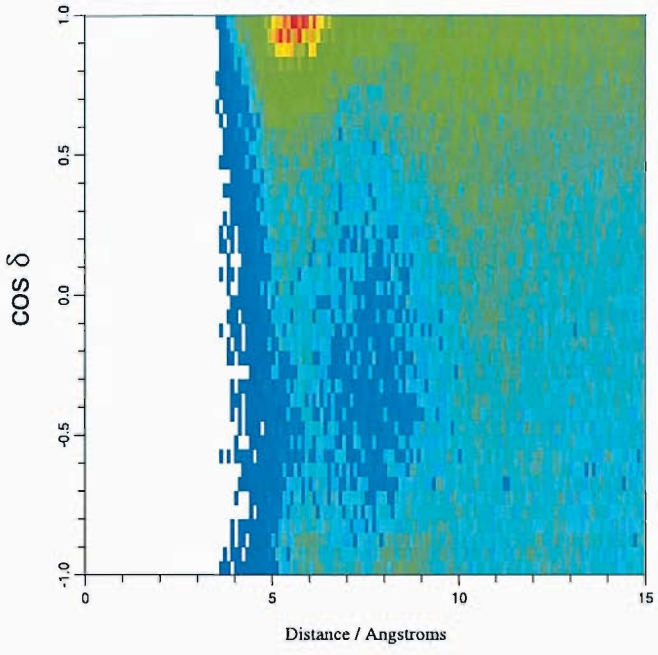

Figure 5.26: Distance correlation plot for a 64 crown molecule simulation. The strong positive correlation at 5.5 Å is still a predominant feature, but there is evidence of a second positive correlation peak in this simulation, and also of some anti-correlation.

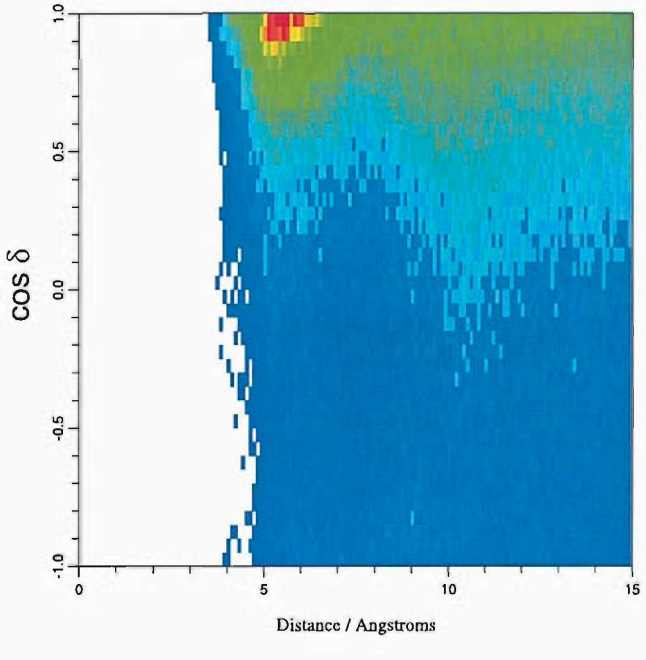

Figure 5.27: Distance correlation plot for a 100 crown molecule simulation. In this case, only the positively correlated peaks are apparent. It may be that at this saturation, the crowns are not free to move significantly from their starting configuration.

Looking at some snapshots from the N_s= 100 simulation, some aggregation is seen (Figure 5.28). The molecules pack together fairly tightly, although they re-

main at the interface (as indicated by the analysis of their positions relative to the Gibbs' dividing surface).

Summary

The interfacial behaviour of benzo-15-crown-5 over the concentration range from 0 to 3.5 mM has been investigated using MD simulations. There are clear trends with concentration of the interfacial order, with the crown ethers increasingly tilting towards the surface normal. At higher concentrations, there appears to be a proportion of crowns which have been stabilised with the benzene moiety submerged. For the Euler angle ϕ, a uniform distribution is seen, as would be expected for a liquid surface. The angle ψ does not show a strong preference, but there is some tendency for it to be 180^{o} (the peaks at 270^{o} are equivalent to those at 180^{o} since this is a fully symmetric molecule). The plane angles observed in the bulk are very similar to those conformations at the interface, although there is a tendency at the interface for the molecule to be less strongly folded, which is probably a result of the preference for the benzene to be unsubmerged, and the crown ether to be submerged.

The surface tension calculated from the MD simulations compares reasonably well to experimental data, but the pressure profiling method applied is susceptible to large fluctuations, and thus does not give the finer detail which would be necessary to detect the very small decrease in surface tension seen experimentally with increasing concentration.

Substantial inter-crown correlation is very clear from the 3-dimensional plots and the fact that the radial distributions show clearly that shells have formed. Benzo-15-crown-5 molecules on the water interface show strong positive correlation peaks, with only a small proportion of anti-correlation at N_s=64. This means that head to head stacking is favoured. This is a highly ordered system, which shows changing behaviour with concentration.

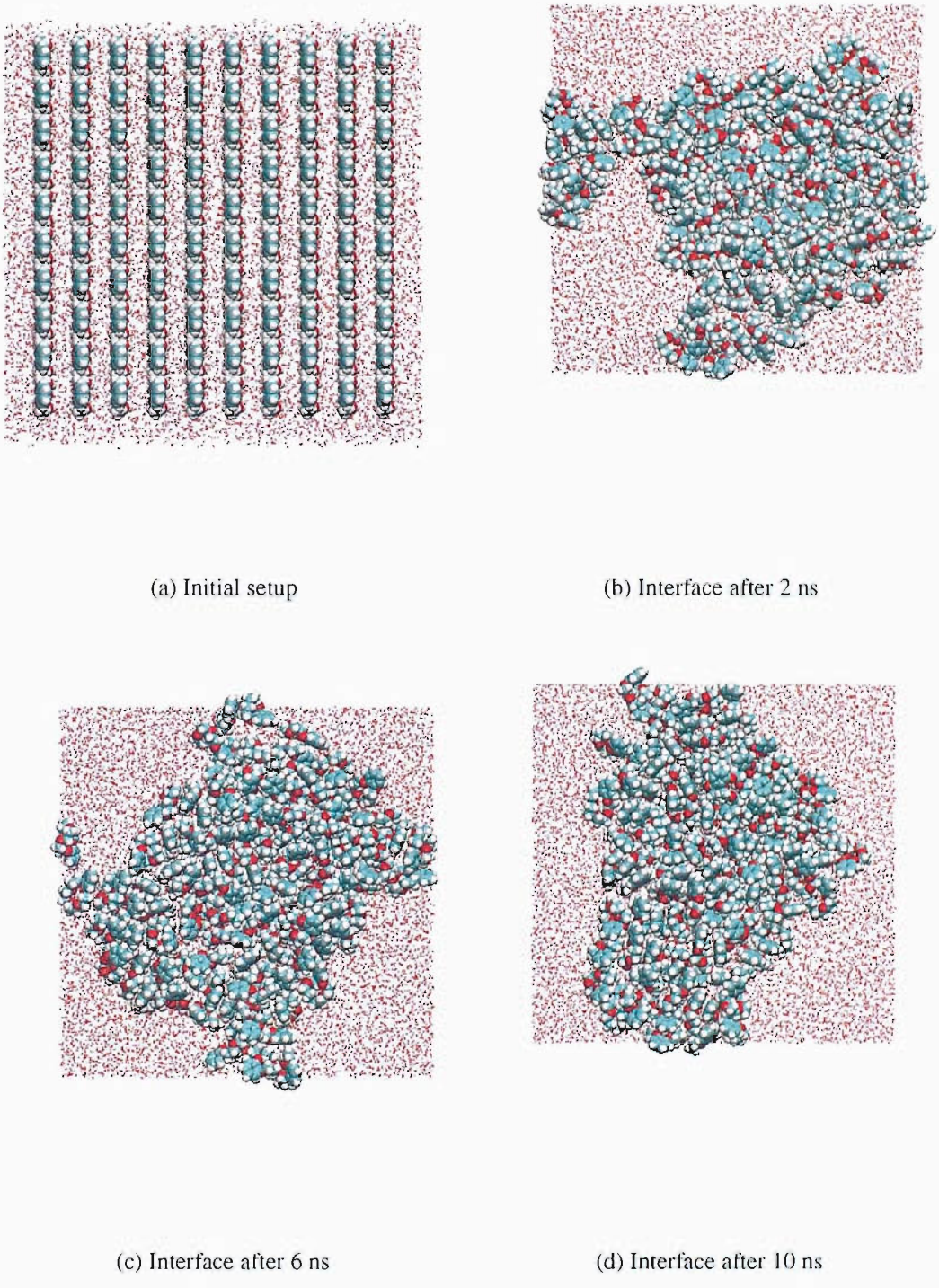

(a) Initial setup

(b) Interface after 2 ns

(c) Interface after 6 ns

(d) Interface after 10 ns

Figure 5.28: Snapshots of one interface in the 100 benzocrown simulation at 0 ns, 2 ns, 6 ns and 10 ns.

5.2.5 4-Nitrobenzo-15-Crown-5 Simulations

The same procedure was followed for the 4-nitrobenzo-15-crown-5 molecule as was used for the benzo-15-crown-5 molecule.

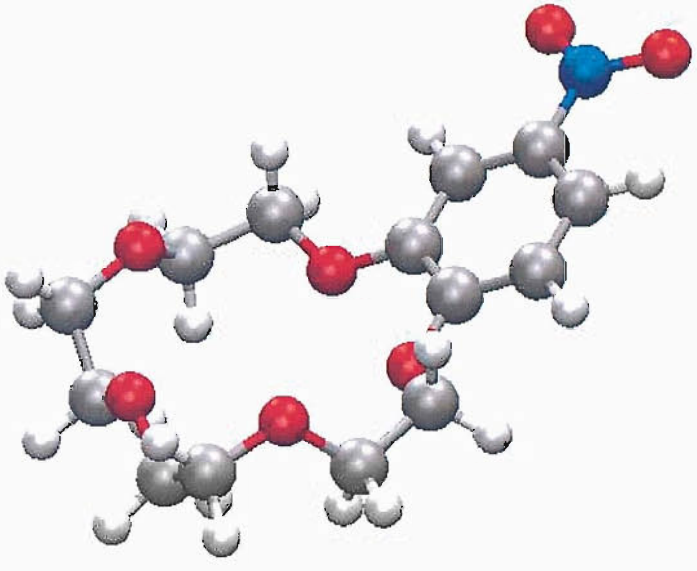

Figure 5.29: The crystal structure of 4-nitrobenzo-15-crown-5.

The crystal structure of the experimental sample is shown in Figure 5.29, which again compares well to the literature,[134] and the RESP charges generated are shown in Figure 5.30. The Lennard-Jones parameters used to represent the nitro group were taken from the "general AMBER force field" (gaff) parameter set, which is provided as a continually updated force field suitable for constructing organic molecules and can be combined with other AMBER parameter sets. The parameters used are given in Table 5.8. The Lennard-Jones parameters for the rest

Atom	Atom Type	σ	ε	parameter set
Nitro group nitrogens	NO	1.8240	0.170	gaff.dat
Nitro group oxygens	ON	1.6612	0.210	gaff.dat

Table 5.8: Additional Lennard-Jones Parameters for 4-Nitrobenzo-15-Crown-5

of the atoms were assigned as for the benzocrown.

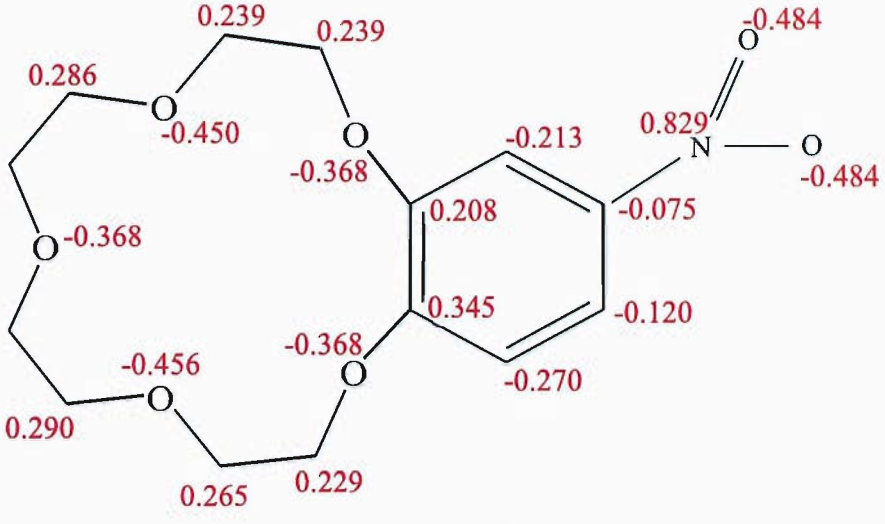

Figure 5.30: The RESP charges generated for 4-nitrobenzo-15-crown-5.

The surface tension results measured on 4-nitrobenzo-15-crown-5 were very similar to those of the benzo-15-crown-5, and so the same range of concentrations were studied in the simulations. The relationship to the experimental bulk concentrations may be seen in Figure 5.31, in which, the circles highlight the simulated systems.

5.2.6 Results and Discussion

As for the previous system, a bulk system was set up with one 4-nitrobenzo-15-crown-5 molecule in Box 3 (sides of 45 Å). This was to enable comparison of the conformations seen in bulk and at the interface.

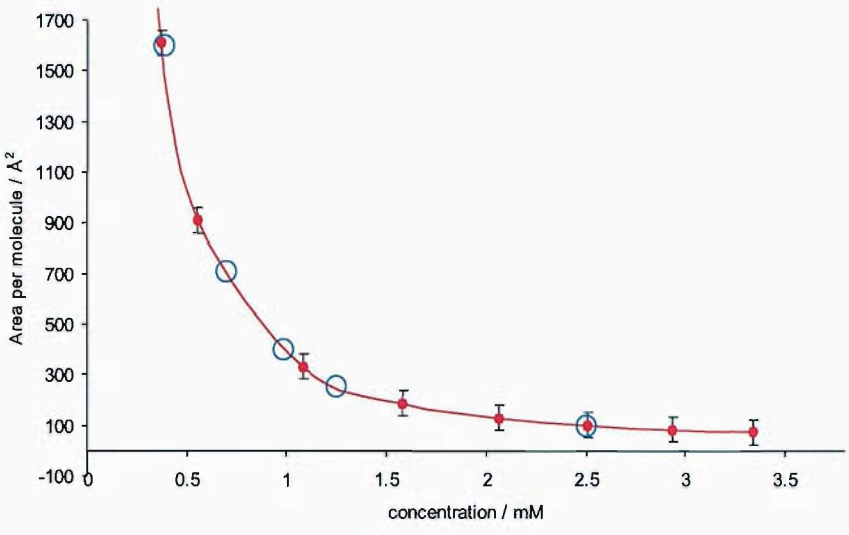

Figure 5.31: The area per molecule calculated from the surface tension measurements for 4-nitrobenzo-15-crown-5. The circles indicate the points which have been used as the initial set up for the interfacial simulations. Simulations were also carried out for an infinitely dilute surface (1 crown on the interface), and for a near saturated interface (100 crowns on the interface).

5.2.7 4-Nitrobenzo-15-crown-5 Behaviour in Bulk Solution

As for the benzo system, the planes within the molecule (as illustrated in Figure 5.7) were investigated to determine preferred conformations, and the distribution of the angle between the planes in the crown ether ring and the benzene ring are shown in Figure 5.32, whilst the distribution of the angles between the planes within the crown ether part are shown in Figure 5.33. It appears that very similar molecular conformations are adopted by the nitrocrown as seen for the benzocrown, except that the bent structure (with an angle of approximately 115° between the normals of the planes) only seems to be formed in one direction. There is no obvious reason for this, especially in bulk, although it is possible that somehow the nitro group stabilises the bent conformation once it occurs, such that the crown does not flip between the bent and straight conformations so readily.

As for the benzo-15-crown-5, the planes within the crown ether appear to remain reasonably flat throughout the simulations.

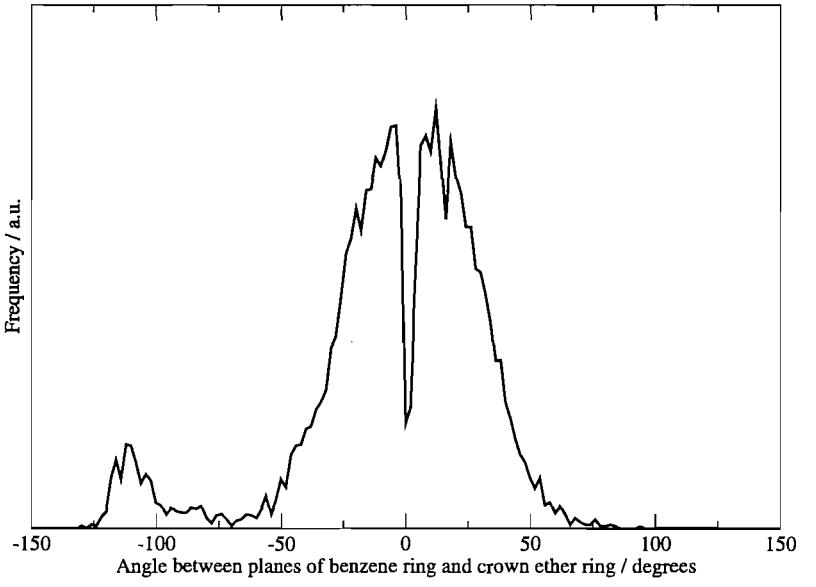

Figure 5.32: Distribution of the angle between the planes of the benzene ring and the crown ether ring for a single nitrocrown molecule in bulk solution.

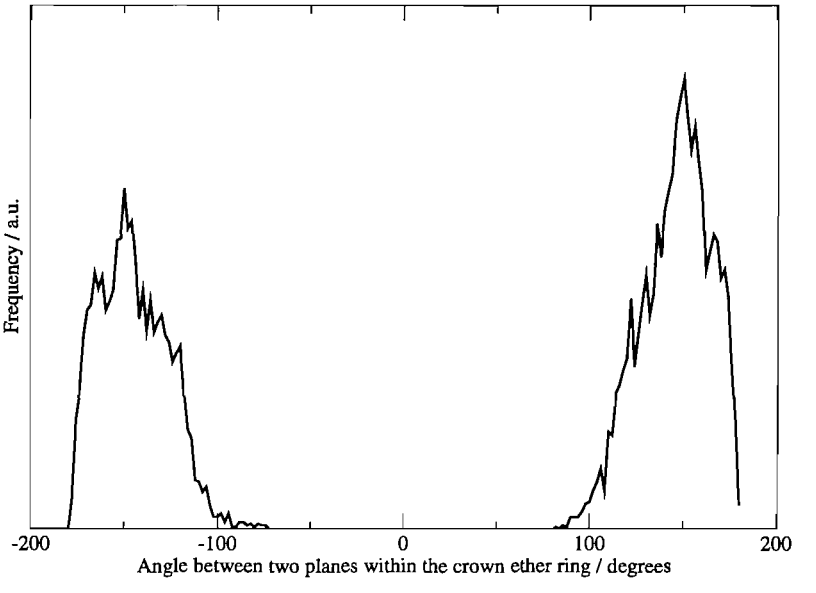

Figure 5.33: Distribution of the angle between the planes within the crown ether ring for a single nitrocrown molecule in bulk solution. These indicate no puckering or distortion of the ring occurs.

5.2.8 4-Nitrobenzo-15-crown-5 at the Water/Air Interface

The simulations set up are shown in Table 5.9. Only two simulations were carried out under two initial configurations in this case, and those were N_s=4 and N_s=25. As for the benzocrown, the simulation is labelled according to the number of crowns on the interface, N_s, and the starting configuration of the crowns, with I indicating a grid of molecules parallel to the interface, and II indicating a grid of molecules perpendicular to the interface.

Simulation Label	N_s	Starting Configuration	Area Occupied per Crown / Å^2	Bulk Concentration represented / M
1I	1	Flat	6400	Infinite Dilution
4I	4	Flat	1600	< 0.0005
4II	4	Upright	1600	< 0.0005
9I	9	Flat	710	0.0007
16II	16	Upright	400	0.0010
25I	25	Flat	256	0.0013
25II	25	Upright	256	0.0013
64II	64	Upright	100	0.0025
100II	100	Upright	64	0.005+

Table 5.9: The simulations run on 4-nitrobenzo-15-crown-5, including the configuration of the molecules, the area occupied per molecule, and the bulk concentration represented at the start of the simulations.

Interfacial conformations

The compound shows the same conformational distribution at the interface as it does in bulk solution, with a proportion of the molecules being in a bent shape, the angle between the planes being $\pm 100^{o}$, but the preference being a relatively flat conformation. Within this bent conformation, the angle made between the normals to the planes is wider than that for the benzo-15-crown-5: that is, the molecule is more bent than the benzocrown.

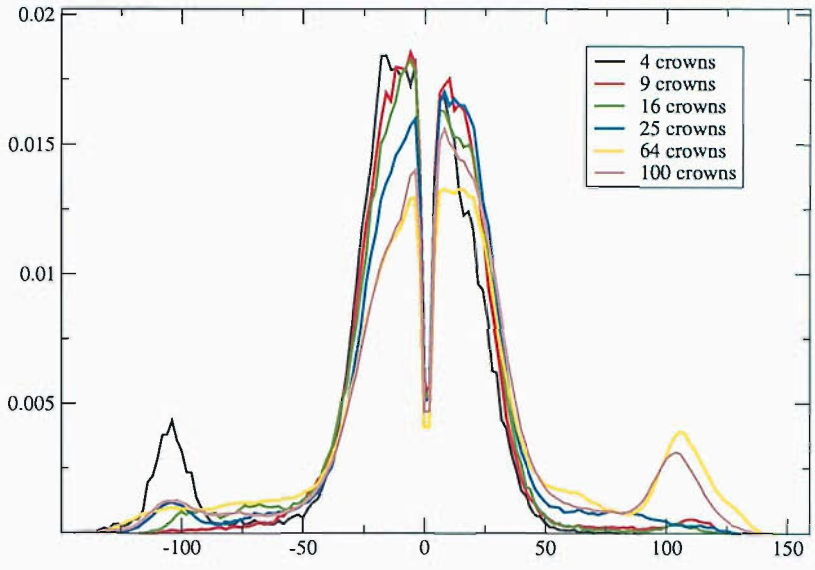

Figure 5.34: Distribution of the Angle between the planes of the benzene ring and the crown ether ring for several surface concentrations.

Interfacial Order Parameters

The way in which the 4-nitrobenzo-15-crown-5 behaves at the interface is studied based upon the axes sets shown in Section 3.3. The parameters derived from the simulations are presented in Table 5.10 and plots of the average computationally derived tilt angle for each system and the order parameters are presented in Figures 5.35.

Simulation	Bulk Conc Represented / M	$\langle P_1 \rangle$	$\langle P_2 \rangle$	$\langle P_3 \rangle$	$\theta_{sim}/^{o}$
1I	infinite dilution	-0.1742(0.025)	-0.2549(0.003)	-0.0304	101.2(1.4)
4I	< 0.0005	-0.1932(0.077)	-0.0184(0.041)	0.0099	104.5(6.7)
4II	0.0007	-0.3185(0.028)	-0.0444(0.030)	0.0240	126.8(7.3)
9I	0.0007	-0.2980(0.022)	0.0158(0.090)	-0.0053	112.5(4.1)
16II	0.0010	-0.3656(0.025)	0.1638(0.059)	-0.0804	105.8(12.8)
25I	0.00125	-0.3035(0.09)	0.1047(0.036)	-0.0359	111.4(4.2)
25II	0.00125	-0.2874(0.045)	0.0314(0.021)	-0.0283	111.6(2.7)
64II	0.0025	-0.1458(0.039)	0.0450(0.047)	-0.0169	103.5(1.4)
100II	>0.005	-0.1181(0.008)	0.0156(0.017)	-0.0012	99.5(1.8)

Table 5.10: Parameters derived from 10 ns of MD on each 4-nitrobenzo-15-crown-5 system.

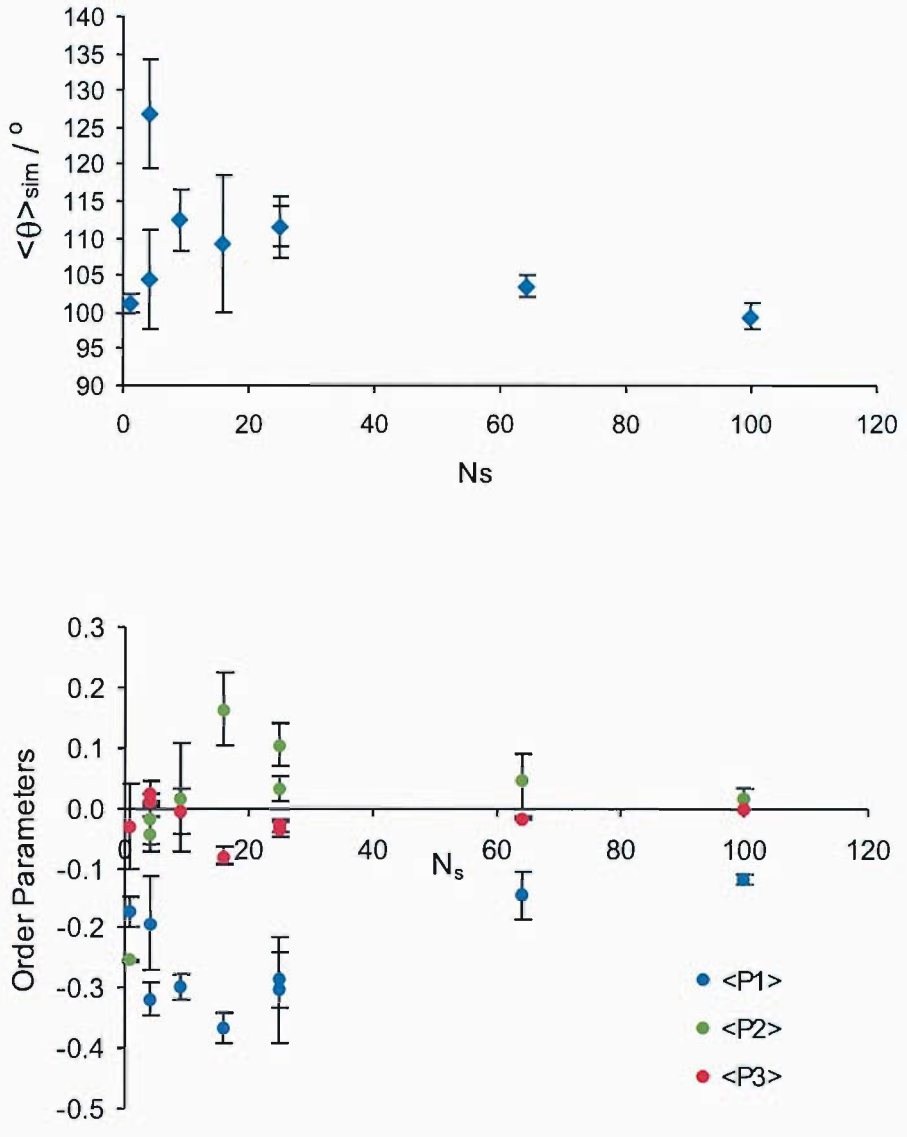

Figure 5.35: Plots of the tilt angle and order parameters obtained for the 4-nitrobenzo-15-crown-5 systems through molecular dynamics. There is a preference indicated in the plots for a tilt angle of greater than 90°. As for the benzocrown, the errors on the points are the standard error over the two interfaces for each system.

4-nitrobenzo-15-crown-5 shows a preferred tilt angle between 99.5 and 126.8°. The distributions of the tilt angle at each concentration are presented in Figure 5.36. Again, to show geometrically that the orientation of the molecules is not random, the distributions of the cosine are also presented (Figure 5.37).

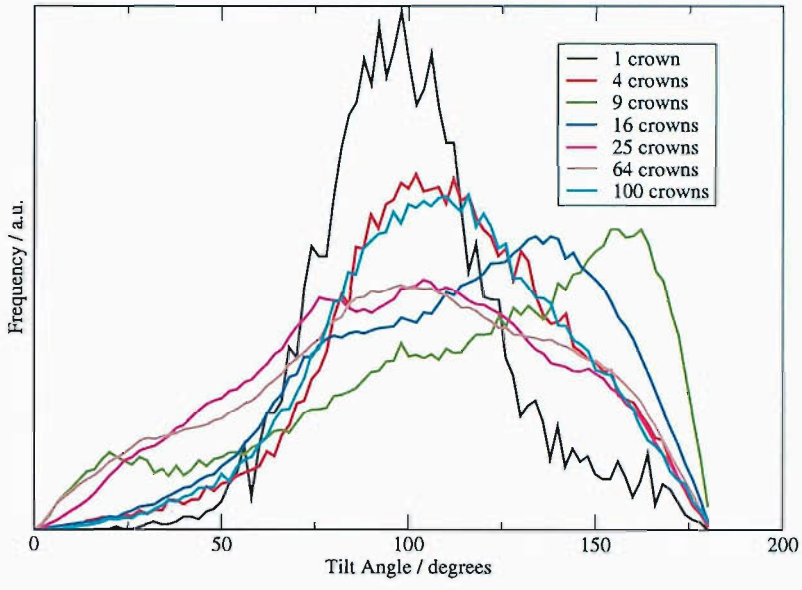

Figure 5.36: The distribution of the tilt angle θ, describing the tilt of the molecule with respect to the surface normal, for all concentrations. The total area of all plots is normalised.

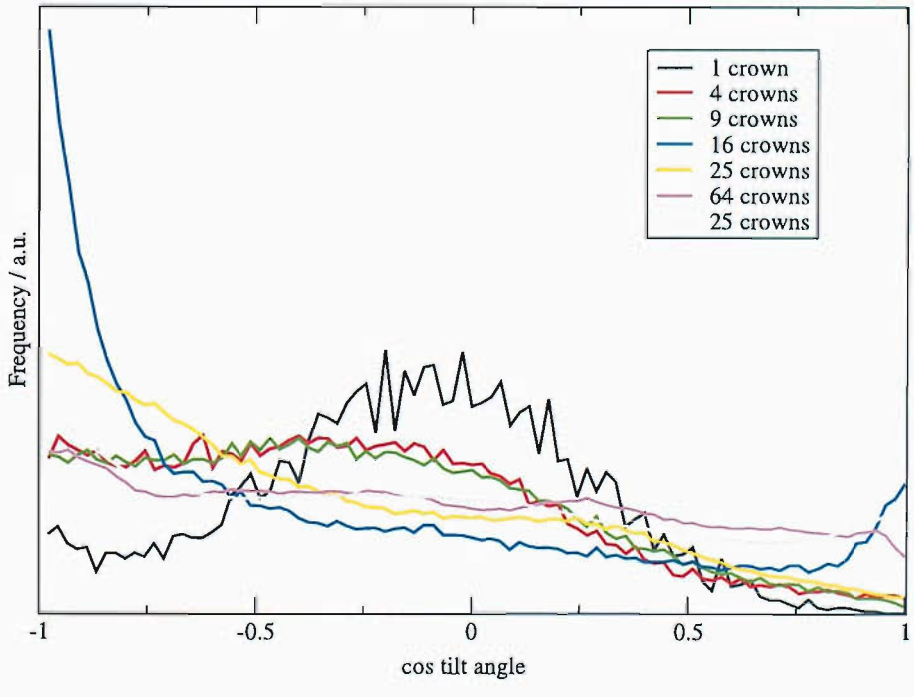

Figure 5.37: The distribution of P_1 for all concentrations. The total area of all plots is normalised.

From Figure 5.38, the Euler angle of rotation about the molecular axis, ψ, is not uniformly distributed in this system. Interestingly, for a single nitrocrown at the interface (at a very low surface concentration), the preferred orientation is $\psi = 180^{o}$. This implies that the crown will lie flat to the interface. However, at higher concentrations, the preferred orientation of the nitrocrowns is very clearly $\psi = 90^{o}$ or 270^{o}, which means that the crown will be lying on its side at the interface. There is still evidence of a significant proportion of the interfacial crowns lying flat relative to the interface, but with increasing concentration, this becomes less and less significant. At the mid-range of concentration, for those crowns which are lying on their side ($\psi = 90^{o}$ or 270^{o}), there is no preference for the nitro group to be in or out of the water. It is possible that this is due to some preferred method of stacking. At the highest concentrations, the crowns show an increased preference to be orientated with the nitro group in the water, seen by the larger peaks at 270^{o} as compared to those at 90^{o} in Figure 5.38. A schematic diagram of this orientation is shown in Figure 5.39.

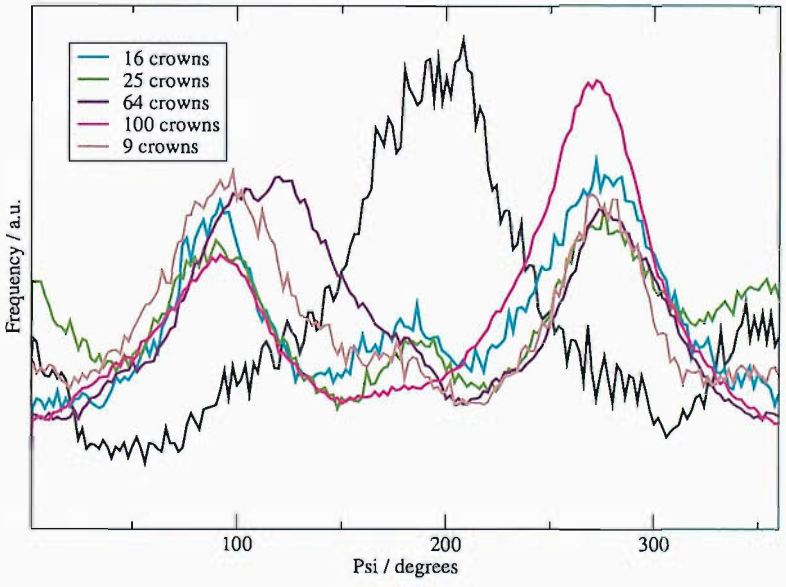

Figure 5.38: The distribution of the Euler angle ψ , describing the rotation of the molecule around the molecular axis.

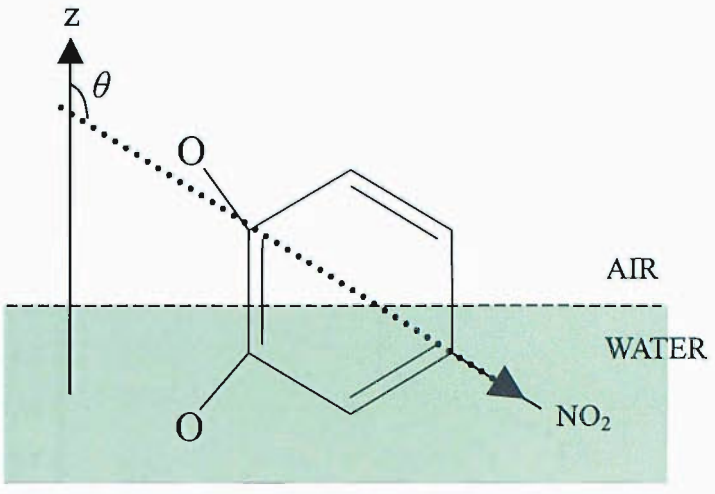

Figure 5.39: Combining the information on the values of θ and ψ, 4-nitrobenzo-15-crown-5 appears to prefer to be nitro group down into the water, and for the chromophore to be perpendicular to the water surface.

Interfacial Refractive Index

The estimated interfacial refractive index is derived by examining the position of the chromophore with respect to the water profile, as for the benzocrown. The calculated n_{int} at each surface concentration is given in Table 5.11. For all but the highest concentration, this refractive index has a more water-like value than the estimated $0.5(n_{air}+n_{wat})$ used for the experimental analysis.

N_s	Dist from Dividing Surface / Å > 0 = vapour side < 0 = liquid side	$\langle n_{int} \rangle_{sim}$	Water-like or Air-like
1I	-0.60(3.5)	1.199(0.12)	water
4I	-3.05(0.6)	1.299(0.01)	water
4II	-2.9(0.0)	1.273(0.02)	water
9I	-3.50(0.2)	1.280(0.02)	water
16II	-3.75(0.5)	1.288(0.01)	water
25I	-3.2(0.0)	1.273(0.01)	water
25II	-3.15(0.3)	1.271(0.01)	water
64II	-1.55(0.15)	1.208(0.03)	water
100II	2.5(1.2)	1.100(0.01)	air

Table 5.11: Interfacial refractive index for the 4-nitrobenzo-15-crown-5 system estimated from the simulations.

The refractive index of the interface is plotted against the number of crowns in the system (Figure 5.40).

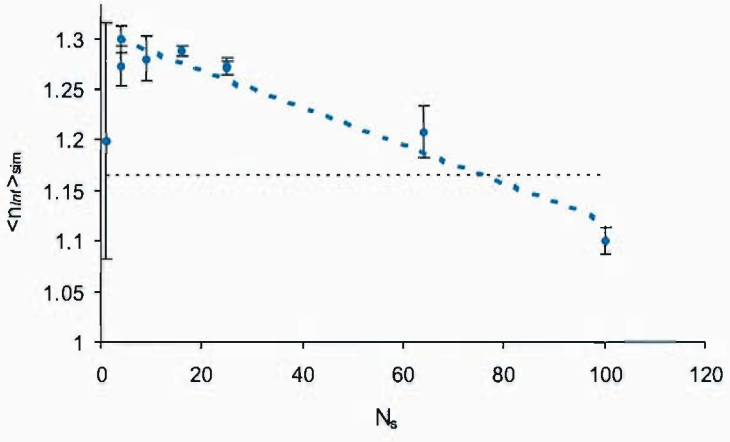

Figure 5.40: Plot of the interfacial refractive index with concentration as derived from MD.

As with the benzo-15-crown-5, the molecules at higher values of N_s are less submerged than at low N_s. The nitrocrown chromophores are water-like for all but the highest concentration, whereas the benzocrowns were air-like at all concentrations.

Surface Tension

Once again, the surface tensions of the systems simulated, shown in Table 5.12, are of comparable value to the experimentally determined values. The fluctuations are large, as is expected, and the detail of the change in surface tension with surface concentration cannot be detected.

Inter-Crown Distance Correlation

As for the benzocrown, the correlation seen between the vertical vectors of molecules (that is, the vector which runs through the long axis of the molecule) is reported here. This vector is labelled $\underline{\mathbf{v}}$ in Figure 5.41.

Number of Crowns	$\langle\gamma\rangle_{sim}$
1I	57.1
4I	50.8
4II	58.4
9I	58.6
16II	57.7
25I	58.4
25II	57.9
64II	59.4
100II	64.0

Table 5.12: The surface tension calculated for each 4-nitrobenzo-15-crown-5 system.

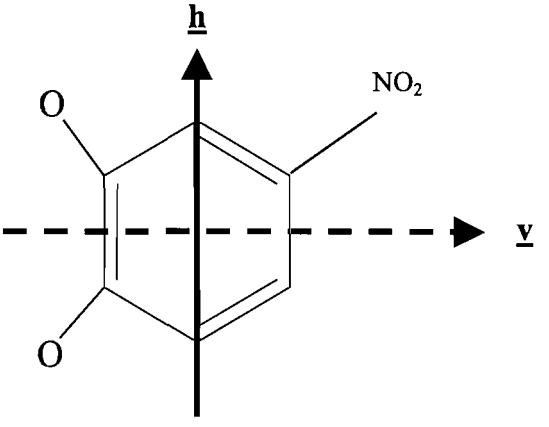

Figure 5.41: The vectors used in the correlation analysis for 4-nitrobenzo-15-crown-5 (Only the chromophore of the molecule is shown here).

The radial distributions are again illustrated for several systems in Figure 5.42. The 4-nitrobenzo-15-crown-5 molecules appear to pack very tightly, and evidence of up to 3 shells is seen for N_s = 16 and upwards. It is seen that a strong peak occurs at 3.9 Å, and comparison to the correlation plots in Figures 5.43 to 5.45 shows that this peak which corresponds to head to head packing. The most common inter-crown configurations appear to be those where the nitrobenzo groups are aligned, be it with both nitro groups up, or one up and one down.

The analyses carried out on the nitrocrown has been extended slightly over those carried out on the benzo system. Since the nitrocrown molecule is not symmetrical, a horizontal correlation has been measured as well as a vertical corre-

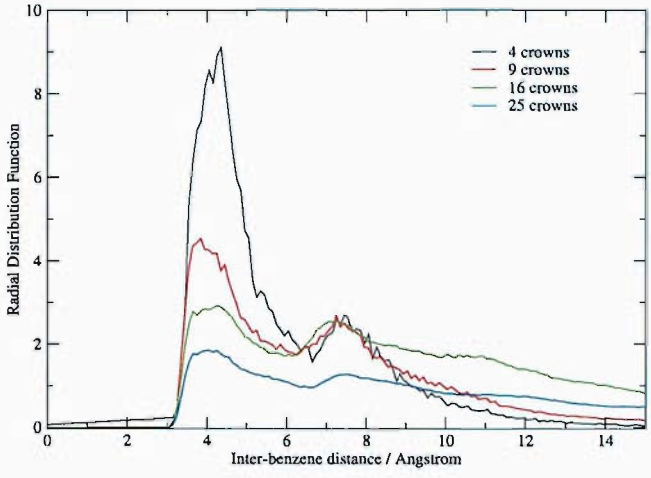

Figure 5.42: The radial distribution plot showing an initial peak at about 3.9 Å. A further shell is seen at about 7.5 Å. Note that the radial distribution function does not quite tend to 1 in bulk, especially at low concentrations, due to the limited number of crowns present in the systems.

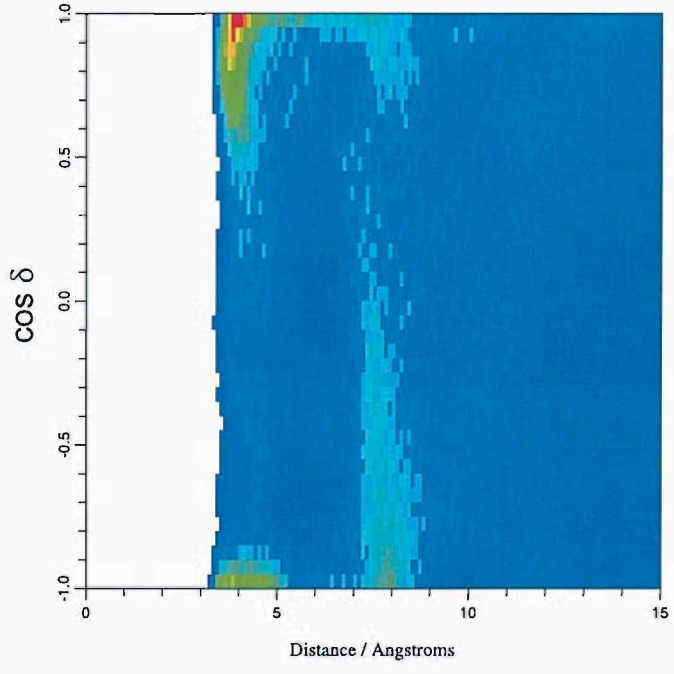

Figure 5.43: Correlation plot relating the vertical vectors of neighbouring 4-nitrobenzo-15-crown-5 molecules for one interface from the 25II simulation (25 nitrocrown molecules).δ is the angle between the $\underline{\mathbf{v}}$ vectors of neighbouring crowns.

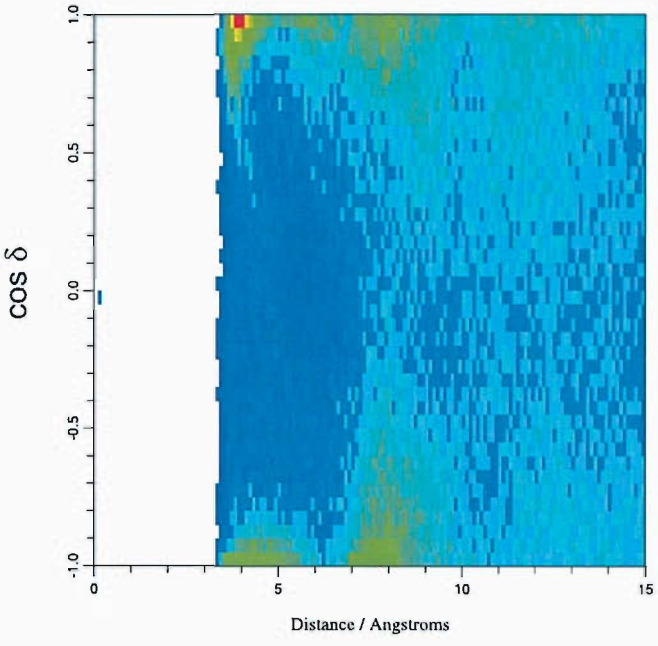

Figure 5.44: Correlation plot (vertical) for the 64 nitrocrown simulation (single interface). There is significant population of both correlated and anti-correlated crown packing at 7.5 Å at this concentration in addition to the peaks at 3.9 Å.

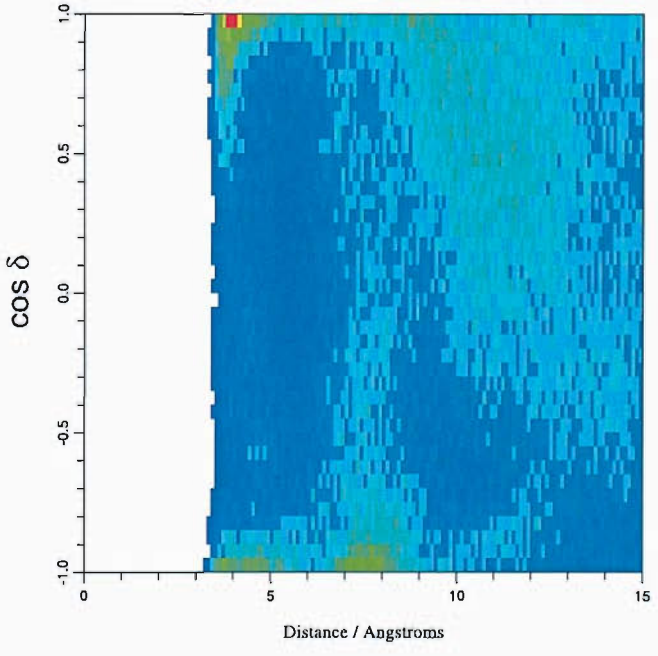

Figure 5.45: Correlation plot for the vertical vectors for the 100 nitrocrown simulation (single interface). There are clearly two shells of oriented crown ethers at this interface.

lation. The vector used in this analysis is represented as $\underline{\mathbf{h}}$ in Figure 5.41. The possible configurations leading to the observed cosine of a vector pair, denoted η, are illustrated in Figure 5.46.

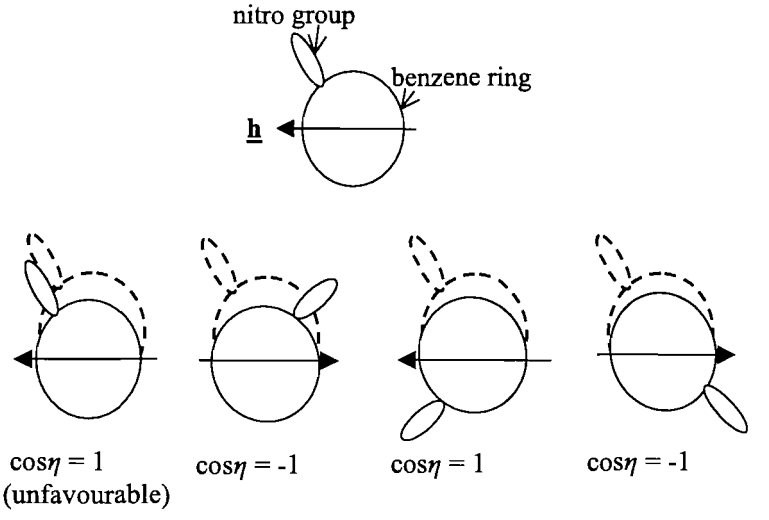

Figure 5.46: Possible orientations of nitrocrown headgroup and the values of cos η which would arise from them.

The molecules pack in a structured way. The peaks arising from the shells of molecules are very well-defined, seen in Figures 5.47 and 5.48.

From investigating the systems using a radial distribution function and inter-crown orientations (how the orientation of one crown affects that of a neighbouring crown), it is apparent that there is a high level of order within the nitrocrown systems.

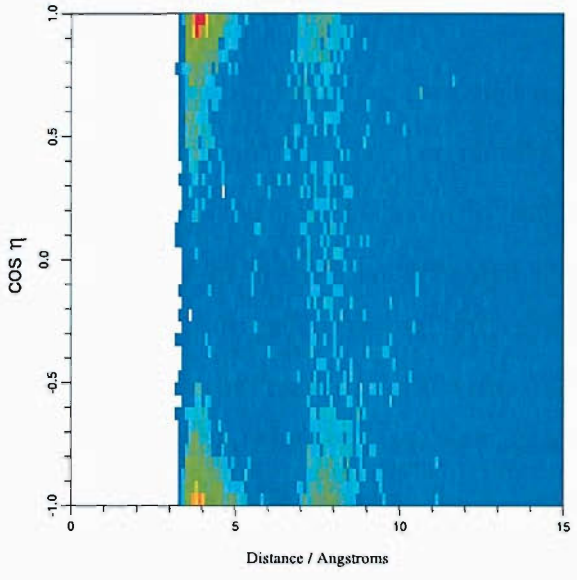

Figure 5.47: Correlation of the horizontal vectors of the nitrocrown for one interface of a 25 nitrocrown simulation, where η represents the angle between the **h** vectors of two neighbouring crowns.

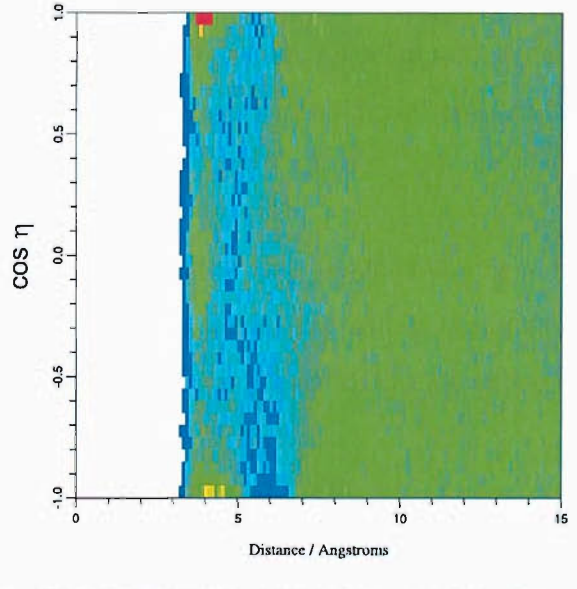

Figure 5.48: Correlation of the horizontal vectors for one interface only of the 64 nitrocrown simulation.

Summary of MD Results

The interfacial behaviour of benzo-15-crown-5 and 4-nitrobenzo-15-crown-5 have been studied over a concentration range determined by the experimental surface tension measurements on each system. Analyses were carried out to look at the interfacial conformations of the crowns. These were compared to the conformations seen in a dilute, bulk simulation, and no significant difference was seen for either crown. The order parameters and Euler angles were then studied to provide a direct link back to the second harmonic generation experiments. The interfacial configurations of the benzo and the nitrobenzo crowns were quite different, but both showed non-random tilt angles. The benzo-15-crown-5 molecules exhibited strong hydrophobicity, with the tendency at the interface for the chromophore centre to be in the vapour region. Conversely, the nitro compound showed preference for the chromophore centre to be submerged in the water, except at the highest surface concentration. The inter-crown stacking for the benzo compound showed the "head to head" configuration to be favoured, with very little anti-correlation of the vertical vectors of neighbouring crowns. This is likely to be due to the hydrophobicity of the molecule. The nitro crown showed a preference to be positively correlated with respect to the vertical vectors, but there was also significant anti-correlation apparent at the same distance. Both systems produced defined radial distribution functions. For the nitrocrown, correlation between the horizontal vectors of neighbours was also investigated, and again, both anti-correlation and correlation were observed.

In summary, these two systems show significant ordering at the interface. In the next part of the thesis, the analysis carried out and its implications for the SHG analysis are set out. An evaluation of the use of MD to aid experimental interpretation is presented.

Part III

Comparison and Evaluation

Chapter 6

Using MD to Improve SHG Analysis

Second harmonic generation is a very valuable spectroscopic tool, being one of very few techniques which allows the surface specific study of interfaces such as the liquid-vapour interface. The interpretation of SHG results does rely heavily on several assumptions, some of which are intuitive (such as the assumed random nature of the azimuthal angle on a liquid surface), but others of which require some knowledge of the system. One of the aims of this project has been to determine how molecular dynamics simulations may aid the interpretation of SHG results. In doing this, caution must be exercised, as the simulations themselves are all based upon models, with their own assumptions underlying the results obtained. However, if the results obtained from experiment and simulation are consistent with each other, the description of a system may be expanded with some confidence.

In this chapter, the assumptions used at various stages throughout the analysis of SHG data are considered, and the way in which molecular dynamics may be used to help validate assumptions is discussed with reference to the work carried out in this project.

6.1 The Assumptions Underlying SHG Analysis

To derive the components of the surface (or second order) susceptibility tensor, $\chi^{(2)}$ from polarisation data through the ABC method, the interfacial refractive index, n_{int}, must be estimated. There is no reliable way of measuring this experimentally for many systems,[23] and so this may limit the reliability of absolute χ determinations. This index may be estimated if it is found that the SHG data lie in the weak limit.[24]

The orientation parameter obtained through SHG measurements is D. It is essential to consider that the usefulness of the orientation parameter D of a system in an absolute sense depends upon the validity of the assumptions that:[5,27]

- The interfacial refractive index, n_{int}, is correctly estimated.
- There is azimuthal symmetry at the surface. That is, that ϕ is uniformly distributed.
- The angle ψ is estimated correctly
- The symmetry of the adsorbate at the interface is the same as that of the free molecule.
- The molecule is resonantly enhanced such that only 1 or 2 hyperpolarisability components are dominant.

Clearly, the likelihood that all of these assumptions hold for many systems except very simple ones is small, and therefore, measurements of D are more useful in a relative sense - that is, as a function of surface coverage or bulk concentration. The final assumption that D may be used to determine an accurate value of θ will hold only for very well defined surfaces.

In order to apply the DRF method of analysis on an SHG dataset, further assumptions are also necessary, and these are that:

- Those hyperpolarisability tensor components which are dominant are known at the outset of analysis.

- The distributions of the angles ψ and θ are independent.

These assumptions, and how they have been addressed with the simulations, are discussed in turn in the following sections, with reference to the two crown ether systems studied here.

6.2 The Use of MD to Validate the Assumptions

6.2.1 Interfacial Refractive Index

The interfacial refractive index, n_{int}, is very difficult to measure experimentally, and tends to be assigned either the value of one of the bulk media refractive indices or the average value of the refractive indices of both media. In the case of the benzo system, the interfacial refractive index could actually be estimated from the polarisation data by assuming that the data lay in the weak limit. This was a reasonable assumption, gven the values obtained for the χ components and D, as discussed in Section 3.2. Treating the data in this way allowed a back-calculation of n_{int}.[24] This resulted in a more water-like interfacial refractive index, as opposed to the half-water, half-air adsorbate layer assumed initially. However, the weak limit is approached with increasing θ distribution width[30] . If the distribution is not entirely weak limit, then the interfacial refractive index could be different again. From the simulation, using the proportion of chromophore centres above and below the Gibbs dividing surface of the water slab,the water density at the point where the chromophore centres lie is used to calculate the refractive index. In the simulation of the benzo-15-crown-5 systems, this lead to the conclusion of a more air-like interfacial layer. It must be considered, however, that without bulk

molecule presence in the simulations, this calculation may be affected. Alternatively, it is possible that at higher concentrations, it is in fact the crown presence at the interface which most affects the interfacial refractive index. Further simulations with a greater concentration of molecules on and near the surface might be able to clarify the situation with the refractive index. For the nitrocrown system, it is impossible to estimate the interfacial refractive index in the same way from the polarisation data. From the simulations, a significantly water-like refractive index is obtained.

6.2.2 Euler Angles

From simulations of adequate length, the distribution of all three Euler angles may be readily studied. These can be directly calculated from the trajectories for each frame of the simulation. This time evolving, atomistic detail is clearly of great use for direct comparison to the second harmonic generation experiments.

The Distribution of ϕ

The assumption that ϕ is random is validated by the simulations, and a low concentration benzo-15-crown-5 simulation (4 crowns at the interface) shows a random ϕ distribution (Figure 6.1).

However, the way in which the simulation cell was set up for the simulations means that the systems may take some time before ϕ does in fact become random, especially at high concentrations when the molecules are very close to each other and in identical configurations. For example, in Figure 6.2, the distributions for two parts (the first 2 ns and the last 2 ns) of the simulation and for the whole simulation are shown for the benzo-15-crown-5 system for which N_s = 64. The distribution from the entire 10 ns is not entirely random, but if the distribution of ϕ within the first 2 ns is taken, the distribution clearly shows deviation from random behaviour. Looking at the final 2 ns distribution, it is seen to have become much more random. This is an issue of equilibration, and the initial setup of the simulation, and supports the argument for long timescales in interfacial simulations.

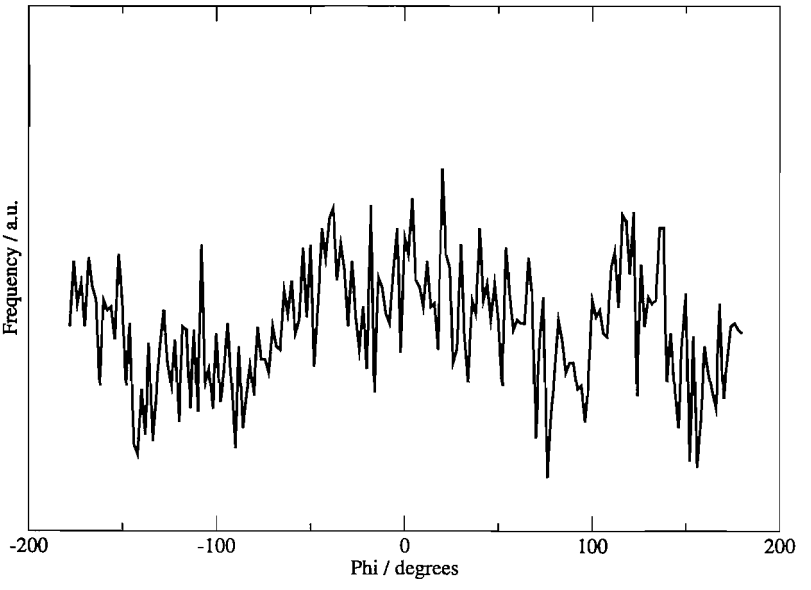

Figure 6.1: The distribution of the Euler angle ϕ throughout the benzo-15-crown-5 simulation where N_S =4. This distribution supports the assumption taken in the experimental analysis that ϕ is random.

A similar breakdown of the distribution of ϕ for the system containing 64 4-nitrobenzo-15-crown-5 molecules is presented in Figure 6.3. The distribution of ϕ only really becomes random in the last 2 ns or so of the simulation.

For the ϕ angle, it is intuitively reasonable to assume a uniform distribution when studying adsorbate molecules at a liquid interface. The ϕ distribution for the systems in this work is indeed uniform, or random. Care must be taken when interpreting simulation data on this parameter, as timescale will play an important role in the randomness of the angles. If the simulation is started from an ordered system, as in this work, then sufficient time must be allowed for the molecules to move away from this artificial order before the distribution may be studied. This is the reason for the long equilibration phase (0.5 ns) of the simulations in this work, as well as the long production runs (10 ns).

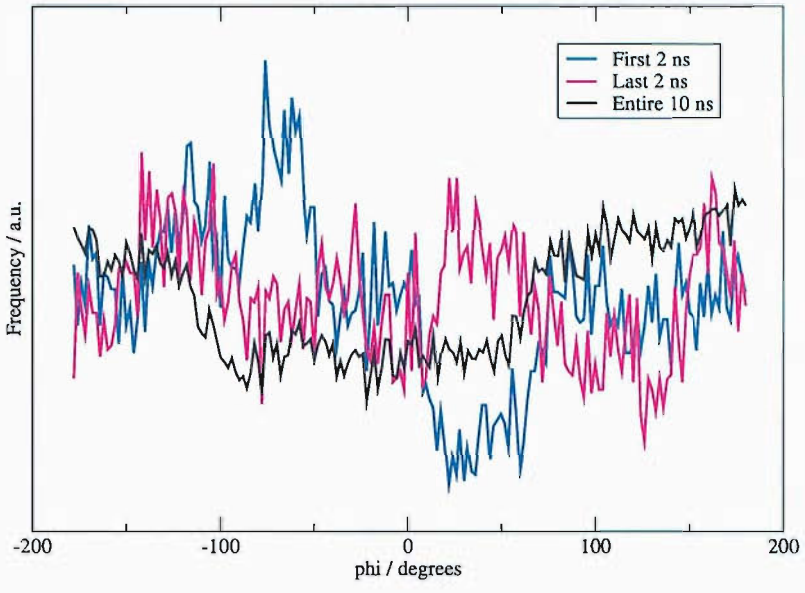

Figure 6.2: The distribution of ϕ over the first 2 ns period of simulation, the last 2 ns period, and over the entire 10 ns. The random nature of ϕ is apparent, but more notably so later on in the simulation run.

The Distribution of ψ

The ψ angle distribution will be dependent on the interaction of the adsorbate with the substrate. Thus, it may be estimated with some degree of confidence if this interaction is straightforward. Generally, the angle is estimated at either 0 or 90^{o}. The benzo-15-crown-5 system studied here shows a preference for the benzene ring to lie parallel to the interface, whilst the 4-nitrobenzo-15-crown-5 nitro-benzene group shows a propensity to sit at 90^{o} to the interface.

The Distribution of θ

The value of θ, the tilt angle of the long axis of the molecule with respect to the surface normal, is very often reported as the final result of an SHG study, and for those systems where the interfacial orientation of the molecules is strongly defined, SHG is of great value for deriving the angle. For other systems where the tilt angle may not be obtained absolutely, the technique will clearly indicate whether the order increases with concentration, or addition of new species into a

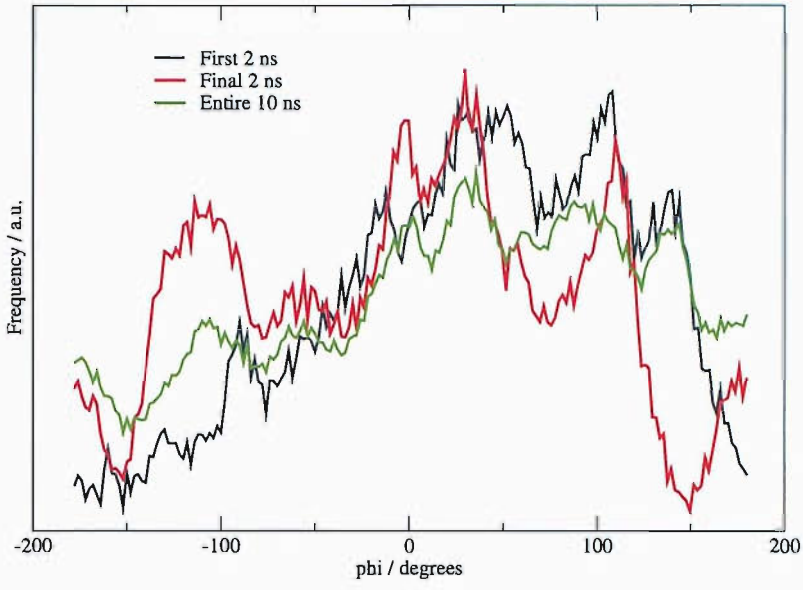

Figure 6.3: The distribution of ϕ over the first 2 ns period of simulation, the last 2 ns period, and over the whole 10 ns. The random distribution expected of ϕ is not clear in the early stages of the simulation, and is only really beginning to become apparent in the last few nanoseconds.

system. The parameter D may be expressed in terms of the order parameters $\langle P_1 \rangle$ and $\langle P_3 \rangle$ (Equation 6.1).

$$D = \frac{\frac{2}{5}\langle P_3 \rangle + \frac{3}{5}\langle P_1 \rangle}{\langle P_1 \rangle} = \frac{\langle \cos\theta^3 \rangle}{\langle \cos\theta \rangle} \tag{6.1}$$

For a sharply peaked, unimodal distribution of tilt angles, this parameter may be approximated to $D = \cos^2\langle\theta\rangle$, and from this, θ can be calculated.

In the systems studied in this work, the distribution of θ is found to be fairly broad. The true value of θ can therefore not be obtained directly from the SHG measurements, and this corresponds to the conclusions derived from the experimental work. However, it is possible to compare the trend in θ_{app} with concentration which would be expected from the simulations and that obtained from the experiments. Each term within expression 6.1 may be taken directly from the simulation. Thus, D may be calculated, and θ_{app}, which is the estimated tilt angle from a second harmonic polarisation experiment, can be obtained, and compared

to the value seen in the experiment. Table 6.1 shows the values of $\langle\theta\rangle_{sim}$, the true mean of the tilt angle distribution obtained through the MD simulations, D_{calc}, the D parameter derived using the order parameters $\langle P_1\rangle$ and $\langle P_3\rangle$ taken directly from the simulation, and θ_{calc}, the tilt angle derived from D_{calc} taking the assumption that $D = \cos^2\theta$.

Number of Crowns	$\langle\theta\rangle_{sim}$ / °	D_{calc}	$\langle\theta\rangle_{calc}$ / °	Bulk Concentration represented / mM
1	72.3(2.0)	0.4483	47.9	infinite dilution
4I	68.3(3.0)	0.5029	44.8	< 0.5
4II	70.0(1.0)	0.5059	44.7	< 0.5
9	65.3(2.7)	0.5312	43.2	0.7
9II	63.0(0.4)	0.5677	41.1	0.7
25I	59.5(1.4)	0.6184	38.2	1.4
25II	59.2(1.0)	0.6440	36.6	1.4
49	57.6(4.3)	0.6296	37.5	2.0
64	59.4(3.3)	0.6699	35.1	2.5
100	56.3(7.8)	0.6350	35.0	3.5

Table 6.1: Parameters derived from 10 ns of MD on each benzo-15-crown-5 system (errors are the standard error over the two interfaces of the system). The comparison is based upon the experimentally determined bulk concentration.

This data is compared to the experimental SHG results in Figure 6.4. The "bulk concentration" assumed for the simulations is that from which the area per molecule was derived originally (through surface tension measurements) and used to set up the simulations. Since there were two slightly different samples of benzo-15-crown-5 used in the experimental section, these are plotted as separate datasets. Although the distributions of tilt angles are quite wide relative to the distributions which would lead to a true tilt angle through the SHG measurements, there is a promising correlation in the trend of D with concentration over the range studied which suggests that the computational and experimental systems are behaving very similarly.

The same comparison is carried out with the 4-nitrobenzo-15-crown-5 system. This has proven to be a more difficult system to analyse, due to the phase which

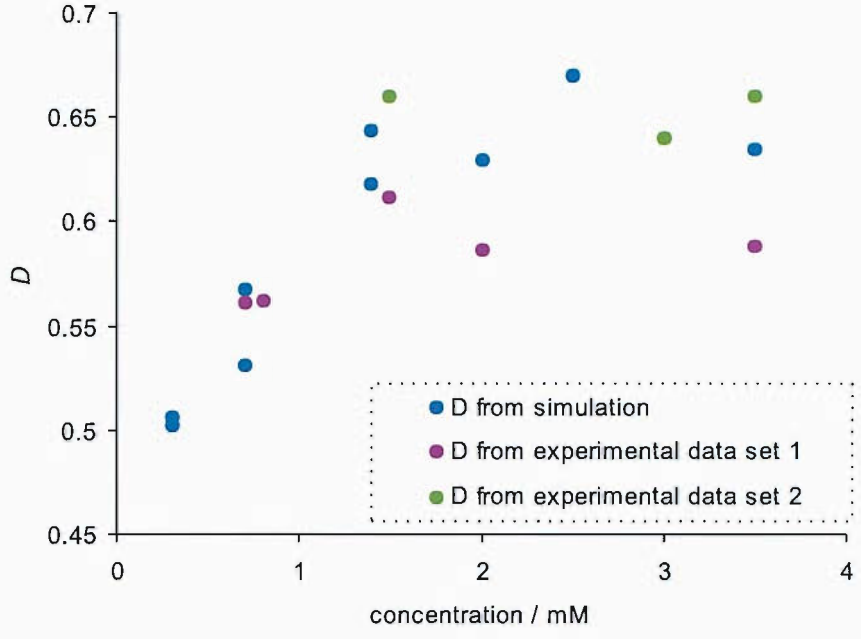

Figure 6.4: Plot of the order parameter D obtained from 2 samples using SHG and from the MD simulations. The trend in all three sets of data is very similar, and indicates a good agreement between experiment and simulation.

exists between the SHG electric fields for water and nitrocrown. The experimental data was treated to remove to water contribution from the data, but the assumption that the water surface is unchanged was taken in order for this treatment to be possible. The data shown in Figure 6.5 is that with the water contribution removed. The simulation data is given in table 6.2.2, and a plot of D obtained from both experiment and simulation is given in Figure 6.5.

For the nitrocrown, the concentration dependence of D derived from the simulations and from the experiments is not comparable, although the two sets do converge towards the same value. However, before any conclusions may be drawn about the consistency between experiment and simulation, the contribution of the water surface needs to be examined carefully.

Number of Crowns	$\langle\theta\rangle_{sim}$ / °	D_{calc}	$\langle\theta\rangle_{calc}$ / °	Bulk Concentration represented / mM
1I	101.2(1.4)	0.6472	35.9	infinite dilution
4I	104.5(6.7)	0.5746	40.7	<0.5
4II	126.8(7.3)	0.5674	41.1	<0.5
9II	112.5(4.1)	0.6034	39.0	0.7
16II	105.8(12.8)	0.6895	33.9	1.0
25I	111.4(4.2)	0.6448	36.6	1.25
25II	111.6(2.7)	0.6466	36.5	1.25
64II	103.5(1.4)	0.6383	37.0	2.5
100II	99.5(1.8)	0.6481	36.4	>5.0

Table 6.2: Parameters derived from 10 ns of MD on each 4-nitrobenzo-15-crown-5 system (errors are the standard error over the two interfaces of the system)

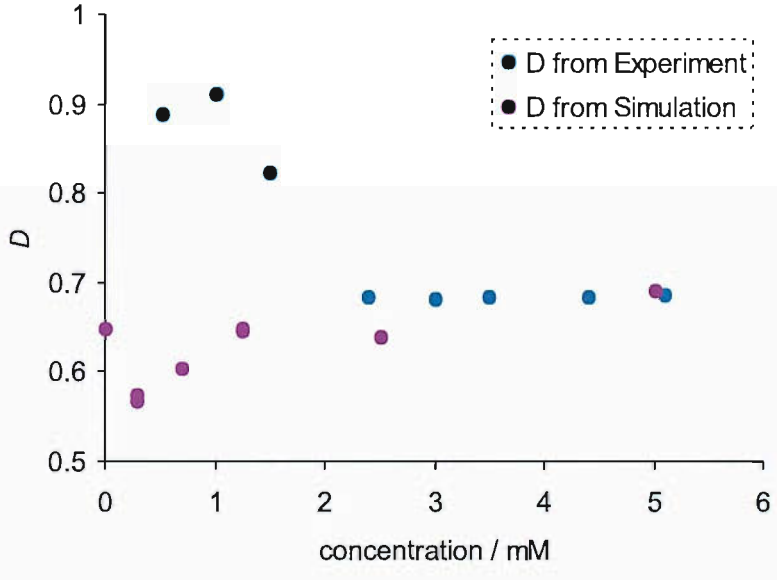

Figure 6.5: Plots of the order parameter D, obtained from the simulations, and from the experiments. The experimental data in this case has been treated to remove the water contribution.

6.2.3 Symmetry of the Adsorbate and Hyperpolarisability Components

The symmetry assumed for the free chromophore is derived from a flat chromophore in both cases here, which is realistic as the chromophores are small and rigid. For larger chromophores with some flexibility, however, such conformational analysis as presented in this work would provide an insight into the symme-

try that should be assigned to the system as an adsorbed species.

The hyperpolarisability assumptions in SHG experiments are now largely already dependent on *ab initio* determination. This partnership between experiment and theory is already well-established.[28,29,35]

6.2.4 The Independence of θ and ψ distributions

The use of the DRF method of analysing the polarisation data makes further assumptions on the Euler angles. The assumption that the ψ and θ angle distributions are independent allows the separation of the function $\langle cos\ \theta sin^2\theta sin^2\psi\rangle$ into the product $\langle cos\ \theta sin^2\theta\rangle\langle sin^2\psi\rangle$. If this does not hold - that is, if the average of the products does not equal the product of the averages - then the distributions of ψ and θ cannot be assumed independent.

Simulation	$\langle sin^2\theta cos\theta sin^2\psi\rangle$	$\langle sin^2\theta cos\theta\rangle$	$\langle sin^2\psi\rangle$	$\langle sin^2\theta cos\theta\rangle\langle sin^2\psi\rangle$
1I	0.0580(0.005)	0.152(0.013)	0.337(0.030)	0.0511(0.009)
4I	0.0728(0.011)	0.165(0.023)	0.409(0.010)	0.0674(0.008)
4II	0.0545(0.014)	0.159(0.024)	0.344(0.060)	0.0546(0.002)
9I	0.0831(0.010)	0.176(0.010)	0.471(0.020)	0.0827(0.009)
9II	0.0890(0.010)	0.175(0.016)	0.491(0.030)	0.0861(0.003)
25I	0.0897(0.010)	0.170(0.011)	0.528(0.010)	0.0898(0.005)
25II	0.0860(0.010)	0.159(0.010)	0.537(0.010)	0.0854(0.003)
49II	0.0982(0.010)	0.177(0.010)	0.550(0.020)	0.0879(0.006)
64II	0.0744(0.011)	0.132(0.040)	0.540(0.010)	0.0710(0.004)
100II	0.0748(0.020)	0.152(0.040)	0.521(0.020)	0.0789(0.030)

Table 6.3: Comparison of the values of $\langle sin^2\theta cos\theta sin^2\psi\rangle$ and $\langle sin^2\theta cos\theta\rangle\langle sin^2\psi\rangle$ for benzo-15-crown-5 over the concentration range. These values are assumed independent for the DRF method of fitting SHG data. If this is the case, then $\langle sin^2\theta cos\theta sin^2\psi\rangle = \langle sin^2\theta cos\theta\rangle\langle sin^2\psi\rangle$. The errors reported in parentheses are 2 standard deviations.

For benzo-15-crown-5, the difference between the product $\langle sin^2\psi\rangle\langle sin^2\theta cos\theta\rangle$ and the product $\langle sin^2\theta cos\theta sin^2\psi\rangle$ is very small, as seen in Figure 6.6. Looking at the values of the data for simulations starting from the same concentration, but

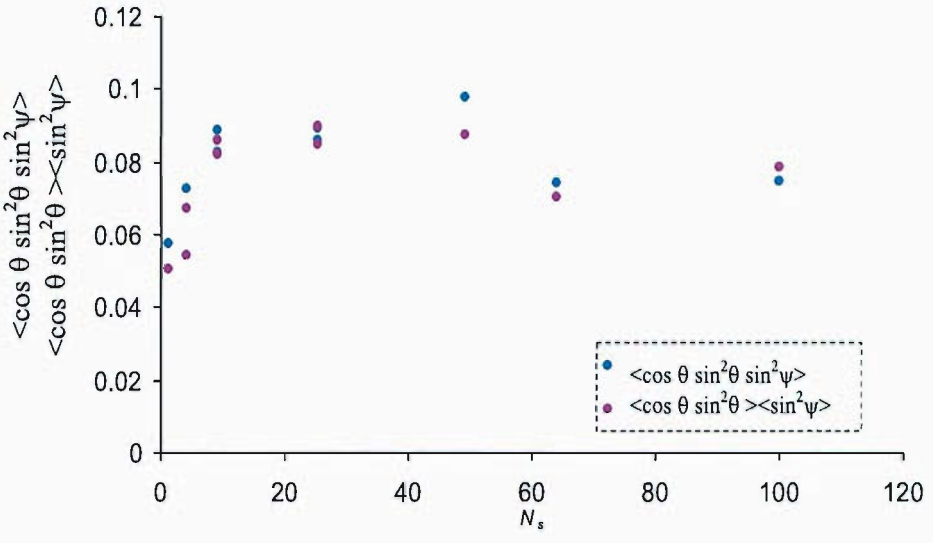

Figure 6.6: The functions $\langle sin^2\theta cos\theta sin^2\psi\rangle$ and $\langle sin^2\theta cos\theta\rangle\langle sin^2\psi\rangle$ plotted for benzo-15-crown-5. The very close agreement between the average of the products, and the product of the averages indicates that the angles θ and ψ are independent.

for two different starting configurations I and II, shown in Table 6.3, the pairs of data are very similar in value, again indicating that the simulations are well-equilibrated. It may be concluded that, for the benzo-15-crown-5 system, the distributions of θ and ψ are indeed independent, and thus, that the DRF method is a valid way of fitting the SHG data, since the contributing $\beta^{(2)}$ components are known.

Simulation	$\langle sin^2\theta cos\theta sin^2\psi\rangle$	$\langle sin^2\theta cos\theta\rangle$	$\langle sin^2\psi\rangle$	$\langle sin^2\theta cos\theta\rangle\langle sin^2\psi\rangle$
1I	-0.0279(0.004)	-0.0986(0.020)	0.264(0.002)	-0.026(0.007)
4I	-0.0514(0.006)	-0.102(0.010)	0.485(0.012)	-0.050(0.009)
4II	-0.0946(0.008)	-0.165(0.040)	0.545(0.040)	-0.090(0.020)
9I	-0.009(0.004)	-0.006(0.070)	0.659(0.050)	-0.004(0.010)
16II	-0.0093(0.003)	-0.0371(0.060)	0.632(0.030)	-0.023(0.003)
25I	-0.0440(0.008)	-0.0937(0.050)	0.593(0.020)	-0.056(0.031)
25II	-0.0412(0.006)	-0.112(0.030)	0.571(0.030)	-0.0636(0.014)
64II	-0.0316(0.005)	-0.051(0.020)	0.630(0.020)	-0.0320(0.008)
100II	-0.0322(0.01)	-0.0480(0.010)	0.612(0.010)	-0.0294(0.007)

Table 6.4: Comparison of the values of $\langle sin^2\theta cos\theta sin^2\psi\rangle$ and $\langle sin^2\theta cos\theta\rangle\langle sin^2\psi\rangle$ for 4-nitrobenzo-15-crown-5 over the concentration range. Errors (in parentheses) are reported as standard errors.

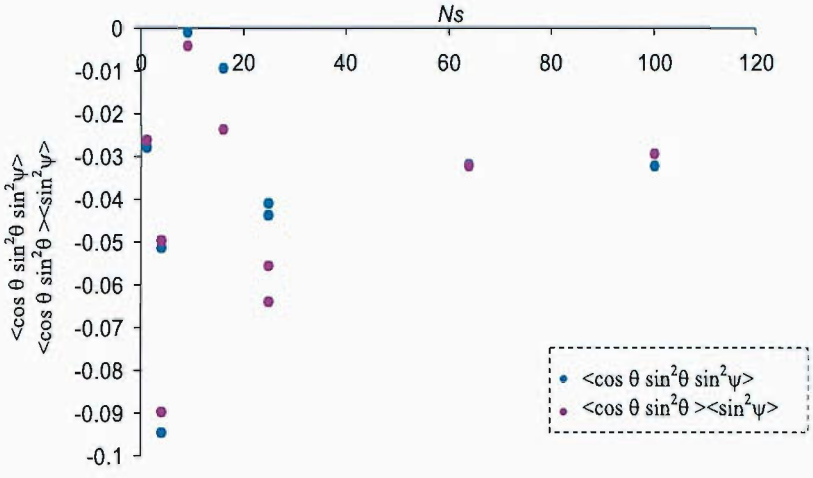

Figure 6.7: Comparison of the values of $\langle sin^2\theta cos\theta sin^2\psi \rangle$ and $\langle sin^2\theta cos\theta \rangle \langle sin^2\psi \rangle$ for 4-nitrobenzo-15-crown-5 over the concentration range. The values calculated for each product within each system are very close, which suggests that the angular distributions of ψ and θ are independent.

For the nitrocrown, the difference between the two products is quite pronounced for the 4 crown and 9 crown systems, although it converges more at higher concentrations. The trend in the two products with concentration is very close, however, and given that the scatter of the parameters is larger than is seen for benzo-15-crown-5, it is possible that the distributions of ψ and θ are still independent and therefore separable. The DRF fitting method was not applied to the nitrocrown in this work, due to the uncertainty in the significant hyperpolarisability components.

6.3 The Effect of an Adsorbate upon the Water Surface

If the water contribution is to be removed from a set of polarisation data as it was for 4-nitrobenzo-15-crown-5, then the assumption taken is that the water surface when the water is a substrate is behaving in the same way that it would as a pure water interface. It has been shown by several MD studies that this would not appear to be the case. In this study, the orientational profile of the pure water slab was presented in Section 5.1.

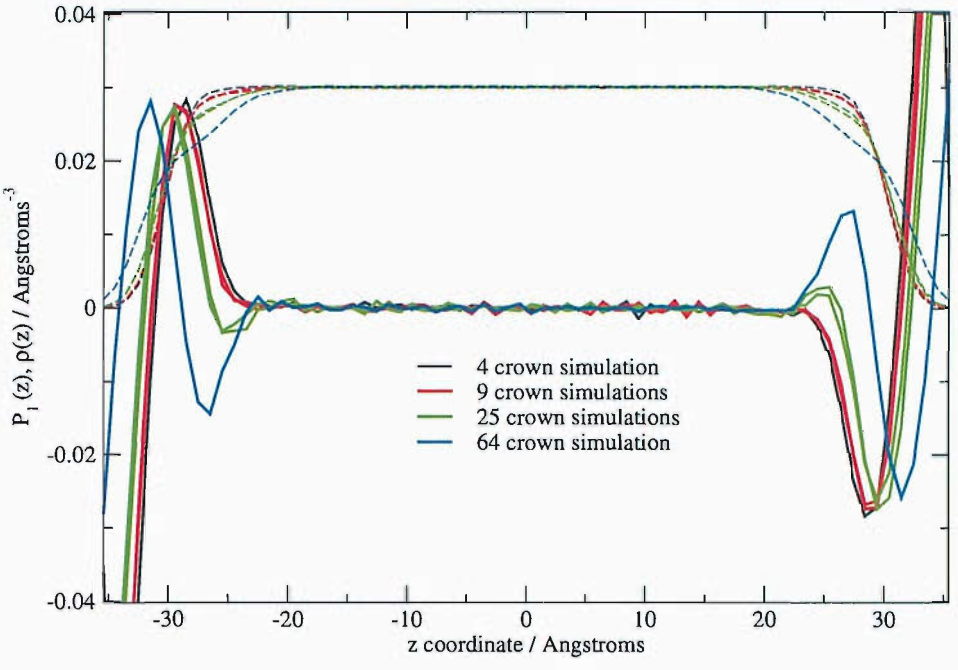

Figure 6.8: The orientational profile, showing $P_1(z)$ (solid, bold lines), of water for various benzo-15-crown-5 simulations. Both 9 crown simulations (9I and 9II) and both 25 crown simulations (25I and 25II) are shown on the plots in the same colour. The density profiles, $\rho(z)$, of water are also shown such that the position of the features in the orientation profiles can be seen in relation to the interfacial position (Gibbs dividing surface being located at ± 30 Å.

With the pure water orientational profile, two distinct regions of orientational behaviour could be seen: on the water side of the Gibbs' dividing surface, there was a peak where the average cosine of the dipole orientation was strongly negative (that is, the water dipole was pointing down towards the bulk water), and then on the vapour side of the surface, the dipole orientation flipped.

In the presence of benzo-15-crown-5 an additional feature develops with increasing concentration: somewhat deeper into the slab a second region is seen where the orientation of the water dipole is pointing up, towards the vapour region, followed by the layer of water molecules with their dipoles on average pointing back into the bulk water, and the outer layer, on the vapour side of the Gibbs' surface, which again has its dipole pointing into the bulk vapour region. This structure is apparent to some extent in the 25 crown simulations, but is very clear in the 64 crown simulation (see Figure 6.8). Thus, not only is the water interfacial structure different in the presence of crowns, but it is also differs with concentration of

crowns.

For the nitrocrown system, the orientational profile of the water slab is also different from that of the pure water interface, which develops clear structure as the surface concentration of the nitrocrown is increased, shown in Figure 6.9. It is significantly different to that of the benzo-15-crown-5 system as well.

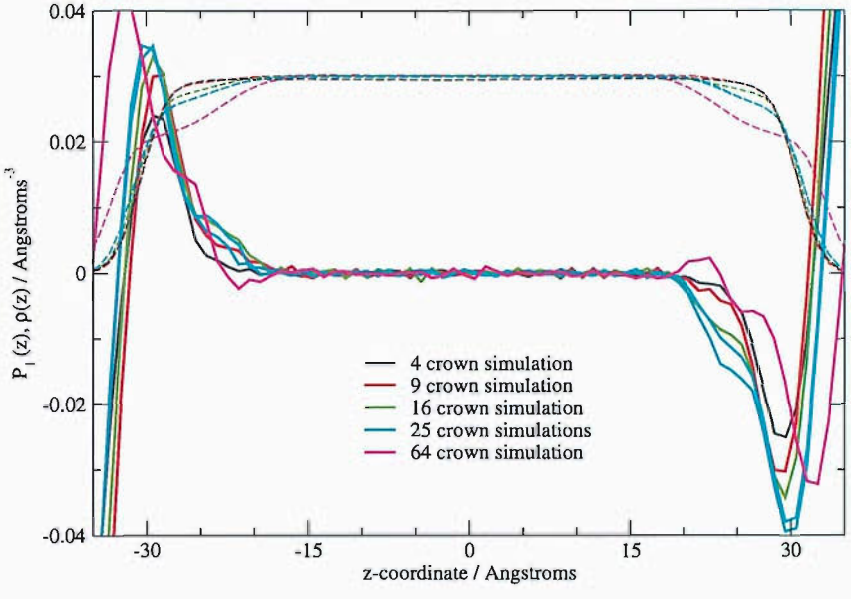

Figure 6.9: The orientational profile, showing $P_1(z)$ (solid, bold lines), of water for several 4-nitrobenzo-15-crown-5 concentrations. Also shown are the density profiles, $\rho(z)$,of the water slabs (dashed lines). The profiles of the water slab is shown for both starting configurations of the 25 crown simulation (I and II). There is an enhanced structure in the interfacial region due to the presence of the adsorbate, which becomes more pronounced with increasing concentration of nitrocrown.

In this system, the presence of a high surface concentration of nitrocrown has again thickened the ordered part of the interface. As well as the layer where the water dipole points towards the bulk water, which is seen in the pure water profile, there is an additional layer deeper in the slab where the molecules are also showing a tendency for their dipoles to be into the bulk water. There is an indication that there is some further slight ordering in the next layer of water too, as $\langle P_1 \rangle$ of the dipole goes very slightly positive (that is, the water dipoles are tending to point towards the bulk vapour region). Although this is a very small feature, the profile

is averaged over a large number of frames of simulation.

The results highlight that the water contribution to the SH signal may well be significantly changed in the presence of an adsorbate. For partially soluble surfactants it is likely that the change in orientational profile of the water is slightly over-emphasised in simulations such as these, since there are no bulk molecules to moderate the influence of the adsorbate upon the water surface. Nonetheless, there is very little doubt that there is some modification of the water surface by the presence of a surfactant, and great care must be taken when trying to separate contributions to surface measurements.

Summary

The assumptions involved in the analysis of SHG data have been addressed using the MD simulations. Firstly, the simulations and the experimental work agree to a large extent, with both studied systems having a wide distribution of tilt angle, the ψ assumptions giving the most likely results from the experimental work agreeing with the determined ψ angles from the simulations. This consistency in the observed data lends weight to the further investigation of the assumptions underlying the analysis of the SHG work.

The interfacial refractive index is a problematic parameter to obtain - it is very difficult to obtain a value experimentally. The method used in the MD estimate of the value did not entirely correlate to the experimentally estimated value for the benzo-15-crown-5 (this experimental estimate could not be carried out on the nitrocrown, as the data was not clearly in the weak limit). However, it cannot be concluded on the basis of this project which estimate gives the best estimate of n_{int}, since there are issues regarding the extent to which the system is weakly ordered (this affects the estimate from the SHG data), and also there is the issue that no bulk crowns are present in the simulations, which may influence the extent to which the chromophores are submerged. It may be that a simulation run with a number of crown ether molecules in the bulk, as well as at the surface would lead to a clearer idea of the true interfacial refractive index.

The Euler angles seem to be well represented in the simulations, and support the findings of the SHG experiments. The angle ϕ does tend towards a random distribution, as is assumed in the experimental analysis. However, the distribution of this angle in the simulations takes some time to equilibrate - this is a result of the highly orered starting configurations used. The length of the simulations presented here (10 ns) is sufficient to allow this equilibration to a random distribution, even at the highest surface concentrations, but shorter timescales may not be. The distribution of the angle ψ for both systems supports the experimentally determined most probable ψ preference, supporting the assumptions employed. For θ, again the distributions supported the experimental findings, as is seen by the D parameter which would arise given the type of distribution calculated, with particular agreement seen for the benzo-15-crown-5 system. For the 4-nitrobenzo-15-crown-5, the situation is slightly complicated given the phase between the electric fields of the crown and the water. An attempt to separate these contributions may be the reason for the discrepancy between the simulation and experiment at low concentrations. This separation was carried out assuming the water contribution to be unchanged by the presence of the crown ether, and when the water orientational profile was investigated in the simulations, it is clear that this is not the case: the presence of the nitrocrown significantly alters the surface layer of the water slab.

The assumption required for the use of the DRF analysis method is that the distributions of ψ and θ are independent of each other: the analysis requires separation of an average of products into a product of averages. The values of each of these have been calculated from the simulations, and found to be very close. Thus, within errors, this assumption is also met.

Chapter 7

Conclusions

This thesis contains a surface study of benzo-15-crown-5 and 4-nitrobenzo-15-crown-5 at the water-air interface using surface tension measurements, second harmonic generation experiments and molecular dynamics simulations.

The simulations and the experiments have been run alongside each other and the combined results have allowed a detailed characterisation of each interface. Both simulations and nonlinear optical spectroscopy are relatively new concepts, and this project has illustrated that a good consistency between the findings from both may be achieved.

The study of crown ethers is a huge field, due to the highly selective ion-binding property which crown ethers possess, and also due to their ability to form supramolecular structures. This study focuses on two simple but nonlinearly active aromatic crown ethers, in their free (uncomplexed) form, in order that they might be fully characterised with respect to their behaviour at the interface. Specifically, the assumptions underlying SHG analysis have been addressed. Once such systems have been characterised successfully, the prospects for using combined studies such as this one are promising.

The main limitation for the analysis of SHG is that the model for the calculation of orientational properties relies on many assumptions about the system which cannot necessarily be verified through experiment, such as the interfacial refractive

index, and the Euler angle ψ. The use of simulations to enhance the reliability of data obtained, in this case by justifying the choice of assumptions, becomes ever more practical as computers grow more powerful and efficient.

7.1 Systems Studied

Initially, the surface tension, SHG polarisation dependence and concentration dependence of the crown ethers were studied over a concentration range between 0 and 10 mM. The surface tension measurements provided an area per molecule which was used to set up several interfacial molecular dynamics simulations, representing various concentrations of crown ether. (Presently, it is not feasible to simulate bulk concentrations such as those used in these experiments.) The simulations were analysed in light of a comparison to SHG data obtained, the main aims being:

- To obtain a self consistent set of results based upon a combination of experimental and computational work,
- To assess and evaluate some of the assumptions which need to be made in order to analyse the Second Harmonic response of the systems.

The comparison of experiment to molecular dynamics has highlighted the limitations of current SHG analysis in a system where the molecular alignment is not perfectly unimodal. It is very interesting to see that once the order parameters are taken from the MD simulations, and used to calculate D and subsequently θ, the results are very similar to those obtained experimentally. It is an important observation that the system as simulated is not necessarily a low order system, although the distribution of θ is relatively wide. Benzo-15-crown-5 showed a clear trend in tilt angle with concentration.

For both species, a large degree of correlation was seen between neighbouring molecules - for the benzocrown, the preferred distance between chromophore centres was about 5.5 Å, whereas for the nitrocrown, a distance of about 3.9 Åwas

seen. The benzocrown chromophore centre was almost always above the level of the water, but the nitrocrown chromophore centre tended to be submerged, and with the nitro group oriented down into the water.

Both sets of simulations showed that the structure of the water interface was altered upon addition of crown ethers to the interface. This has significant implications for work in which, as for benzo-15-crown-5 and 4-nitrobenzo-15-crown-5, the non-linear optical signal from the adsorbed species is not very much higher than that from the pure water interface. This change in the water surface depends upon the concentration of crown ethers.

With computational techniques improving all the time, it is becoming possible to ascertain the values which should be assigned to the various Euler angles, hyperpolarisability components, interfacial refractive indices, and even the effect of the adsorbate on the substrate. This provides valuable information which may then be incorporated into experimental assumptions. As longer timescale MD simulations become more feasible with increasing computer power, so this type of combined study will become an important way of elucidating many characteristics of liquid interfacial systems.

7.2 Further Work

The crown ethers studied in this work have produced some very interesting results, both experimentally and through simulations. There are many more studies which could be carried out to characterise the surface behaviour fully, including investigating the system on addition of various ions, through both experimental and computational work:

1. A more in-depth study into how ion presence affects the surface behaviour of both of these crown ethers. The addition of sodium chloride was seen to strongly increase the intensity of the signal obtained from 4-nitrobenzo-15-crown-5.

2. Work should be done on some other simple crowns with different functional groups, and different ring sizes. This could provide a very interesting series of data from which other studies could proceed.

   And further computational work:

3. higher crown concentrations for the 4-nitrobenzo-15-crown-5 system: more crown molecules could be added to an equilibrated high concentration system, to see what to what extent the multi-layer will build up. It appears from these simulations that the benzo-15-crown-5 simulation where N_s=100 is already introducing equilibration issues. It would be interesting to run this simulation from the unfavourable starting configuration with the benzene rings closest to the interface, to see whether this forces any different behaviour within the system.

4. Long crown simulations for both species could be run with a starting configuration of bulk crown ethers. It might be that constraints would have to be introduced to pull the molecules to the surface, but it would be interesting to see how an equilibration period in the bulk water would affect the crown behaviours.

5. the addition of ions to a simulation imposes some issues on a system, but would worth looking into if the ion addition was studied experimentally, as a comparison.

Appendix A

The Transformation Matrix, T

The nonlinear susceptibility tensor, $\chi^{(2)}$, of a system, is related to the hyperpolarisability of the molecules at the surface, through Equation A.1.

$$\chi^{(2)} = \frac{N_s}{\varepsilon_o}\langle T\rangle\beta^{(2)} \tag{A.1}$$

Where $\chi^{(2)}$ is the second-order susceptibility tensor, N_s is the number density of the species at the interface, T is a transformation matrix, and $\beta^{(2)}$ is the molecular hyperpolarisability tensor.

This gives a system of equations relating the components of $\chi^{(2)}$ to those of $\beta^{(2)}$, as described in the following section.

The relationship between $\chi^{(2)}$ and $\beta^{(2)}$ is given in Section 2.2 by:

$$\chi_{ijk} = N_D\langle T_{ii'}T_{jj'}T_{kk'}\rangle\beta_{i'j'k'} \tag{A.2}$$

The rotation matrices for transformation from the laboratory to the molecular frame ($R_\psi R_\theta R_\phi$) are:

$$R_\psi = \begin{bmatrix} cos\psi & -sin\psi & 0 \\ sin\psi & cos\psi & 0 \\ 0 & 0 & 1 \end{bmatrix} \tag{A.3}$$

$$R_\theta = \begin{bmatrix} 1 & 0 & 0 \\ 0 & cos\theta & -sin\theta \\ 0 & sin\theta & cos\theta \end{bmatrix} \tag{A.4}$$

$$R_\phi = \begin{bmatrix} cos\phi & -sin\phi & 0 \\ sin\phi & cos\phi & 0 \\ 0 & 0 & 1 \end{bmatrix} \tag{A.5}$$

Through the SHG experiments, we derive information on the laboratory frame, and so we need to carry out the transformation from molecular onto laboratory frame. For this, the inverse of the transformations above are needed. The entire transformation is $T = R_\phi^{-1} R_\theta^{-1} R_\psi^{-1}$. The matrices involved are given in Equations A.6 to A.8.

$$R_\phi^{-1} = \begin{bmatrix} cos\phi & sin\phi & 0 \\ -sin\phi & cos\phi & 0 \\ 0 & 0 & 1 \end{bmatrix} \tag{A.6}$$

$$R_\theta^{-1} = \begin{bmatrix} 1 & 0 & 0 \\ 0 & cos\theta & sin\theta \\ 0 & -sin\theta & cos\theta \end{bmatrix} \tag{A.7}$$

$$R_\psi^{-1} = \begin{bmatrix} cos\psi & sin\psi & 0 \\ -sin\psi & cos\psi & 0 \\ 0 & 0 & 1 \end{bmatrix} \tag{A.8}$$

Which gives the full transformation matrix, T, shown in Equation A.9.

$$T = \begin{bmatrix} cos\psi cos\phi - sin\phi sin\psi cos\theta & sin\psi cos\phi + sin\phi cos\psi cos\theta & sin\phi sin\theta \\ -cos\psi sin\phi - sin\psi cos\phi cos\theta & cos\psi cos\phi cos\theta - sin\psi sin\phi & cos\phi sin\theta \\ sin\theta sin\psi & -sin\theta cos\psi & cos\theta \end{bmatrix} \tag{A.9}$$

Appendix B

Derivation of the D, R, F based expressions for $\chi^{(2)}$

The general expressions for the components of the surface susceptibility, for an isotropic liquid interface (where the azimuthal angle, ϕ, is random), are:[5]

$$\chi_{xzx} = \frac{N}{2\varepsilon_o}\left[\langle sin^2\theta\cos\theta\rangle\beta_{zzz} - \langle sin^2\psi\cos\theta sin^2\theta\rangle\left(\beta_{zxx} + 2\beta_{xzx}\right) + \langle\cos\theta\rangle\beta_{xxz}\right] \tag{B.1}$$

$$\chi_{zxx} = \frac{N}{2\varepsilon_o}\left[\langle sin^2\theta\cos\theta\rangle\beta_{zzz} - \langle sin^2\psi\cos\theta sin^2\theta\rangle\left(\beta_{zxx} + 2\beta_{xzx}\right) + \langle\cos\theta\rangle\beta_{zxx}\right] \tag{B.2}$$

$$\chi_{zzz} = \frac{N}{\varepsilon_o}\left[\langle\cos^3\theta\rangle\beta_{zzz} - \langle sin^2\psi\cos\theta sin^2\theta\rangle\left(\beta_{zxx} + 2\beta_{xzx}\right)\right] \tag{B.3}$$

These expressions are then simplified by taking assumptions on the distribution of ψ. For the case where ψ is random, such that $sin^2\psi = 0.5$, Equations B.1 to B.3 become:

$$\chi_{xzx} = \frac{N}{2\varepsilon_o}\left[\langle sin^2\theta\cos\theta\rangle\beta_{zzz} - \frac{1}{2}\langle\cos\theta sin^2\theta\rangle\left(\beta_{zxx} + 2\beta_{xzx}\right) + \langle\cos\theta\rangle\beta_{xxz}\right] \tag{B.4}$$

$$\chi_{zxx} = \frac{N}{2\varepsilon_o}\left[\langle sin^2\theta\cos\theta\rangle\beta_{zzz} - \frac{1}{2}\langle\cos\theta sin^2\theta\rangle\left(\beta_{zxx}+2\beta_{xzx}\right) + \langle\cos\theta\rangle\beta_{zxx}\right] \quad \text{(B.5)}$$

$$\chi_{zzz} = \frac{N}{\varepsilon_o}\left[\langle\cos^3\theta\rangle\beta_{zzz} - \frac{1}{2}\langle\cos\theta sin^2\theta\rangle\left(\beta_{zxx}+2\beta_{xzx}\right)\right] \quad \text{(B.6)}$$

For the case where the significant components of $\beta^{(2)}$ are β_{zzz} and β_{zxx}, Equations B.4 to B.6 may be expressed in terms of D, R and F, where:

$$D = \frac{\langle\cos^3\theta\rangle}{\cos\theta} \quad \text{(B.7)}$$

$$R = \frac{\beta_{zxx}}{\beta_{zzz}} \quad \text{(B.8)}$$

$$F = \frac{N_s}{2\varepsilon_o}\langle\cos\theta\rangle\beta_{zzz} \quad \text{(B.9)}$$

Equations B.4 to B.6 may be written:

$$\chi_{xzx} = F\left[(1-D) - \frac{R}{2}(1-D)\right] \quad \text{(B.10)}$$

$$\chi_{zxx} = F\left[(1-D) - \frac{R}{2}(1-D) + R\right] \quad \text{(B.11)}$$

$$\chi_{zzz} = F\left[2D + (1-D)R\right] \quad \text{(B.12)}$$

Similarly, for the same system, if ψ is 0, then $sin^2\psi = 0$, and the DRF expressions are:

$$\chi_{xzx} = F(1-D) \quad \text{(B.13)}$$

$$\chi_{zxx} = F(1-D+R) \quad \text{(B.14)}$$

$$\chi_{zzz} = 2FD \tag{B.15}$$

And for $\psi = 90^{\circ}$, the system of equations is:

$$\chi_{xzx} = F(1-D)(1-R) \tag{B.16}$$

$$\chi_{zxx} = F[(1-D)(1-R)+R] \tag{B.17}$$

$$\chi_{zzz} = F(2D-R(1-D)) \tag{B.18}$$

Appendix C

Calculating the Orientation Parameter, D

The order parameter, D, may be expressed in terms of the derived χ components. The expression depends upon which components of β are significant, and on the assumption taken on ψ. Several cases are given in Tables C.1 and C.2.

Significant β_{klm}	Assumption on ψ	D
β_{zzz}	random or 90°	$\frac{\chi_{zzz}}{\chi_{zzz}+2\chi_{zxx}}$
β_{zxx}	random	$\frac{2\chi_{zxx}-\chi_{zzz}}{2\chi_{zxx}+2\chi_{zzz}}$
	90°	$\frac{2\chi_{zxx}}{2\chi_{zxx}+\chi_{zzz}}$
β_{xzx}	random	$\frac{\chi_{xzx}}{\chi_{xzx}-\chi_{zxx}}$
	90°	$\frac{2\chi_{xzx}-\chi_{zxx}}{2\chi_{xzx}-2\chi_{zxx}}$

Table C.1: Order parameter, D, expressed in terms of χ for single significant hyperpolarisability tensor component.

Significant β_{klm}	Assumption on ψ	D
β_{zzz} and β_{zxx}	random	$\frac{\chi_{zzz}-\chi_{zxx}+\chi_{xzx}}{\chi_{zzz}-\chi_{zxx}+3\chi_{xzx}}$
	90^{o}	$\frac{\chi_{zzz}-2\chi_{zxx}+2\chi_{xzx}}{\chi_{zzz}-2\chi_{zxx}+4\chi_{xzx}}$
β_{zzz} and β_{xzx}	random	$\frac{\chi_{zzz}+2\chi_{zxx}-2\chi_{xzx}}{\chi_{zzz}+4\chi_{zxx}-2\chi_{xzx}}$
	90^{o}	$\frac{\chi_{zzz}+4\chi_{zxx}-4\chi_{xzx}}{\chi_{zzz}+6\chi_{zxx}-4\chi_{xzx}}$
β_{zxx} and β_{xzx}	random	$\frac{\chi_{zzz}+2\chi_{zxx}+4\chi_{xzx}}{3\chi_{zzz}+2\chi_{zxx}+4\chi_{xzx}}$
	90^{o}	$\frac{2\chi_{zzz}+2\chi_{zxx}+4\chi_{xzx}}{3\chi_{zzz}+2\chi_{zxx}+4\chi_{xzx}}$

Table C.2: Order parameter, D, expressed in terms of χ for two significant hyperpolarisability tensor components.

Appendix D

The Parameters Used in the SPC/E and TIP3P Water Models

The parameters used to create the SPC/E and TIP3P models used in this work are given, in order that all the parameters used for the molecular modelling work are reported.

	SPC/E	TIP3P
OH bond length / Å	1.0	0.9572
HOH bond angle / ^{o}	109.47	104.52
A$x10^{-3}$ / kcal $Å^{12}$ mol^{-1}	629.4	582.0
C/ kcal $Å^{6}$ mol^{-1}	625.5	595.0
charge, q, on O	-0.8472	-0.834
charge, q, on H	0.4238	0.417

Table D.1: The parameters used in the SPC/E and TIP3P water potentials.

Appendix E

Typical NAMD Input File for Simulations

A NAMD input file is included for production simulations on bulk water, and pressure profiling slab simulations.

For bulk water, a typical input file is:

#INPUT
extendedsystem in.xsc
velocities in.vel
wrapWater on

#FORCEFIELD
amber yes
parmfile in.top
coordinates in.coor
readexclusions yes
scnb 2.0
1-4scaling 0.833333
exclude scaled1-4

#SHAKE
rigidTolerance 0.00000001

```
rigidbonds all

    #APPROXIMATIONS
switching on
switchdist 9
cutoff 11
pairlistdist 13

    #PME PARAMETERS
PME yes
PMEinterporder 6
PMEGridsizex 80
PMEGridsizey 80
PMEGridsizez 60
margin 0
stepspercycle 1
timestep 2.0
dcdfreq 5000

    #OUTPUT
outputname nptL.out
outputenergies 10
outputtiming 1000
binaryoutput no
restartfreq 1000
XSTfreq 10

    #THERMOSTAT
langevin on
langevinTemp 298
langevinDamping 1

    #BAROSTAT
useGroupPressure yes
useFlexibleCell no
```

```
LangevinPiston on
LangevinPistonTarget 1.013377
LangevinPistonPeriod 400
LangevinPistonDecay 300
LangevinPistonTemp 298
run 50000
```

An input file for simulation of a slab of water (with or without crown ethers present), including pressure profiling parameters, would be:

```
    #INPUT
coordinates in.coor
velocities in.vel
extendedsystem in.xsc
parmfile in.top

    #FORCEFIELD
amber yes
scnb 2.0
exclude scaled1-4
1-4scaling 0.8333333

    #SHAKE rigidBonds all
rigidTolerance 0.00000001

    #APPROXIMATIONS switching on
switchdist 9
cutoff 11
pairlistdist 13

    #PME PARAMETERS
PME yes
PMEinterporder 6
PMEGridsizex 80
PMEGridsizey 80
```

```
PMEGridsizez 300
margin 0
stepspercycle 1
timestep 2.0

    #PRESSURE PROFILING
pressureProfile on
pressureProfileSlabs 300
pressureProfileFreq 5
dcdfreq 5

    #OUTPUT
outputname out
outputenergies 1
outputtiming 1000
binaryoutput no
wrapAll on
restartfreq 1000
XSTfreq 50

    #BAROSTAT
langevin on
langevinTemp 298
langevinDamping 1
useGroupPressure yes
run 10000
```

And the long range part of the pressure profile is calculated offline using a script such as:

```
    #INPUT FILES
coordinates in.coor
velocities in.vel
extendedsystem in.xsc
```

```
parmfile in.top

    #FORCEFIELD
amber yes
scnb 2.0
exclude scaled1-4
1-4scaling 0.8333333

    #SHAKE
rigidBonds all
rigidTolerance 0.00000001

    #APPROXIMATIONS switching off
cutoff 20
pairlistdist 20.5
margin 0
stepspercycle 1

    #PRESSURE PROFILING pressureProfile on
pressureProfileSlabs 300
pressureProfileFreq 5
pressureProfileNonbonded on

    #OUTPUT
outputname outnb
outputenergies 1
outputtiming 1000
binaryoutput no
wrapAll on
restartfreq 1000
XSTfreq 50

    #LANGEVIN THERMOSTAT
langevin on
langevinTemp 298
```

```
langevinDamping 1

    #NOSE-HOOVER LANGEVIN PISTON BAROSTAT
useGroupPressure yes

    #TCL SCRIPT
set ts 5
coorfile open dcd out.dcd
while { [coorfile read] !=-1} {
firstTimestep $ts
run 0
incr ts 5
}
coorfile close
```

Appendix F

The Long Range Correction for Surface Tension

The surface tension calculated from simulations is significantly affected by the truncation of long range forces. The correction for the van der Waals forces is given by 5.3, and the upper bound of this correction is given in 5.4. This upper bound is derived here.

$$\gamma_{LRC} = 12\pi\varepsilon\sigma^6 (\rho_L - \rho_v)^2 \int_0^{+1} ds \int_{r_c}^{\infty} dr \, coth\left(\frac{rs}{d}\right) \left(3s^3 - s\right) r^{-3} \tag{F.1}$$

For very sharp interfaces, i.e where the thickness of the interface is essentially zero, $\frac{rs}{d}$ tends to infinity, and thus, $coth\left(\frac{rs}{d}\right)$ tends towards 1. Equation F.1 therefore becomes:

$$\gamma_{LRC} = 12\pi\varepsilon\sigma^6 (\rho_L - \rho_v)^2 \int_0^{+1} ds \int_{r_c}^{\infty} dr \left(3s^3 - s\right) r^{-3} \tag{F.2}$$

Decomposing this gives:

$$\int_{r_c}^{\infty} \left(3s^3 - s\right) r^{-3} dr = \left[-\frac{\left(3s^3 - s\right)}{2r^2} \right]_{r=r_c}^{r=\infty} = \frac{\left(3s^3 - s\right)}{2r_c^2} \tag{F.3}$$

So that F.1 then becomes:

$$\gamma_{LRC} = 12\pi\varepsilon\sigma^6 (\rho_L - \rho_v)^2 \int_0^{+1} \frac{(3s^3 - s)}{2r_c^2} ds \tag{F.4}$$

Where:

$$\int_0^1 \frac{(3s^3 - s)}{2r_c^2} ds = \frac{1}{2r_c^2} \left[-\frac{3s^4}{4} - \frac{s^2}{2} \right]_{s=0}^{s=1} = \frac{1}{8r_c^2} \tag{F.5}$$

Thus, Equation F.1 becomes Equation F.6.

$$\gamma_{LRC} = \frac{12\pi\varepsilon\sigma^6}{8r_c^2} (\rho_L - \rho_v)^2 \tag{F.6}$$

Which may be expanded and written using reduced Lennard-Jones units, as in Equation F.7.

$$\gamma_{LRC} = \frac{3\pi\varepsilon}{2r_c^2} \left(\rho *_L^2 - 2\rho *_L \rho *_V - \rho *_V^2 \right) \tag{F.7}$$

Bibliography

[1] R. Aveyard and D. A. Haydon, *The Principles of Surface Chemistry*, Cambridge University Press, (1973).

[2] J. M. Gold, D. M. Teegarden, K. M. Mcgrane, D. J. Luca, P. A. Falcigno, C. C. Chen and T. W. Smith, *J. Am. Chem. Soc.*, **108**, 5827, (1986).

[3] P. A. Heiney, M. R. Stetzer, O. Y. Mindyuk, E. Dimasi, A. R. Mcghie, H. Liu and A. B. Smith, *J. Phys. Chem. B*, **103**, 6206, (1999).

[4] F. MacRitchie, *Chemistry at Interfaces*, Academic Press, Inc., San Diego/London, (1990).

[5] P.-F. Brevet, *Cahiers de Chimie: Surface Second Harmonic Generation*, Presses Polytechniques et Universitaires romandes, Lausanne, (1997).

[6] Y. R. Shen, *Surface Science*, **300**, 551, (1994).

[7] A. J. Timson, R. D. Spencer-Smith, A. K. Alexander, R. Greef and J. G. Frey, *Measurement Science and Technology*, **14**, 508, (2003).

[8] S. Kohli, C. D. Rithner, P. K. Dorhout, A. M. Dummer and C. S. Menoni, *Review of Scientific Instruments*, **76**, 107, (2005).

[9] J. W. Benjamins, K. Thuresson and T. Nylander, *Langmuir*, **21**, 149, (2005).

[10] J. Minones, C. Carrera, P. Dynarowicz-Latka, J. Minones, O. Conde, R. Seoane and J. M. R. Patino, *Langmuir*, **17**, 1477, (2001).

[11] F. Ahmad, F. Constabel, K. E. Geckeler, O. H. Seeck, Y. S. Seo, S. K. Satija, S. Kubik and K. Shin, *Isr. J. Chem.*, **45**, 345, (2005).

[12] B. B. Luokkala, S. Garoff and R. M. Suter, *Physical Review E*, **62**, 2405, (2000).

[13] C. A. Miller and P. Neogi, *Interfacial Phenomena: Equilibrium and Dynamic Effects*, Marcel Dekker, Inc., New York and Basel, (1985).

[14] J. W. Gibbs, *Trans. Conn. Acad. (Reprinted in The Scientific Papers of J. Willard Gibbs, Vol 1, New York, Dover*, **3**, 343, (1878).

[15] C. H. Chang and E. I. Franses, *Colloids and Surfaces a-Physicochemical and Engineering Aspects*, **100**, 1, (1995).

[16] S. Y. Lin, K. Mckeigue and C. Maldarelli, *Langmuir*, **7**, 1055, (1991).

[17] L. Marrucci, D. Paparo, G. Cerrone, C. De Lisio, E. Santamato, S. Solimeno, S. Ardizzone and P. Quagliotto, *Optics and Lasers in Engineering*, **37**, 601, (2002).

[18] J. F. Mcgilp, *Journal of Physics D-Applied Physics*, **29**, 1812, (1996).

[19] H. Motschmann, R. Teppner, S. Bae, K. Haage and D. Wantke, *Colloid and Polymer Science*, **278**, 425, (2000).

[20] M. Born and E. Wolf, *Principles of Optics*, Pergamon Press, New York, (1959).

[21] V. Mizrahi and J. E. Sipe, *Journal of the Optical Society of America B-Optical Physics*, **5**, 660, (1988).

[22] N. Bloembergen and P. S. Pershan, *Phys. Rev.*, **128**, 606, (1962).

[23] J. A. Ekhoff and K. L. Rowlen, *Analytical Chemistry*, **74**, 5954, (2002).

[24] J. G. Frey, *Chem. Phys. Lett.*, **323**, 454, (2000).

[25] Y. R. Shen, *Applied Physics B-Lasers and Optics*, **68**, 295, (1999).

[26] S. Vanelshocht, T. Verbiest, M. Kauranen, A. Persoons, B. M. W. Langeveldvoss and E. W. Meijer, *J. Chem. Phys.*, **107**, 8201, (1997).

[27] M. J. E. Morgenthaler and S. R. Meech, Applications of surface second order nonlinear optical signals, (From An Introduction to Laser Spectroscopy, Eds D. L. Andrews and A. A. Demidov, 1995).

[28] S. Haslam, S. G. Croucher, C. G. Hickman and J. G. Frey, *Physical Chemistry Chemical Physics*, **2**, 3235, (2000).

[29] D. A. Higgins, M. B. Abrams, S. K. Byerly and R. M. Corn, *Langmuir*, **8**, 1994, (1992).

[30] G. J. Simpson and K. L. Rowlen, *J. Am. Chem. Soc.*, **121**, 2635, (1999).

[31] D. A. Steinhurst and J. C. Owrutsky, *J. Phys. Chem. B*, **105**, 3062, (2001).

[32] A. Castro, K. Bhattacharyya and K. B. Eisenthal, *J. Chem. Phys.*, **95**, 1310, (1991).

[33] G. J. Simpson and K. L. Rowlen, *Analytical Chemistry*, **72**, 3399, (2000).

[34] G. J. Simpson and K. L. Rowlen, *Analytical Chemistry*, **72**, 3407, (2000).

[35] L. Danos, Phd thesis (non-linear spectroscopic studies at interfaces: Experiment and theory), (2003).

[36] A. A. T. Luca, P. Hebert, P. F. Brevet and H. H. Girault, *J. Chem. Soc., Fararay Trans.*, **91**, 1763, (1995).

[37] A. J. Fordyce, W. J. Bullock, A. J. Timson, S. Haslam, R. D. Spencer-Smith, A. Alexander and J. G. Frey, *Mol. Phys.*, **99**, 677, (2001).

[38] V. P. Sokhan and D. J. Tildesley, *Mol. Phys.*, **92**, 625, (1997).

[39] M. C. Goh, J. M. Hicks, K. Kemnitz, G. R. Pinto, K. Bhattacharyya, T. F. Heinz and K. B. Eisenthal, *J. Phys. Chem.*, **92**, 5074, (1988).

[40] C. J. Pedersen, *J. Amer. Chem. Soc.*, **89**, 2495, (1967).

[41] B. A. Moyer, S. D. Alexandratos, R. Chiarizia, M. L. Dietz, B. P. Hay and R. A. Sachleben, Design and synthesis of the next generation of crown ethers for waste separations: An inter-laboratory comprehensive proposal, (1996-2000).

[42] M. Hiraoka, *Crown Compounds: Their Characteristics and Applications*, Elsevier Scientific Publishing Company, Amsterdam, Oxford, New York, (1982).

[43] G. F. Vandegrift and W. H. Delphin, *Journal of Inorganic and Nuclear Chemistry*, **42**, 1359, (1980).

[44] Z. S. Nickolov, K. Ohno and H. Matsuura, *J. Phys. Chem. A*, **103**, 7544, (1999).

[45] A. C. W. M. S. E. Dye, J. L., *J. Phys. Chem.*, **79**, 3065, (1975).

[46] S. W. Park, B. S. Choi, D. W. Park and S. S. Kim, *Journal of Industrial and Engineering Chemistry*, **11**, 527, (2005).

[47] M. L. Dietz and E. P. Horwitz, *Industrial and Engineering Chemistry Research*, **39**, 3181, (2000).

[48] E. P. Horwitz, M. L. Dietz and D. E. Fisher, *Solvent Extraction and Ion Exchange*, **9**, 1, (1991).

[49] R. Chiarizia, M. L. Dietz, E. P. Horwitz, W. C. Burnett and P. H. Cable, *Separation Science and Technology*, **34**, 931, (1999).

[50] R. Plehnert, J. A. Schroter and C. Tschierske, *Langmuir*, **14**, 5245, (1998).

[51] S. Y. Zaitsev, M. Belohradsky, J. Zavada and D. Mobius, *Thin Solid Films*, **248**, 78, (1994).

[52] M. Jozwiak, *Thermochimica Acta*, **417**, 27, (2004).

[53] M. Jozwiak, *Thermochimica Acta*, **417**, 31, (2004).

[54] M. Jozwiak, H. Piekarski and A. Jozwiak, *Journal of Molecular Liquids*, **106**, 15, (2003).

[55] Y. Takeda, T. Watanabe, H. Yamada and S. Katsuta, *Journal of Molecular Liquids*, **108**, 151, (2003).

[56] Takeda, Yaseyuki, Kamazawa and Toshishiro, *Bull. Chem. Soc. Jpn., EN*, **61**, 655, (1988).

[57] L. Danos, Personal communication.

[58] B. Dick, A. Gierulski, G. Marowsky and G. A. Reider, *Applied Physics B-Photophysics and Laser Chemistry*, **38**, 107, (1985).

[59] B. R. Brooks, R. E. Bruccoleri, B. D. Olafson, D. J. States, S. Swaminathan and M. Karplus, *J. Comput. Chem.*, **4**, 187, (1983).

[60] W. D. Cornell, P. Cieplak, C. I. Bayly, I. R. Gould, K. M. Merz, D. M. Ferguson, D. C. Spellmeyer, T. Fox, J. W. Caldwell and P. A. Kollman, *J. Am. Chem. Soc.*, **118**, 2309, (1996).

[61] Y. Duan, C. Wu, S. Chowdhury, M. C. Lee, G. M. Xiong, W. Zhang, R. Yang, P. Cieplak, R. Luo, T. Lee, J. Caldwell, J. M. Wang and P. Kollman, *J. Comput. Chem.*, **24**, 1999, (2003).

[62] W. L. Jorgensen and J. Tiradorives, *J. Am. Chem. Soc.*, **110**, 1657, (1988).

[63] T. Darden, D. York and L. Pedersen, *J. Chem. Phys.*, **98**, 10089, (1993).

[64] A. R. Leach, *Molecular Modelling: Principles and Applications*, Pearson Education Ltd., (1996, 2nd Ed. 2001).

[65] L. Verlet, *Phys. Rev.*, **159**, 98, (1967).

[66] W. C. Swope, H. C. Andersen, P. H. Berens and K. R. Wilson, *J. Chem. Phys.*, **76**, 637, (1982).

[67] J. Alejandre, D. J. Tildesley and G. A. Chapela, *J. Chem. Phys.*, **102**, 4574, (1995).

[68] A. Borodin and M. Kiselev, *Pure and Applied Chemistry*, **76**, 197, (2004).

[69] L. V. Woodcock, *Chem. Phys. Lett.*, **10**, 257, (1971).

[70] H. J. C. Berendsen, J. P. M. Postma, W. F. Vangunsteren, A. Dinola and J. R. Haak, *J. Chem. Phys.*, **81**, 3684, (1984).

[71] M. G. Paterlini and D. M. Ferguson, *Chem. Phys.*, **236**, 243, (1998).

[72] P. Mark and L. Nilsson, *J. Phys. Chem. B*, **105**, 24A, (2001).

[73] B. Guillot, *Journal of Molecular Liquids*, **101**, 219, (2002).

[74] A. Brodsky, *Chem. Phys. Lett.*, **261**, 563, (1996).

[75] H. J. C. Berendsen, J. P. M. Postma, W. F. van Gunsteren and J. Hermans, *Interaction Models for Water in Relation to Protien Hydration*, Dordrecht, Reidel.

[76] W. L. Jorgensen, J. Chandrasekhar, J. D. Madura, R. W. Impey and M. L. Klein, *J. Chem. Phys.*, **79**, 926, (1983).

[77] H. J. C. Berendsen, J. R. Grigera and T. P. Straatsma, *J. Phys. Chem.*, **91**, 6269, (1987).

[78] Stilling.Fh and A. Rahman, *J. Chem. Phys.*, **60**, 1545, (1974).

[79] M. W. Mahoney and W. L. Jorgensen, *J. Chem. Phys.*, **112**, 8910, (2000).

[80] C. Vega, E. Sanz and J. L. F. Abascal, *J. Chem. Phys.*, **122**, art. no., (2005).

[81] E. Sanz, C. Vega, J. L. F. Abascal and L. G. Macdowell, *Physical Review Letters*, **92**, art. no., (2004).

[82] G. Hura, J. M. Sorenson, R. M. Glaeser and T. Head-Gordon, *J. Chem. Phys.*, **113**, 9140, (2000).

[83] D. M. Ferguson, *J. Comput. Chem.*, **16**, 501, (1995).

[84] A. Morita and J. T. Hynes, *J. Phys. Chem. B*, **106**, 673, (2002).

[85] P. Ahlstrom, A. Wallqvist, S. Engstrom and B. Jonsson, *Mol. Phys.*, **68**, 563, (1989).

[86] P. Cieplak, P. Kollman and T. Lybrand, *J. Chem. Phys.*, **92**, 6755, (1990).

[87] M. Sprik, *J. Phys. Chem.*, **95**, 2283, (1991).

[88] S. W. Rick, S. J. Stuart and B. J. Berne, *J. Chem. Phys.*, **101**, 6141, (1994).

[89] L. Delle Site, R. M. Lynden-Bell and A. Alavi, *Journal of Molecular Liquids*, **98-9**, 79, (2002).

[90] M. Matsumoto and Y. Kataoka, *J. Chem. Phys.*, **88**, 3233, (1988).

[91] R. S. Taylor, L. X. Dang and B. C. Garrett, *J. Phys. Chem.*, **100**, 11720, (1996).

[92] S. E. Feller, R. W. Pastor, A. Rojnuckarin, S. Bogusz and B. R. Brooks, *J. Phys. Chem.*, **100**, 17011, (1996).

[93] L. Kale, R. Skeel, M. Bhandarkar, R. Brunner, A. Gursoy, N. Krawetz, J. Phillips, A. Shinozaki, K. Varadarajan and K. Schulten, *Journal of Computational Physics*, **151**, 283, (1999).

[94] R. M. Townsend and S. A. Rice, *J. Chem. Phys.*, **94**, 2207, (1991).

[95] E. Lindahl and O. Edholm, *J. Chem. Phys.*, **113**, 3882, (2000).

[96] M. P. Allen and D. J. Tildesley, *Computer Simulation of Liquids*, Oxford Science Publications, Clarendon Press, Oxford, (1987).

[97] G. A. Chapela, G. Saville, S. M. Thompson and J. S. Rowlinson, *Journal of the Chemical Society-Faraday Transactions Ii*, **73**, 1133, (1977).

[98] V. Simmons and J. B. Hubbard, *J. Chem. Phys.*, **120**, 2893, (2004).

[99] D. Duque and L. F. Vega, *J. Chem. Phys.*, **121**, 8611, (2004).

[100] J. C. Bryan, L. H. Delmau, B. P. Hay, J. B. Nicholas, L. M. Rogers, R. D. Rogers and B. A. Moyer, *Structural Chemistry*, **10**, 187, (1999).

[101] B. P. Hay, J. B. Nicholas and D. Feller, *J. Am. Chem. Soc.*, **122**, 10083, (2000).

[102] V. Lamare, D. Haubertin, J. Golebiowski and J. F. Dozol, *Journal of the Chemical Society-Perkin Transactions 2*, pp. 121–127, (2001).

[103] M. J. Wilson, R. A. Pethrick, D. Pugh and M. S. Islam, *J. Chem. Soc., Fararay Trans.*, **93**, 2097, (1997).

[104] J. B. Nicholas, B. P. Hay and D. A. Dixon, *J. Phys. Chem. A*, **103**, 1394, (1999).

[105] R. A. Sachleben, J. C. Bryan, N. L. Engle, T. J. Haverlock, B. P. Hay, A. Urvoas and B. A. Moyer, *European Journal of Organic Chemistry*, pp. 4862–4869, (2003).

[106] L. X. Dang and P. A. Kollman, *J. Phys. Chem.*, **99**, 55, (1995).

[107] P. Cieplak, D. A. Pearlman and P. A. Kollman, *J. Chem. Phys.*, **101**, 627, (1994).

[108] Y. X. Sun and P. A. Kollman, *J. Comput. Chem.*, **13**, 33, (1992).

[109] P. D. J. Grootenhuis and P. A. Kollman, *J. Am. Chem. Soc.*, **111**, 2152, (1989).

[110] L. Troxler and G. Wipff, *J. Am. Chem. Soc.*, **116**, 1468, (1994).

[111] A. Varnek, L. Troxler and G. Wipff, *Chemistry-a European Journal*, **3**, 552, (1997).

[112] J. Gumbart, Y. Wang, A. Aksimentiev, E. Tajkhorshid and K. Schulten, *Current Opinion in Structural Biology*, **15**, 423, (2005).

[113] I. Chandrasekhar, D. Bakowies, A. Glattli, P. Hunenberger, C. Pereira and W. F. Van Gunsteren, *Molecular Simulation*, **31**, 543, (2005).

[114] R. W. Benz, F. Castro-Roman, D. J. Tobias and S. H. White, *Biophysical Journal*, **88**, 805, (2005).

[115] M. S. Tomassone, A. Couzis, C. Maldarelli, J. R. Banavar and J. Koplik, *Langmuir*, **17**, 6037, (2001).

[116] V. P. Sokhan and D. J. Tildesley, *Faraday Discussions*, pp. 193–208, (1996).

[117] J. M. Hicks, K. Kemnitz and K. B. Eisenthal, *J. Phys. Chem.*, **90**, 560, (1986).

[118] P. B. Petersen, R. J. Saykally, M. Mucha and P. Jungwirth, *J. Phys. Chem. B*, **109**, 10915, (2005).

[119] P. B. Petersen and R. J. Saykally, *Chem. Phys. Lett.*, **397**, 51, (2004).

[120] D. Michael and I. Benjamin, *J. Phys. Chem. B*, **102**, 5145, (1998).

[121] H. F. Wang, E. Borguet and K. B. Eisenthal, *J. Phys. Chem. A*, **101**, 713, (1997).

[122] H. Kuhn and H. Rehage, *J. Phys. Chem. B*, **103**, 8493, (1999).

[123] H. Kuhn and H. Rehage, *Physical Chemistry Chemical Physics*, **2**, 1023, (2000).

[124] J. Chanda, S. Chakraborty and S. Bandyopadhyay, *J. Phys. Chem. B*, **109**, 471, (2005).

[125] M. Roeselova, J. Vieceli, L. X. Dang, B. C. Garrett and D. J. Tobias, *J. Am. Chem. Soc.*, **126**, 16308, (2004).

[126] S. Coles, M. B. Hursthouse, J. G. Frey and E. R. Rousay, http://ecrystals.chem.soton.ac.uk/145/, (2005).

[127] I. R. Hanson, *Acta Crystallographica Section B-Structural Science*, **34**, 1026, (1978).

[128] J. J. P. Stewart, *J. Comput.-Aided Mol. Design*, **4**, 1, (1990).

[129] M. J. Frisch, G. W. Trucks, H. B. Schlegel, P. M. W. Gill, B. G. Johnson, M. A. Robb, J. R. Cheeseman, G. A. Keith, T.and Petersson, J. A. Montgomery, K. Raghavachari, M. A. Al-Laham, V. G. Zakrzewski, J. V. Ortiz, J. B. Foresman, J. Cioslowski, B. B. Stefanov, A. Nanayakkara, M. Challacombe, C. Y. Peng, P. Y. Ayala, W. Chen, M. W. Wong, J. L. Andres, E. S. Replogle, R. Gomperts, R. L. Martin, D. J. Fox, J. S. Binkley, D. J. Defrees, J. Baker, J. P. Stewart, M. Head-Gordon, C. Gonzalez and J. A. Pople, *Gaussian 94, Revision C.3*, Gaussian, Inc., Pittsburgh PA, (1995).

[130] C. I. Bayly, P. Cieplak, W. D. Cornell and P. A. Kollman, *J. Phys. Chem.*, **97**, 10269, (1993).

[131] T. Cheatham, P. Cieplak and P. Kollman, *J. Biomol. Struct. Dyn.*, **16**, 845, (1999).

[132] I. Thormahlen, J. Straub and U. Grigull, *Journal of Physical Chemistry Reference Data*, **14**, 933, (1985).

[133] M. La Rosa, A. Uhlherr, C. H. Schiesser, K. Moody, R. Bohun and C. J. Drummond, *Langmuir*, **20**, 1375, (2004).

[134] R. D. Rogers, R. F. Henry and A. N. Rollins, *Journal of Inclusion Phenomena and Molecular Recognition in Chemistry*, **13**, 219, (1992).